Modeling of Capacity, Resistance, and Expansion of Lithium-ion Batteries as they Degrade: Linking Expansion and Degradation

by

Sravan Pannala

A dissertation submitted in partial fulfillment
of the requirements for the degree of
Doctor of Philosophy
(Mechanical Engineering)
in the University of Michigan
2025

Doctoral Committee:

Research Associate Professor Jason Siegel, Co-Chair
Professor Anna Stefanopoulou, Co-Chair
Professor Wei Lu
Assistant Professor Ziyou Song

Sravan Pannala
spannala@umich.edu
ORCID iD: 0000-0002-1847-6854

© Sravan Pannala 2025

DEDICATION

To my loving family for their unconditional love and unwavering support.

ACKNOWLEDGEMENTS

I would like to express my deepest gratitude to all those who have supported me throughout my dissertation journey.

First and foremost, I would like to thank my advisors, Prof. Jason Siegel and Prof. Anna Stefanopoulou, for their invaluable guidance, unwavering support, and insightful feedback. Your expertise and encouragement have been instrumental in shaping my research and pushing me to achieve my best.

I am also grateful to the members of my dissertation committee, Prof. Wei Lu and Prof. Ziyou Song, for their constructive critiques and insightful comments.

A heartfelt thank you goes to my present and former labmates in the Battery Control Group, especially Dr. Peyman Mohtat, Dr. Hamidreza Movahedi, Dr. Valentin Sulzer, Dr. Andrew Weng, Vivian Tran, Everardo Olide, Puneet Valecha, Dr. Miriam Figueroa, Dr. Suhak Lee, Dr. Ting Cai, Omar Ahmed, Zhiwen Wan, Clement Wong, for your camaraderie, support, and endless discussions that kept me motivated during the challenging times. I cherish the moments we shared in and out of the laboratory.

I would like to acknowledge the financial support provided by General Motors, Mercedes-Benz R&D North America, and the National Science Foundation under Grant No. 1762247, which made my research possible. Your investment in my education has made a significant impact. Thanks to colleagues at General Motors, Dr. Taylor Garrick, Matt Jones, and Rafid Mollah, for the exciting discussion and feedback.

To my family, especially my parents, thank you for your unconditional love and encouragement. Your belief in me has been a constant source of strength, and I am forever grateful for your support.

TABLE OF CONTENTS

DEDICATION ii

ACKNOWLEDGEMENTS iii

LIST OF FIGURES vii

LIST OF TABLES xiii

LIST OF APPENDICES xiv

ABSTRACT xv

CHAPTER

1 Introduction 1

1.1 Background and Motivation 1
1.2 Battery Degradation 3
1.2.1 Degradation Mechanisms 3
1.2.2 Tuning Degradation Models 5
1.3 Battery Expansion 6
1.3.1 Link between Degradation and Expansion 6
1.3.2 Sensing Expansion 9
1.3.3 Impact of Pressure 9
1.4 Dissertation Organization 10
1.5 Contributions 12

2 Development of Inductance Based Expansion Sensor 14

2.1 Introduction 14
2.2 Theory and Design of an Inductance-Based Expansion Sensor 16
2.2.1 Operating Principle 16
2.2.2 Coil Design 16
2.2.3 Target Design 18
2.3 Experimental Setup 18
2.3.1 Fixture 18
2.3.2 Testing Procedure 19
2.4 Results and Discussion 20
2.4.1 Calibrating Sensor 20

2.4.2 Uncertainty in Measurement . . . 21
2.4.3 Performance of Sensor during Battery Cycling . . . 22
2.4.4 Differential Expansion . . . 22
2.5 Conclusion . . . 23

3 Battery Electrochemical and Expansion Models . . . 25

3.1 Introduction . . . 25
3.2 Electrochemical Model: Single Particle Model . . . 26
3.3 Battery Expansion Model: Particle to Cell . . . 28
3.3.1 Particle Stress and Strain Model . . . 29
3.3.2 Particle Expansion . . . 31
3.3.3 Electrode Expansion due to Intercalation . . . 31
3.3.4 Total Expansion . . . 32
3.4 Conclusion . . . 33

4 Degradation Model Mechanisms . . . 34

4.1 Introduction . . . 34
4.2 SEI Growth . . . 35
4.3 Lithium Plating . . . 37
4.4 Mechanical Damage . . . 40
4.5 Effects of degradation mechanisms on battery performance . . . 45
4.5.1 Side Reaction Currents . . . 45
4.5.2 Resistance Growth . . . 46
4.5.3 Battery Expansion . . . 47
4.6 Interactions Between the Degradation Mechanisms . . . 49
4.7 Conclusions . . . 50

5 Tuning of Degradation Model Parameters . . . 51

5.1 Introduction . . . 51
5.2 Degradation Model Tuning Process . . . 51
5.2.1 Accelerated Simulations . . . 52
5.2.2 Degradation Mechanism States and Parameters . . . 54
5.2.3 Parameter fitting . . . 54
5.2.4 Sequential Tuning Process . . . 55
5.2.5 Parameterization of Degradation Mechanisms during Calendaring Aging . . . 56
5.2.6 Parameterization of Degradation Mechanisms during Cycling Aging 57
5.2.7 Parametrization of Resistance model . . . 58
5.2.8 Parameterization of Expansion model . . . 58
5.3 Experiments and Data . . . 58
5.3.1 Aging Methodology . . . 59
5.3.2 Performance Testing and eSOH calculation . . . 59
5.4 Results and Discussion . . . 60
5.4.1 Model Tuning Results . . . 60
5.4.2 Capacity Prediction . . . 60

5.4.3 Degradation Mechanism and Modes . . . 61
5.4.4 Resistance Prediction . . . 63
5.4.5 Irreversible Expansion Prediction . . . 67
5.4.6 Voltage and Total Expansion prediction for cycling at BOL, MOL, and EOL . . . 69
5.4.7 Contribution of Degradation Mechanisms . . . 70
5.5 Model Parameters . . . 71
5.6 Conclusions . . . 71

6 Modeling Degradation at Multiple Pressures . . . 74

6.1 Introduction . . . 74
6.2 Analyzing Degradation Data at Different Pressures . . . 74
6.2.1 Experimental Procedure . . . 76
6.2.2 Apparent Cell Capacity . . . 76
6.2.3 Negative Electrode Capacity . . . 76
6.2.4 Resistance . . . 77
6.2.5 Expansion . . . 78
6.3 Modeling Degradation at High Temperatures . . . 79
6.3.1 Tuning Degradation Model Parameters . . . 79
6.3.2 Results . . . 80
6.3.3 Contribution of Degradation Mechanisms to Capacity Loss, Resistance Growth and Irreversible Expansion . . . 83
6.3.4 Analysis . . . 86
6.4 Mechanical Damage Model: Impact of Pressure . . . 87
6.5 Results . . . 89
6.5.1 Capacity . . . 90
6.5.2 Resistance . . . 91
6.5.3 Expansion . . . 91
6.5.4 Contribution of Degradation Mechanisms . . . 92
6.6 Conclusion . . . 92

7 Conclusions and Future Work . . . 93

7.1 Summary of Contributions . . . 93
7.2 Future Work . . . 95
7.2.1 Extension to Different Cell Chemistries . . . 95
7.2.2 Model Improvements . . . 96
7.2.3 Model Validation . . . 97
7.2.4 Using Degradation Model for Charge Optimization . . . 97

APPENDICES . . . 98

BIBLIOGRAPHY . . . 130

LIST OF FIGURES

FIGURE

1.1 A Summary of inputs and outputs of the degradation model mechanisms. . . . 4
1.2 Voltage and battery expansion response over several cycles. The expansion within one charge-discharge cycle is reversible, while the expansion over many cycles is irreversible, as reported in [1]. The lower bound of the expansion plot shows the irreversible battery expansion, while the difference between the lower and upper bounds shows the reversible expansion. 7
1.3 Change in thickness due to SEI growth. Figure from [2] 8

2.1 The fixture used to measure expansion. The battery is placed between two aluminum plates. The plate above the battery moves in the direction shown by the red arrow when the battery expands and both the IDS (Inductive Displacement Sensor) and LDVT sensors capture this displacement. Reference coil is placed at a fixed distance from the top plate and the readings from this coil is used to compensate for environmental effects. 15
2.2 Principle of operation for an inductance-based battery expansion sensor. 17
2.3 IDS sensor reading in sensor counts vs LDVT distance in μm at 25°C and 45°C. We can observe that the relationship between IDS sensor reading and distance is linear with $r^2 > 0.999$ at both temperatures. The slope of the graph is 680 counts/μm at both temperatures. 20
2.4 Steady state IDS sensor measurement in μm for 1 hour. The sensor measurement has a noise with standard deviation of $0.26\,\mu m$ at 25°C, and $0.39\,\mu m$ at 45°C. These values could be considered as the practical resolution for the sensor. . . . 21
2.5 Comparing IDS expansion measurement with LDVT expansion measurement for a cell cycled at C/3 current for 5 cycles. Panel a) shows voltage response of the battery. Panel b) shows the expansion measurement plotted for both IDS and LVDT sensors. panel c) shows the error in measurement between IDS and LVDT sensors. Maximum error is 3.2 μm and the RMSE is 0.7 μm. 23
2.6 Differential expansion signal and battery SOH features locations P_1 and P_2 for both sensors for a C/3 charge. While location of P_1 is almost identical for both sensors, there was a 2% SOC error in the location of the P_2 feature. 24

3.1 Overview of the Single Particle Model (SPM). The input to the model is applied current and the output is terminal voltage. The SPM keeps track of states of lithiation in the negative and positive electrodes and uses these states to predict the voltage. 26

3.2 Illustration of the Battery reversible expansion model. Lithium intercalation leads to particle stress and strain. Particle strain results in electrode expansion. Battery expansion is the sum of the expansion of negative and positive electrodes. 28

4.1 Comparison of variables used in Li plating model at C/5 (blue), 1.5C (red). The variables compared are: c_{ss}^{-}, which influences the concentration gradient $c_{\mathrm{ss}}^{-} - c_{\mathrm{s,avg}}^{-}$ which in turn influences η_{pl}. We also compare $\exp\left(\frac{-\alpha_{c,pl}F}{RT}\eta_{pl}\right)$ which directly influences the plating current j_{pl} for two C-rates 37

4.2 Plating model comparison. a) shows the plating current and capacity loss for the conventional $i_{0,pl}$ formulation while b) shows the same for the new $i_{0,pl}$ formulation. The conventional $i_{0,pl}$ has higher capacity loss due to Li plating at C/5, the modified $i_{0,pl}$ shows higher capacity loss at 1.5C. This is because the modified $i_{0,pl}$ increases the gradient in magnitude of j_{pl} for the two C-rates while also adding the effect of Li stripping during discharge. 38

4.3 a) Volumetric strain of the negative electrode as a piecewise linear function of particle stoichiometry (concentration). b) Volumetric strain rate of the negative electrode. Strain rates for 100% DOD ($\Omega_{\mathrm{DOD,100}}$) and 50% DOD ($\Omega_{\mathrm{DOD,50}}$) estimated using Eq. 4.35. c) Values of σ_h at C/5 100% DOD estimated using concentration dependent stress Eq. 4.31 (black) and simplified stress Eq. 4.36 (blue). d) Values of σ_h at C/5 50% DOD estimated using concentration dependent stress Eq. 4.31 (black) and simplified stress Eq. 4.36 (green). The strain rate in the negative electrode is concentration dependent which results in different magnitudes of minimum and maximum stress at different DOD and thus different rate of capacity loss 41

4.4 Modeled current densities of intercalation, SEI, and plating at both BOL (blue) condition and EOL (red). We observe an increase in all three current densities during 1.5C cycling at EOL (33% Capacity Loss) compared to BOL. 45

4.5 (Simulated) Components of terminal voltage for 1C charging step on a cell at BOL and EOL after cycling at 1.5C-rate and 100% DOD. At EOL, we find higher electrode overpotentials (grey) and also higher voltage rise due to an increase in SEI resistance (orange) and Li plating resistance (blue). 46

4.6 The model for irreversible changes in battery thickness (irreversible expansion) is depicted in the Figure. Growth of SEI layer δ_{SEI}, formation of plated lithium δ_{pl} and LAM which results in the formation of inactive material $\varepsilon_{\mathrm{s,in}}$ contribute to irreversible expansion. 48

4.7 Summary of degradation model and SPM equations 49

5.1 A summary of degradation model tuning process. Here P represents the vector of tunable degradation mechanisms parameters, and X represents the model states that change as the battery ages. Voltage and expansion data can be processed at RPTs to extract eSOH parameters $\tilde{Y}$. The methodology to extract eSOH parameters is explained in Chapter A. An optimization algorithm is used to find P that minimizes the error between $\tilde{Y}$ and $\hat{Y}$ (extracted from model states). We adopt a sequential tuning process, i.e. tuning SEI degradation model P_{cal} first using data from calendar aging data where other degradation mechanisms aren't active and thus don't contribute to battery degradation. We then use the tuned parameters to tune the other degradation models P_{cyc} using cycling aging data. 52
5.2 Inter-cycle extrapolation, from [3]. The change in SOH parameters over one cycle, Δy_1, is assumed to be constant for the next n cycles, resulting in a $n\Delta y_1$ change over n cycles. The change in SOH over the n^{th} cycle is then calculated and extrapolated to the $2n^{\text{th}}$ cycle, etc. Here SOH represents an internal degradation variable of the model, of which there can be several, for example SEI thickness (k_{SEI}) or active material volume fraction in either electrode ($\varepsilon_{\text{s}}^{\pm}$). 53
5.3 The SEI growth model is tuned to match capacity loss and lithium loss for calendar aged cells stored at 100% SOC at 45°C (red) and -5°C (blue). Capacity, LLI, and eSOH parameters are shown here for data(markers), and simulations (lines). 61
5.4 The mechanical damage model and lithium plating model is tuned to match capacity loss, lithium loss and active material loss for cells cycled at C/5 (blue), 1.5C (red) and C/5 Charge 1.5C Discharge (orange) for 100% DOD. Capacity, LLI, and eSOH parameters are shown here for data(markers), and simulations (lines). 62
5.5 Capacity Prediction for a) 100% DOD cells b) 50% DOD vs 100% DOD cells. Cell nominal capacity is 5 Ah and the cells were cycled at $25°C$ 63
5.6 Degradation Modes Prediction for 100% DOD Cells. Cell nominal capacity is 5 Ah and the cells were cycled at $25°C$ 64
5.7 Resistance Growth Prediction for a) 100% DOD cells b) 50% DOD vs 100% DOD cells. Cell nominal capacity is 5 Ah and the cells were cycled at $25°C$. HPPC test data with 1C pulses averaged over various SOCs is used to calculate cell resistance. Data is shown as markers and the simulation is shown as lines. Dashed lines show the simulations on trained cells, and solid lines show predictions on untrained cells. The resistance is averaged over charge and discharge pulses and over SOC. 65
5.8 Resistance vs SOC at BOL, MOL, and EOL for C/5 100% DOD Cycling Aging Cell. HPPC test data with 1C pulses is used to calculate cell resistance. Resistance plotted is the average of charge and discharge resistance. Data is shown in black and simulation is shown in red. The model captures variation in resistance with SOC and also the resistance growth as the battery ages. 66
5.9 Irreversible Expansion Prediction for a) 100% DOD cells b) 50% DOD vs 100% DOD cells. Cell nominal capacity is 5 Ah and the cells were cycled at $25°C$ . . 68

5.10 Cycling Current, Voltage and Expansion profile at BOL, MOL and EOL for C/5, 1.5C and 2C cycling aging. Data is shown in black, and the simulation is shown in red. 69
5.11 Contribution of degradation mechanisms (SEI growth, Li plating, Negative electrode damage, Positive electrode damage) to capacity loss, resistance growth, and irreversible expansion for cell cycled at 1.5C 70

6.1 a) Battery fixture used to cycle cell and collect electrical and mechanical (expansion) data. Different springs were used to apply different pressures on the cell. b) Minimum and maximum battery expansion at each cycle under 0 kPa and 172 kPa, respectively. Minimum expansion occurs at the fully discharged state and is used as the value of irreversible expansion in this work. We also observe that the 0 kPa cell has a sharp increase in expansion due to gassing. 75
6.2 a) Apparent Capacity Loss, b) Resistance Growth and c) Irreversible Expansion for various pressures. 35 kPa cell has 25°C RPTs conducted at regular intervals, resulting in associated capacity recovery, high resistance growth, and irreversible during those tests. 75
6.3 Resistance is estimated for each cycle at the start of discharge where current changes suddenly 77
6.4 eSOH simulation and data for cells used for training degradation model parameters 81
6.5 Capacity, Resistance and Expansion Simulation vs Data for cells cycled under various currents at Hot Temp ($45°C$) 82
6.6 a) Modeled Negative electrode capacity, positive electrode capacity, lithium inventory (moles of cyclable lithium) and the battery capacity for a cell cycled at 2C and at $45°C$ b) Capacity loss and inventory loss 83
6.7 Components of voltage of an aged cell at 50% SOC during a pulse. These voltage components are used to calculate resistance growth due to each degradation mechanism 85
6.8 Contribution of degradation mechanisms (SEI growth, Li plating, Negative electrode damage, Positive electrode damage) to capacity loss, resistance growth and irreversible expansion at 35 kPa 87
6.9 Negative Electrode Mechanical Damage Coefficient (Scaled) $\beta^{-}_{\mathrm{LAM},s}$ vs Pressure 87
6.10 Capacity Simulation (Apparent Capacity Loss) for various pressures plotted against data 89
6.11 Resistance Simulation (Resistance growth) for various pressures plotted against data 90
6.12 Expansion Simulation (Irreversible expansion) for various pressures plotted against data 90
6.13 Impact of Pressure on contribution of degradation mechanisms to capacity loss, resistance growth and irreversible expansion 92

A.1 Voltage fitting during a C/5 charge (yellow) and a 1.5C charge (black) to estimate C_{n} of a 16% aged cell. The data is shown in black, and the model fit is shown in red. The orange regions, which represent the first and last 10% during the charge, are not used in voltage fitting to improve the fitting accuracy. 100

A.2 C_{n} calculation error in % for various sampling rates. The error is less than 0.2% if we have more than 3 samples per % SOC. 101
A.3 Empirical Negative electrode Capacity degradation model. The dots represent the data used for fitting, the solid lines represent the model fit at low C-rates, and the dotted lines represent the model fit at high C-rates. 105
A.4 C_{n} observer at C/5 100% DOD. The capacity in the plot is shown in the percentage of initial electrode capacity. The observed values $\hat{C}_{\mathrm{n}}$ [Eq. A.10] are shown as a black dashed line, the empirical degradation model C_{n} [Eq. A.19] (with model mismatch) as a green line, and voltage estimation values from voltage fitting $\overline{C_{\mathrm{n}}}$ [Eq. A.8] as cyan (during cycling) and as red (during RPT). The value of L for each cycle is also plotted. Since every cycle in this case has a low C-rate and high DOD, the value of $L = 0.5$ during all cycles. 106
A.5 C_{n} observer at 1.5C 100% DOD. The capacity in the plot is shown in the percentage of initial electrode capacity. The observed values $\hat{C}_{\mathrm{n}}$ [Eq. A.10] are shown as a black dashed line, the empirical degradation model C_{n} [Eq. A.19] as a green line, and voltage estimation values from voltage fitting $\overline{C_{\mathrm{n}}}$ [Eq. A.8] as cyan (during cycling) and as red (during RPT). The value of L for each cycle is also plotted. Since only the RPTs have low C-rate and high DOD, the value of $L = 0.5$ during only the RPTs. The rest of the cycles has $L = 0$. 107
A.6 C_{n} observer at C/5 50% DOD. The capacity in the plot is shown in the percentage of initial electrode capacity. The observed values $\hat{C}_{\mathrm{n}}$ [Eq. A.10] are shown as a black dashed line, the empirical degradation model C_{n} [Eq. A.19] as a green line, and voltage estimation values from voltage fitting $\overline{C_{\mathrm{n}}}$ [Eq. A.8] as cyan (during cycling) and as red (during RPT). The value of L for each cycle is also plotted. Since only the RPTs have low C-rate and high DOD, the value of $L = 0.5$ during only the RPTs. Here, we do not consider the data after 150 cycles for update which results in error between model and observer after 150 cycles. 108
A.7 Graphite Volumetric Strain and its 2nd derivative. The two peaks of 2nd derivative are located at stoichiometries 0.24 and 0.5 109
A.8 Voltage vs Expansion Derivative Signals at high C-rate (2C) (blue) and low C-rate (red). The second peak (around 2.7 Ah) is present in the expansion signal but disappears in the voltage signal for high C-rate but is present at low C-rate. 110
A.9 Comparing Cn estimated using expansion method vs voltage method 111
A.10 Negative Electrode Capacity at various pressures 112

B.1 Observer Schematic Diagram. The positive electrode observer depends on the inverted surface concentration $\check{c}_{ss}^{+}$ from the voltage inversion block which uses measured battery terminal voltage V_t. The voltage inversion depends on the open loop Electrolyte concentration estimate $\hat{c}_e$. The estimated positive electrode concentration $\hat{c}_s^{+}$ is then used in the expansion inversion block in combination with the measured battery temperature T_b and expansion δ_b to inform the negative electrode observer $\hat{c}_s^{-}$ using inverted negative electrode average concentration $\check{c}_{s,avg}^{-}$. 118

B.2 Simulation results for 1C Constant Current input with $SOC_0 = 0.05$ and $\hat{SOC}_0 = 0.10$ shown for two gains $\kappa^- = 0.001$ and $\kappa^- = 0.01$. (a) Current (b) Voltage (c) Expansion (d) Voltage and Expansion Errors (e) Surface Concentration of both electrodes c^-_{ss}, c^+_{ss} (f) Average Concentration of both electrodes $c^-_{s,avg}, c^+_{s,avg}$. Voltage and expansion converge to the measured values within 5 minutes. . . . 122
B.3 Simulation results for Stoichiometric Window Drift for Voltage and Expansion observer and Voltage only observer during Constant Current charge at 1C rate with $SOC_0 = 0.05$ and $\hat{SOC}_0 = 0.10$. (a) Surface Concentration error of both electrodes $c^-_{s,s}, c^+_{s,s}$ (b) Average Concentration error of both electrodes $c^-_{s,avg}, c^+_{s,avg}$. $\hat{c}^+_s$ converges for both observers, but $\hat{c}^-_s$ converges only for V+EXP-obs. 123
B.4 Simulation results for Active Material Ratio Drift for V+EXP-obs and V-obs with $SOC_0 = 0.05$ and $\hat{SOC}_0 = 0.10$. (a) Surface Concentration error of both electrodes $c^-_{s,s}, c^+_{s,s}$ (b) Average Concentration error of both electrodes $c^-_{s,avg}, c^+_{s,avg}$. The estimates of negative electrode concentration states $\hat{c}^-_s$ does not converge for either observer. 124

C.1 Negative Electrode Capacity Loss at various pressures plotted 127
C.2 Negative Electrode Mechanical Damage Coefficient (Scaled) $\beta^-_{\text{LAM},s}$ vs Pressure 128
C.3 a) Negative electrode capacity loss simulation at 35 and 138 kPa b) Apparent capacity loss simulation using outlier value of $\beta^-_{\text{LAM},s}(P)$ at 138 kPa 128
C.4 a) Negative electrode capacity loss simulation at 35 and 138 kPa b) Apparent capacity loss simulation without using outlier value of $\beta^-_{\text{LAM},s}(P)$ at 138 kPa . . 129

LIST OF TABLES

TABLE

2.1 Coil design parameters. 18

5.1 Time for Experiments and Simulations 58
5.2 List of Model Parameters and their values 71
5.3 Degradation Model Parameters 72
5.4 Tuned Degradation Model Parameters 72

6.1 Tuned Degradation Model Parameters shown at room temperature, hot temperature 82
6.2 Comparison of RMSE in Capacity, Resistance Growth and Expansion. Expansion in μm is converted to strain by dividing with the cell thickness of 4000μm. Thus an error of 0.5% corresponds to 20μm 83
6.3 Comparison of RMSE in Capacity, Resistance Growth, and Expansion for cells cycled at various pressures. 89

A.1 Cycle Aging Test Conditions 104

B.1 Simulation Error in RMSPE (after 5 minutes) of Concentration Estimates for V+EXP-obs and V-obs 125

LIST OF APPENDICES

A Electrode State of Health Estimation 98

Estimating eSOH from Degradation Model Variables 99
eSOH Based on Voltage Fitting of Electrode Open Circuit Potential 100
A Strategy for Updating Estimated Electrode Capacity using Data Screening Based on Pre-computed Error Bounds 101
Expansion Fitting to compute eSOH at high C-Rates 107
Conclusion 113

B Application of Expansion: Improving Estimation of Electrode Level Lithiation 114

Single Particle Model with Electrolyte 114
Thermal Model 115
Battery State Observer Design 116
Results 121
Conclusion 125

C Explaining the Outlier in Negative Electrode Capacity 127

ABSTRACT

Battery degradation leads to changes in battery dimensions. Reversible dimensional changes (expansion) due to lithium intercalation in the graphite take place during charging and reverse during discharging. The magnitude of the reversible expansion reduces as the batteries age and their capacity decreases over their lifetimes. Irreversible dimensional changes (irreversible expansion) are observed as an overall increase in battery thickness as the battery ages. Although there is a general understanding that these dimensional changes are functions of degradation mechanisms that affect the electrode thickness, such as solid-electrolyte interface (SEI), Li-plating, and stress-induced particle fracture, this thesis directly connects and parameterizes lifetime degradation mechanisms with expansion in multi-layer pouch cells.

The resulting physics-based model predicts the reversible and irreversible expansion under various laboratory cycling conditions for which the model has not been trained. The thesis contributions span novel and low-cost measuring techniques, advances in reduced-order modeling of lifetime degradation, and methodologies for parameterizing these models.

The predictive model has advanced state of electrode lithiation (SOL) estimation and electrode state-of-health (eSOH) estimation techniques that rely on interpreting the dimensional changes and attributing various patterns to plating or SEI that are indistinguishable from capacity loss or resistance growth.

Finally, the effects of externally applied pressure on capacity loss, resistance growth, and irreversible expansion are studied and modeled. The aging data shows us that the dominant degradation mechanism of negative electrode mechanical damage is pressure-dependent, and tuning it to match negative electrode loss of active material (LAM) at various pressures captures the influence of externally applied pressure on the lifetime capacity loss, resistance growth, and irreversible expansion. This work advances battery pack design, including the casing and padding design, the externally applied pressure on the cells, and the state of health estimation.

CHAPTER 1

Introduction

1.1 Background and Motivation

As we see a societal push towards the electrification of products that have traditionally been powered using fossil fuels, a great deal of work is required for engineers during the design phase to ensure that electrified products meet performance metrics at the beginning of product life, as well as the end-of-life. In automotive applications, these end-of-life criteria are usually captured in terms of a warranty requirement. For example, the California Air Resources Board (CARB) is driving towards a common battery warranty requirement for 2026 and later model years requiring that electric vehicles maintain at least 80 percent of their certified Urban Dynamometer Driving Schedule (UDDS) for 15 years or 150,000 miles. At the time of writing this thesis, the most common warranty is 8 years or 100,000 miles.

Lithium-ion batteries degrade when they undergo charging and discharging and also when they are stored (calendar aging). The rate of this degradation depends on how the batteries are used and under what conditions. Even if the Lithium-ion chemistry degrades less than other chemistries, when the battery degrades, its internal impedance and individual electrode capacities change, causing a change in its electrical performance including terminal voltage response, reduction of battery power, and reduction of battery available capacity. In addition to changes in electrical performance of the cell, dimensional changes are also observed. These changes are observed as an overall increase in battery thickness, thus affecting the stresses in the battery pack.

Battery expansion creates real-world challenges in battery pack design and battery state-of-health management. In the presence of battery pack external geometry constraints, the volume expansion exerts an outward pressure on the pack housing material, creating small deformations of the pack and leading to possible pack-level reliability issues. Battery expansion characterization requires large designs-of-experiments, since the magnitude of deformation depends not only on external loading constraints, but also on battery design, chemistry,

and use case, including current and temperature loads over a battery's lifetime. These realities further motivate the need for a high-throughput, low-cost, and accurate method for measuring battery expansion.

A typical life-test to quantify the changes in electrical and mechanical behavior, in an automotive laboratory environment, even with accelerated aging protocols (which may induce atypical aging side reactions compared to consumer usage), may take upwards of 18 months. While this may be relevant for the validation of performance for a design prior to product launch, lifecycle testing using the expected usage profile is prohibitively slow. To this end, automotive engineers must rely on virtual battery models that can accurately capture the beginning-of-life (BOL) performance, end-of-life (EOL) performance, and any state-of-life condition in between. This approach enables vehicle level performance specifications to virtually flow down from a vehicle level, to a system level, to a pack or module level, and finally to a battery cell level to be evaluated virtually. These tuned models assist the BMS in making decisions regarding allowable power limits and their effect on remaining useful life, reuse/resale value, and decisions on pack replacement, repurposing, or recycling. The performance metrics of the battery cell, such as Direct Current Internal Resistance (DCIR), peak operational power, heat generation, and volume expansion can then be captured and predicted virtually, and then extended back up the virtual system to the vehicle level in order to capture cycling performance, as well as traditional performance metrics such as all-electric range, 0-60 mile-per-hour acceleration time, and top speed.

The battery state of health (SOH) has been traditionally quantified as capacity loss and/or resistance growth. For packaging and safety reasons, the battery thickness change is also an important SOH metric. Understanding thickness changes will play an important role in accomodating these changes in the design of batteries including electrode materials and pack design. The rate of degradation depends heavily on the usage profile and environmental conditions. To better design systems with battery energy storage, we must understand and be able to predict all three changes in cell performance over life accurately, but the models for all three metrics have been traditionally done separately. We aim to connect the models for the three metrics and link battery expansion to battery degradation.

The focus of this thesis is to develop and parameterize reduced order models that predict the three SOH metrics of capacity loss, resistance growth, and thickness changes of multilayer pouch cells by connecting the most popular degradation mechanisms previously used to model the electrochemical performance of Lithium-ion batteries over their useful life.

1.2 Battery Degradation

There are several ways to model battery degradation [4]. Data-driven methods [5] are very flexible but require large amounts of data and can be hard to interpret. Empirical aging maps [6, 7, 8] are computationally fast, but require a proper design of experiments and proper statistical validation to ensure interpolation rather than extrapolation from the operating conditions [9], and are difficult to utilize in a virtual design scenario as mentioned above.

Physics-based battery models use systems of partial differential equations to describe the chemical and physical mechanisms in the battery to predict voltage response and dimensional changes as a function of the battery state of charge (SOC). These models require electrochemical and mechanical parameters that are the properties of materials used in the batteries in addition to parameters tuned to fit battery voltage and expansion response. Physics-based degradation models use additional systems of partial differential equations coupled with equations of physics-based battery models to describe the changes in battery electrical and mechanical response as the battery ages. We use physics-based models in this work as they offer insights into the degradation mechanisms occurring in the battery and provide us with a way to predict dimensional changes linked to battery aging. Physics-informed parameterizable models in the literature capture the capacity degradation of battery cells over life, [10], can be applied to various duty cycles, but they traditionally assume that the thickness and resistance of the battery cell electrodes do not change appreciably over life and seek to assign thickness and resistance changes in other manners. This dissertation aims to link battery thickness and resistance to degradation mechanisms and their associated states.

1.2.1 Degradation Mechanisms

A large number of chemical and physical mechanisms are responsible for battery degradation [11, 12]. Modeling all of these mechanisms and their interactions is extremely challenging because each mechanism has its own model parameters to be parameterized and the interactions between the mechanisms also has be considered [1]. This is why most physics-based models consider only the most dominant mechanisms. These are: Solid Electrolyte Interface (SEI) growth [13, 14, 15], lithium plating [16, 17], and particle cracking of the anode and cathode materials [18, 19].

The most commonly modeled aging mechanism is SEI formation and growth. SEI forms on the surface of the negative electrode (graphite) during the formation process of the cell[20],

[1] Additional degradation mechanisms include: SEI decomposition, current collector cracking and contact loss, lithium dendrite formation, transition metal dissolution in cathode, binder decomposition and contact loss, electrolyte oxidation at the cathode etc., which are not considered in this study

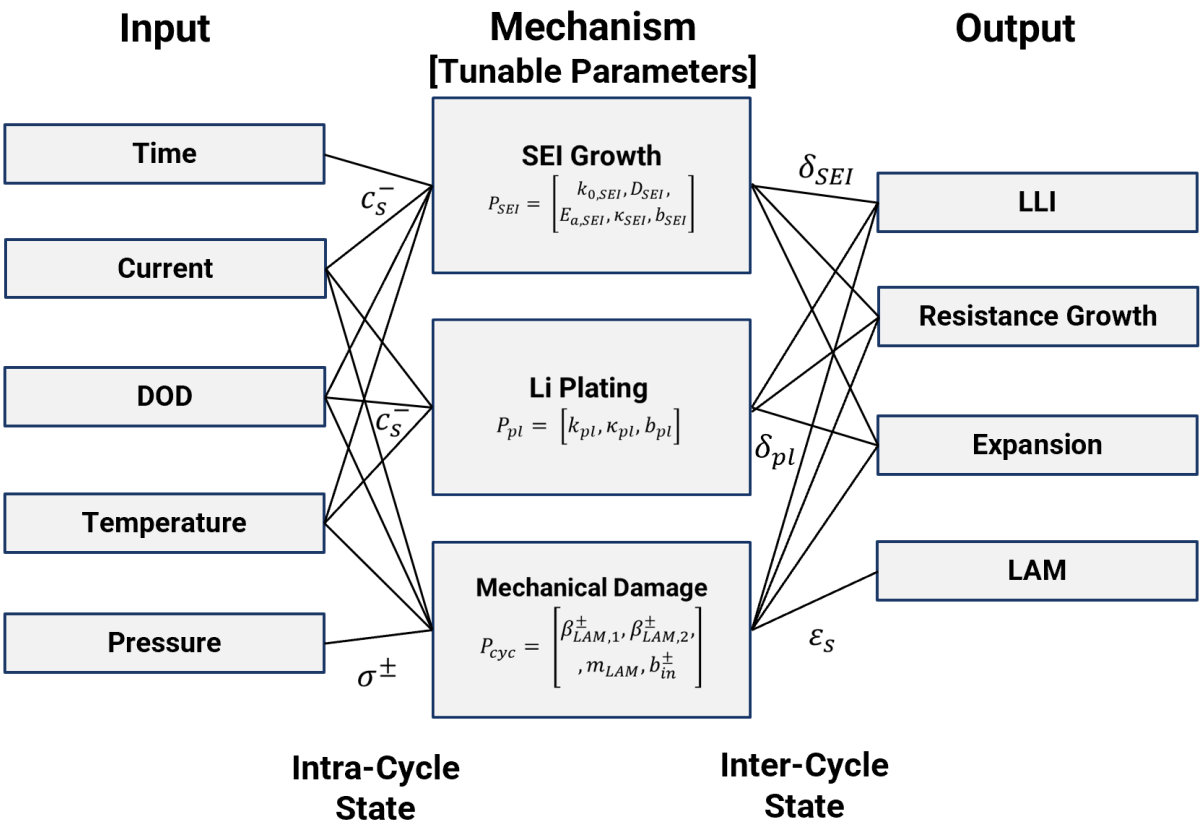


Figure 1.1: A Summary of inputs and outputs of the degradation model mechanisms.

from the reaction of lithium-ions with the electrolyte. This SEI layer initially protects the electrode against further reactions with the electrolyte but over time leads to loss of cyclable lithium, leading to capacity fade and also an increase in battery resistance. In this thesis we attribute part of the pouch cell irreversible thickness change to the growth of the SEI layer similarly to [2]

Lithium plating occurs when lithium-ions deposit as metallic lithium instead of intercalating in the electrodes. This leads to loss of cyclable lithium leading to capacity fade as well as safety issues like internal shorts caused due to dendrite formation. Lithium plating is also contributing to the irreversible battery thickness increase [21]. Lithium plating is commonly modeled using Tafel or Bulter-Volmer kinetics via the exchange current density of Li deposition that depends on the concentration of Li in electrolyte along the electrode [16, 22, 17].

The reduced order modeling approach used in this Thesis involves a Single Particle Model (SPM) approximation for modeling the lithium concentration inside a representative particle and assumes uniform intercalation current across the electrode. This uniformity assumption

isn't valid at high currents where plating is significant. High currents result in non-uniform intercalation current that is typically captured by higher order models such as SPMe that includes Li concentration gradients across the electrolyte [23] and P2D [24].

To address this limitation, we propose and implement in this thesis a novel low-order modification to the SPM modeling framework to capture the spatial non-uniformity in electrolyte concentration dynamics. After a single parameterization coefficient is determined using training data, the added dynamic state is effective in capturing the lithium plating kinetics that contribute to loss of lithium inventory for various cycling conditions that are different from the training conditions. The resulting lithium plating is then modeled as a film that contributes to resistance and thickness growth.

Last but not least, we also propose and implement numerically a novel low-order model for capturing the loss of active material associated with the particle fracture and isolation occurring during cyclic charging and discharging. When the batteries are cycled, the reversible expansion and contraction from lithium intercalation to the active particle leads to cycling stresses in the electrodes leading to fatigue damage of the electrode materials and leads to particle cracking of the electrode active materials [18, 25, 26]. This particle cracking causes loss of active material (LAM) and leads to capacity loss based on some parameterized degradation models [18, 27, 12] and the degradation mechanism is referred to as mechanical damage. These models are valid only when the battery cycling is symmetric (charge and discharge rates are the same) and fail to capture differences in LAM at different depth of discharges (DOD). Additional modifications to the model are required to capture mechanical damage when the battery cycling is asymmetric (charge and discharge rates are different) and at different DODs.

1.2.2 Tuning Degradation Models

One of the challenges of using these physics-based models is that simulating hundreds to thousands of cycles until the battery reaches its end of life can take hours, making model parametrization that fits experimental data difficult. Speeding up these aging simulations to a human timescale and can enable the physics-based models to be used as an engineering design tool. Many studies in literature focus on speeding up the simulation of intra-cycle simulations [4]. Our work simulates intra-cycle degradation, calculates changes in electrode state of health (eSOH) parameters, and extrapolating it inter-cycle using an adaptive algorithm [3]. Few studies exist in literature on tuning degradation model parameters with data [12, 28, 29]. Tuning of degradation model parameters is mostly done manually to reduce the error between simulation and data [12]. Global optimization techniques [30, 28]

are also used to tune model parameters using aging data for entire battery lifetime. These algorithms can take a long time to converge if the time to compute the cost function for each iteration is long. In this thesis we employ a novel technique of reformulating the inter cycle loss of lithium inventory that was co-developed with other lab mates to speed up the time for each iteration. We show how using accelerated simulations makes automatic tuning of degradation model parameters using aging data and optimization techniques like [31] computationally tractable.

1.3 Battery Expansion

Lithium-ion batteries are made of electrodes hosting lithium ions and they expand and contract as the lithium ion concentration changes and as they age. Over the course of a single charge-discharge cycle, lithium intercalation into and out of the active materials of both electrodes induces reversible expansion and contraction of the crystal lattices. A mismatch in the resulting net volume change of the positive and negative electrodes results in an overall, macroscopic volume change of the entire battery. Such is the case for most commercial lithium-ion batteries comprising a graphite negative electrode and a metal oxide positive electrode. These volumetric changes can be measured either by the bulk force [32] or expansion measurements [33] and provide better means to estimate the State of Charge (SOC) [34] of the batteries as this expansion is reversible and is a function of battery SOC. There are challenges in utilizing mechanical measurement which include difficulties in instrumenting the force/expansion sensors in packs [35] and additional sensor cost [36].

1.3.1 Link between Degradation and Expansion

Another component of battery expansion is the irreversible expansion that occurs in addition to reversible expansion as the battery ages. While reversible expansion is based on the SOC of the battery, irreversible expansion is related to the SOH of the battery. Along with the capacity loss due to battery aging, a corresponding increase in cell thickness is observed [37, 38, 2, 39, 1].

Cannarella et al. [37] observe a linear relationship between the battery stack stress to cell SOH for cells aged under different cycling parameters. This increase in stack stress was attributed to irreversible volume expansion of the electrodes caused due to SEI growth. A simple phenomenological model was also proposed to correlate SOH with stress increase. Jones et al. [38] measured in situ the deformation of graphite composite electrodes and correlated the irreversible electrode deformation with the formation and growth of the SEI.

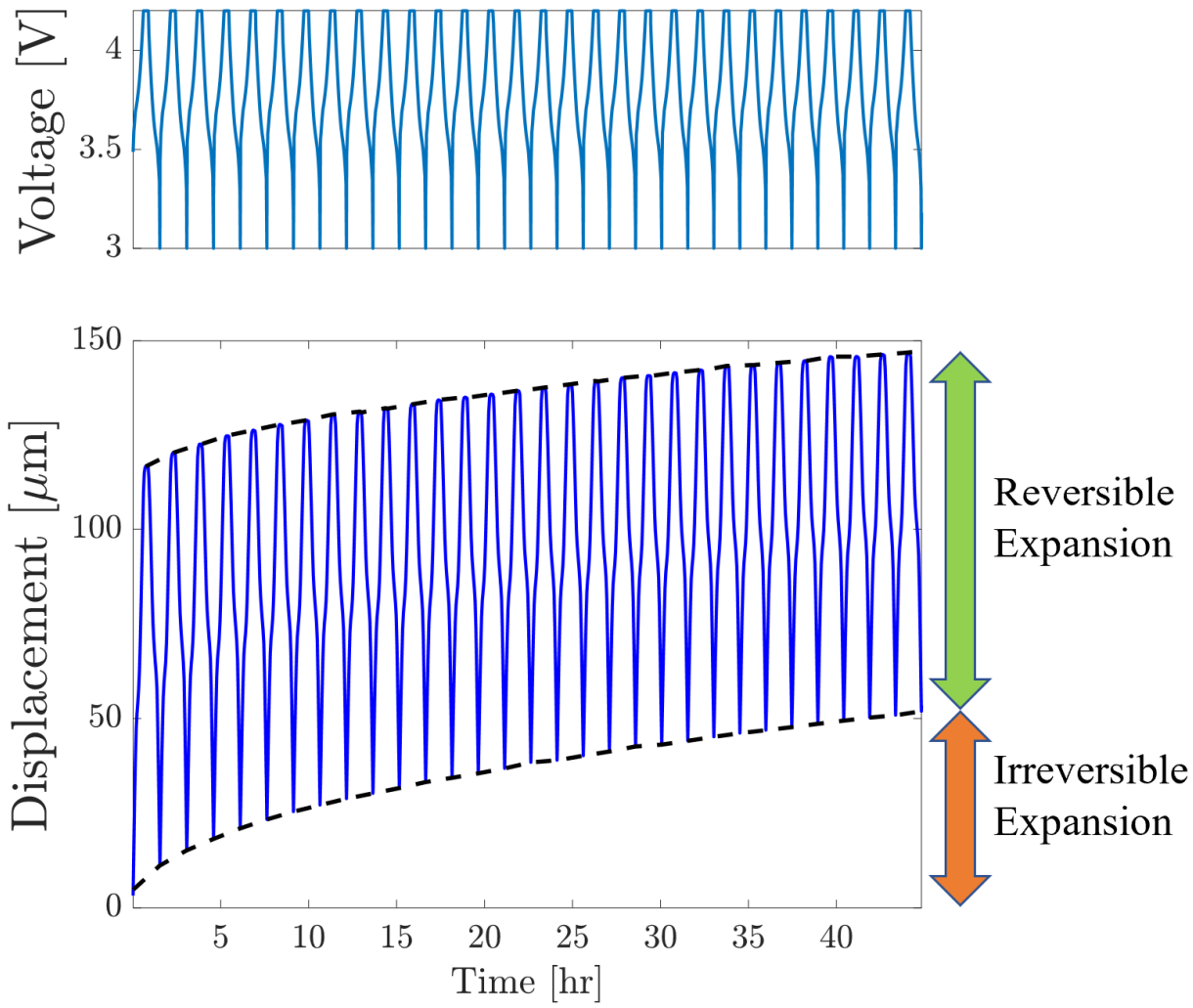


Figure 1.2: Voltage and battery expansion response over several cycles. The expansion within one charge-discharge cycle is reversible, while the expansion over many cycles is irreversible, as reported in [1]. The lower bound of the expansion plot shows the irreversible battery expansion, while the difference between the lower and upper bounds shows the reversible expansion.

They also found that the choice of polymer binder affects the irreversible electrode deformation considerably. This suggests that the physical properties of the electrode components can have a significant influence on the irreversible expansion of the battery. Louli et al. [2] used operando pressure measurements to detect irreversible volume expansion of constrained pouch cells of various positive and negative electrode chemistries. They found that irreversible pressure growth is inversely proportional to capacity fade due to loss of lithium inventory (LLI) to SEI growth. A schematic showing the thickness change due to SEI is shown in Fig. 1.3. The formation of SEI was verified by X-ray photoelectron spectroscopy

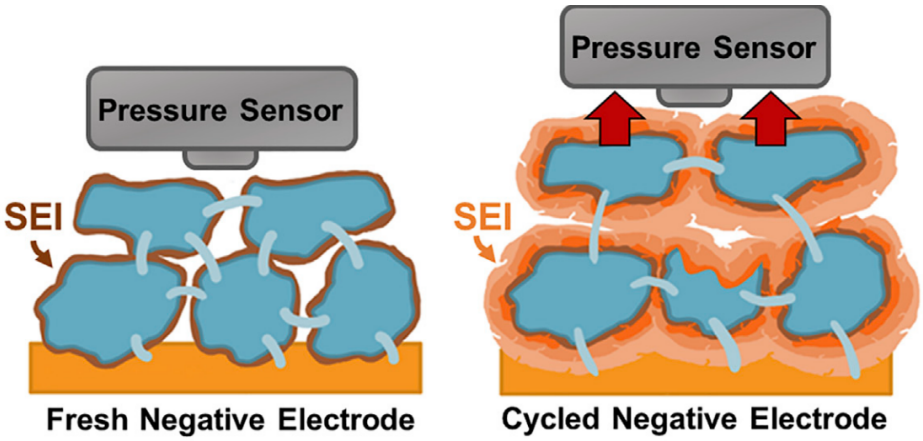


Figure 1.3: Change in thickness due to SEI growth. Figure from [2]

measurements. Willenberg et al. [39] found that the characteristic curves shape of the diameter changed over aging and observed a direct correlation between this diameter change and the capacity loss of the battery. Mechanical impedance was used by von Kessel et al. [40] to study and model the mechanical behavior of lithium-ion cells. The authors found that as the battery ages, mechanical stiffness also increases in addition to the cell thickness growth. Samad et al. [35] found that the features of the expansion force-based Incremental Capacity Analysis (ICA) change as the batteries age and can be considered as indicators of battery aging.

Hahn et al. [41] used the mechanical impedance in addition to other scanning electron imaging and elemental analysis to analyze the cause of irreversible expansion. Their findings reveal that the cause of irreversible expansion is primarily anode-dominated growth attributed to SEI growth in addition to isolated metallic lithium formed due to lithium plating. Based on these findings, they developed a relaxed 1D force equilibrium model that predicts module pressures for fresh as well as aged cells based on cell properties, cell aging data, and module design. Deich et al. [21] studied the effects of module stiffness and initial compression on cell aging. They found that the aged negative electrodes showed a 3-6 % increase in thickness compared to a fresh cell. A cell that has a higher thickness increase also exhibited non-uniform surface depositions indicating additional thickness change due to lithium plating. Positive electrodes had more variability in their thickness changes. Some cells showed a slight increase in thickness and others a slight decrease. Cross-section SEM micrographs revealed an increase in positive electrode particle cracking under higher pressure. The authors also modeled the decrease in battery capacity as mechanical degradation due to fatigue damage using Wölher curves.

Mohtat et al. [1, 42] studied the correlation between reversible and irreversible battery

expansion and battery aging. While irreversible expansion increased as the battery capacity decreased across cells cycled under various conditions, a clear correlation between cycling conditions and irreversible expansion wasn't observed. Meanwhile, the reduction in reversible expansion as the battery aged showed an excellent correlation to the capacity loss.

While some of the studies model irreversible expansion empirically, we employ reduced-order electrochemical models and physics-based degradation processes to predict the cell's irreversible thickness change throughout its lifecycle. A physics-based model that predicts irreversible expansion based on battery degradation mechanisms can help design battery packs for improving battery life.

1.3.2 Sensing Expansion

Expansion measurements for cells under various cycling conditions are necessary to tune the degradation model introduced in this thesis. Accurate lithium-ion battery state-of-health estimation remains a critical function in modern battery management systems, especially as the quantity and diversity of battery technologies continue to increase due to the global push towards vehicle electrification. A promising indicator of battery state-of-health is the battery expansion, which was shown to be strongly correlated to battery lifetime by [1], and can thus potentially be used to improve state-of-health estimation algorithms. The need for accurate calibration of state-of-health estimation algorithms motivates the development of sensor platforms that can enable high-resolution, high-throughput measurements of battery expansion under various load conditions.

Several sensor configurations for measuring battery expansion has been reported in the past. [39] used strain gauges to monitor strain on cylindrical cells. [1] used commercial linear displacement sensors to measure the thickness expansion of pouch cells. [34] used a load cell to measure the expansion force in a lithium-iron phosphate prismatic cell. While these devices enable high-accuracy battery expansion measurements, the complexity in test setup and the usage of specialized measurement equipment prevents wider adoption of such techniques.

1.3.3 Impact of Pressure

Prior research on the effects of externally applied pressure on battery cycling performance studied the impact of external loading on the volumetric changes in the porous components of the battery and modeled it using rock mechanics [43, 44]. At higher external loading, the changes in electrode dimensions are lower, and hence, changes in electrode porosity are higher, thus affecting the battery response, mostly in the form of battery resistance.

The effect of external loading is different in different components of battery because the mechanical properties like Young's Modulus are different [45]. However, these works don't study the effect of battery pressure on lifetime aging.

There are also other works that have studied the effect of pressure on resistance growth as the battery ages and the linked capacity fades [46, 47]. Applied pressure effects separator creep and the wettability of the electrode [46]. At higher pressure, there is increased creep and consequently higher resistance, but the higher wettability of the electrode reduces resistance. Thus the resistance growth of the battery is lower at low pressure (0 kPa) and high pressure (2000 kPa) but is higher at medium pressures (1000-1500 kPa). But, at the pressures studied in this thesis (0-172 kPa), the effect of separator creep and wettability is minimal and doesn't explain the observed impact of pressure on degradation. Studies by [48, 49] show us that there is low lithium plating and, thus, less capacity fade at higher pressures. But, this doesn't explain the lower loss of active material (LAM), which isn't effected by lithium plating, at higher pressures in the cells studied in this thesis.

The works discussed above mostly focus on the electrochemical response of the battery aging: capacity fade and resistance growth. There have been few works that try to analyze the impact of pressure on battery expansion. The impact of module stiffness and initial compression on battery aging was studied in [21]. They found out that high pressure, high module stiffness results in larger capacity loss and large resistance. Medium pressure and low module stiffness result in high swelling, and finally, low pressure also results in high swelling. An experimental study of effect of externally applied pressure on battery degradation was done in [1]. They have shown that as pressure increases on the battery, the battery swelling, resistance growth, and capacity loss decrease. Data-based modeling on the impact of pressure on capacity and battery expansion was done by [50]. While they used a physics-based model for predicting battery expansion, the degradation model was data-based.

While the above works have shown us the impact of pressure on battery performance and aging, this thesis will provide a physics-based model parameterization of the effect of pressure on battery aging and specially graphite particle fracture and loss of active anode material.

1.4 Dissertation Organization

The main contribution of this work is to model and predict the battery expansion, resistance growth, and capacity as it degrades. This has been done by modeling and simulating battery degradation, developing a framework to tune degradation model parameters from experimental data, developing sensor to measure expansion as the battery ages, and modeling battery

expansion as it ages. The contributions of the thesis are summarized as follows:

In Chapter 2, we develop a novel displacement sensor to measure expansion. The sensor uses commercially available inductance to digital converters (LDC) to measure battery expansion by measuring changes in the inductance of the sensor coil. Battery expansion causes movement in the attached aluminum plate, which serves as the conductive target for the sensor coil. The movement in the conductive target located in the sensor coil's AC magnetic field causes a change in the inductance of the sensor coil. The change in inductance is measured using an LDC chip. The advantage of this sensor is that it is cheaper compared to state-of-the-art expansion measurement techniques used to measure battery expansion. This enables us to measure expansion data of a large number of batteries at the same time at a lower cost, thus helping us understand the relationship between battery expansion and degradation.

This chapter is based on the following work:

- **S. Pannala**, A. Weng, I. Fischer, J. B. Siegel, and A. G. Stefanopoulou, "Low-cost inductive sensor and fixture kit for measuring battery cell thickness under constant pressure" Modeling, Estimation and Controls Conference - IFAC-PapersOnLine, vol. 55, no. 37, pp. 712–717, 2022.

Chapter 3 of the thesis introduces the reduced-order battery model used for voltage response. A battery expansion model that links lithiation states in the reduced-order battery model to particle stress and strain is also described in this chapter. Particle strain results in electrode expansion and thus, battery reversible expansion. Particle stress results in mechanical damage of the electrodes and thus, capacity loss.

This chapter is based on the following work:

- **S. Pannala**, P. Valecha, P. Mohtat, J. B. Siegel, and A. G. Stefanopoulou, "Electrochemical Battery State Estimation under Parameter Uncertainty Caused by Aging Using Expansion Measurements" American Controls Conference (ACC), 2022.

Chapter 4 of the thesis introduces the degradation mechanisms in the model. Extensions to existing mechanical damage and Li plating models are added to improve degradation prediction at high C-rates, asymmetric charging and discharge rates, and different DODs. The irreversible expansion and resistance growth is attributed to SEI growth, lithium plating, and the mechanical damage degradation mechanisms.

This chapter is based on the following works:

- **S. Pannala**, H. Movahedi, T. R. Garrick, J. B. Siegel, and A. G. Stefanopoulou, "Consistently Tuned Battery Lifetime Predictive Model of Capacity Loss, Resistance

Increase, and Irreversible Thickness Growth" Journal of The Electrochemical Society, vol. 171, no. 1, p. 010532, 2024.

Chapter 5 of the thesis develops a framework to automatically tune physics-based degradation model parameters using battery aging data. This framework utilizes accelerated battery aging simulations to speed up aging simulations to human timescales, leading to faster and easier parameterization of models. Calendar aging data was used to tune SEI model parameters, and the cycling data was used to tune mechanical degradation and Li plating parameters for cells cycled at low currents. The fit between model and data is good across both cycling and calendar aging, and the model even predicts aging in conditions that were not used for parameter tuning. This model can predict battery capacity, loss of lithium inventory, and eSOH parameters using only a single set of parameters.

This chapter is based on the following works:

- V. Sulzer, P. Mohtat, **S. Pannala**, J. B. Siegel, and A. G. Stefanopoulou, "Accelerated Battery Lifetime Simulations Using Adaptive Inter-Cycle Extrapolation Algorithm," J. Electrochem. Soc., vol. 168, no. 12, p. 120531, 2021.
- **S. Pannala**, V. Sulzer, J. B. Siegel, and A. G. Stefanopoulou, "Methodology for Accelerated Inter-Cycle Simulations of Li-ion Battery Degradation with Intra-Cycle Resolved Degradation Mechanisms" American Controls Conference (ACC), 2022.
- **S. Pannala**, H. Movahedi, T. R. Garrick, J. B. Siegel, and A. G. Stefanopoulou, "Consistently Tuned Battery Lifetime Predictive Model of Capacity Loss, Resistance Increase, and Irreversible Thickness Growth" Journal of The Electrochemical Society, vol. 171, no. 1, p. 010532, 2024.

In Chapter 6 of the thesis, we extend the model developed in Chapter 4, to capture degradation of cells cycled under various externally applied pressures. First, we develop ways to analyze aging metrics of cells cycled under various pressures from cycling data, including resistance growth and irreversible expansion, which are usually estimated using characterization tests. Then, we introduce the dependency of pressure in the degradation mechanisms and finally predict the dependency of aging mechanisms on pressure.

1.5 Contributions

First, a novel battery expansion sensor is developed to enable measurement of battery expansion under constant pressure using the principle of inductive sensing. The sensor uses

commercially available inductance to digital converters to measure the changes in inductance of the sensor coil due to changes in the space between the coil and a plate that follows the battery swelling. The cost of the new sensors, the programmable interface and the data acquisition make it possible to apply in laboratory setting for lifetime testing of a large number of cells typically needed for degradation studies.

Second, we modified the multiphysics mechanical damage models to better link them to the reduced-order electrochemical model known as the single particle model (SPM). This was done by introducing an equivalent stress that adjusts for non-zero mean stress and concentration dependence of stress to the mechanical damage model. We also modified the Lithium plating model to capture the high-concentration gradients across the electrode that the SPM cannot capture. This was done by adding a current-dependent dynamic term to account for the spatial nonuniformity of electrolyte dynamics at higher currents.

Third, we introduce a parameterization methodology that leverages accelerated aging simulations to speed up the tuning process. The tuning is performed in three sequential steps, where we first use the calendar aging data to tune the SEI mechanism. Tuning the mechanical damage model and the Lithium plating model is done simultaneously during the second step. The third and innovative tuning step addresses the resistance and expansion predictions. This work shows that a single set of parameters can predict capacity loss, resistance growth, and irreversible thickness change as the battery ages, even for cycling conditions not used for parameter tuning.

Finally, the effects of externally applied pressure on capacity loss, resistance growth, and irreversible expansion are studied and modeled. The aging data shows us that the dominant degradation mechanism of negative electrode mechanical damage is pressure-dependent, and tuning it to match negative electrode loss of active material (LAM) at various pressures captures the dependence of capacity loss, resistance growth, and irreversible expansion on pressure.

CHAPTER 2

Development of Inductance Based Expansion Sensor

2.1 Introduction

Extensive battery testing is needed to understand battery expansion and degradation. Battery degradation rate is a function of cycling conditions such as current (C-rate), temperature, depth of discharge, and pressure. To build a model that can predict irreversible expansion and aging, we need to collect a lot of expansion data for cells cycled under several combinations of cycling conditions. Additionally, we need to test 2-3 cells per test condition to account for cell-to-cell variability and outliers. Thus, we require testing equipment, including expansion sensors, which can measure and quantify the expansion across hundreds of cells that are cycling under different cycling conditions.

Several sensor configurations for measuring battery expansion have been reported in the past. Strain gauges were used by [39] to monitor strain on cylindrical cells. Load cells are used in several studies to measure the expansion force in a lithium-iron [34, 35, 2, 37] across both prismatic and pouch cells. Commercial linear variable differential transformer (LVDT) displacement sensor (Keyence GT-2) was used by [1] to measure the thickness expansion of pouch cells. A key limitation of this sensor design is revealed after considering that accurate calibration of predictive state-of-health models will require life cycle testing on dozens, if not hundreds, of test conditions [51]. The commercial sensor, costing $2000 per device, becomes quickly cost-prohibitive as the size of the experiments increases. Thus, we need a low-cost and accurate expansion sensor with a simple design to scale to hundreds of experiments.

In this chapter, we report on a battery expansion sensing platform based on the principle of mutual inductance in metallic conductors. The viability of inductive proximity sensing was shown in thin-film eddy current sensors developed by [52] to measure expansion in a battery pack setting. The contribution of this chapter is using off the shelf inductance to

digital converter (LDC) chips from Texas Instruments and printed circuits boards (PCB) which makes the sensing platform easy to replicate.

Our sensing platform, henceforth referred to as inductive displacement sensor (IDS) and illustrated in Fig. 2.1, enables cost-effective and high-throughput measurements of battery expansion without sacrificing sensor accuracy. We demonstrate that our sensor design enables expansion measurements with sufficiently high accuracy to parameterize battery aging models within 3% capacity prediction accuracy. To our knowledge, this work represents the first report of the application of inductance proximity sensors to accurately measure battery expansion. The current work focuses on measuring expansion of lithium-ion pouch cells. However, the fundamental concepts introduced in this chapter can also be applied to measure expansion of prismatic and cylindrical cell formats.

The chapter is organized as follows. We begin by discussing the theory and application of mutual inductance for battery expansion sensing (Section 2.2). Afterwards, we describe the experimental setup and testing protocol (Section 2.3). Finally, we discuss the key performance metrics of the proposed sensor suite (Section 2.4).

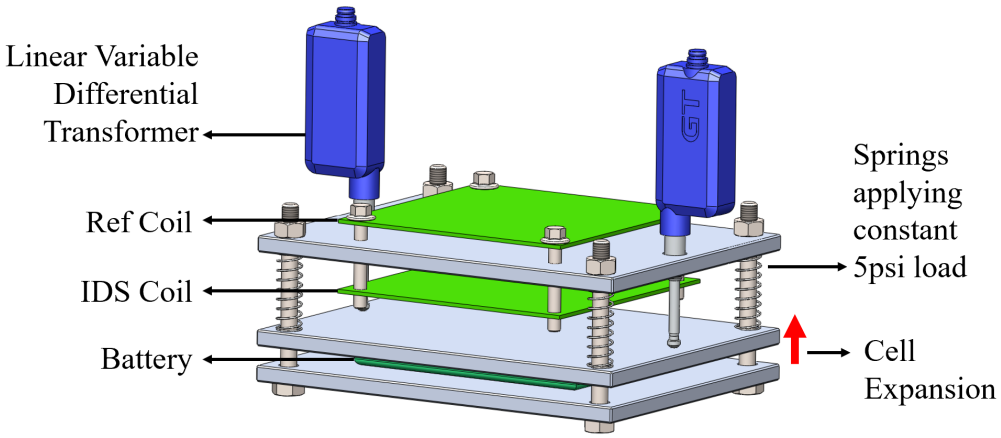


Figure 2.1: The fixture used to measure expansion. The battery is placed between two aluminum plates. The plate above the battery moves in the direction shown by the red arrow when the battery expands and both the IDS (Inductive Displacement Sensor) and LDVT sensors capture this displacement. Reference coil is placed at a fixed distance from the top plate and the readings from this coil is used to compensate for environmental effects.

2.2 Theory and Design of an Inductance-Based Expansion Sensor

This section describes the operating principle of the inductive displacement sensor (IDS) and the design considerations of the sensor coil and the metal target.

2.2.1 Operating Principle

The inductance based displacement sensor uses an inductance to digital converter (LDC) chip along with a inductive sensor coil and a capacitor to measure expansion. The sensor chip generates an alternating current magnetic field through the sensor coil which is printed on a circuit board. Since the sensor consists of commonly available electrical components the cost of the sensor is less than $20, which is much lower compared to the LVDT sensor. The operating principle of the IDS sensor is summarized in Fig. 2.2.

If a conductor is present in the magnetic field, eddy currents are induced on the conductor's surface. Lenz's law states that an induced current flows in a direction such that the current opposes the magnetic field that induced it, thus reducing the sensor coil's magnetic field. The sensor coil and the capacitor form an RLC tank circuit with a resonant frequency given by:

$$f = \frac{1}{2\pi\sqrt{\mathrm{LC}}} \tag{2.1}$$

where f is the sensor resonant frequency, L is the coil inductance and C is the capacitance. The sensor chip measures this resonant frequency and calculates sensor inductance using Eq. (2.1) and converts it to a digital value that a micro-controller can read. The value of this resonant frequency increases when the sensor coil's magnetic field is reduced due to the eddy current, and this change is captured by the sensor chip. The change in f is directly proportional to the distance between the coil and the metal target.

2.2.2 Coil Design

For our application of measuring battery expansion in a single direction, a flat spiral inductor coil configuration was used. The aim of designing coil features is to maximize the quality factor (Q) of the sensor given by:

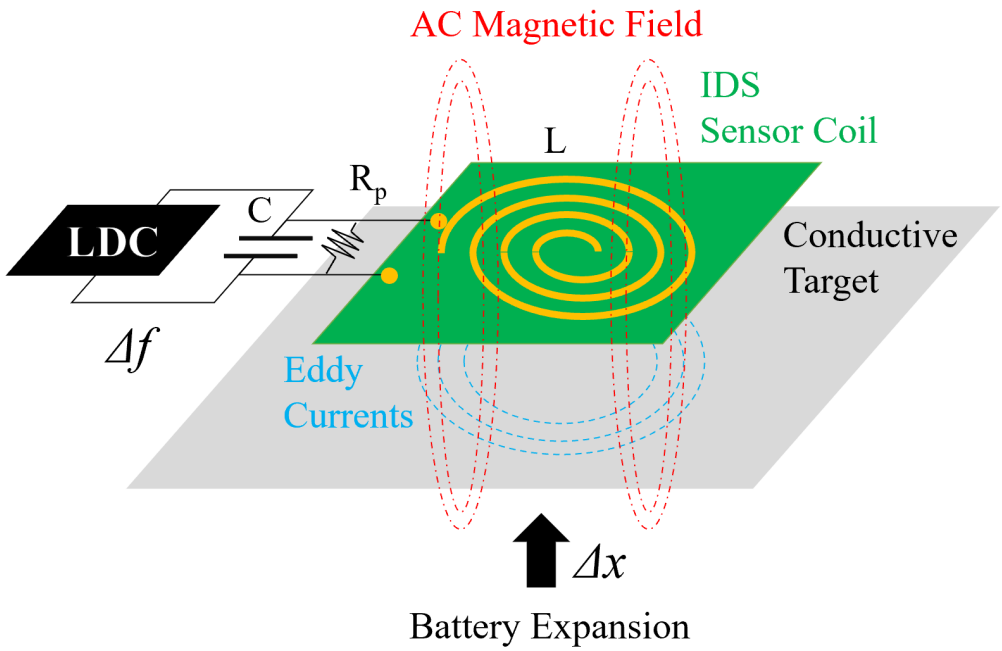


Figure 2.2: Principle of operation for an inductance-based battery expansion sensor.

$$\mathrm{Q} = \mathrm{R_p}\sqrt{\frac{\mathrm{C}}{\mathrm{L}}} \tag{2.2}$$

where R_p is the parallel resistance of the RLC tank circuit.

The inductor size was chosen to maximize the linearity in signal response for the range of displacements to be measured. The number of coil turns had to be sufficiently high to improve the inductance signal strength, but increasing the number of turns also decreases the ratio of d_{in}, the inner coil diameter, and d_{out}, the outer coil diameter, which must be kept greater than 0.3 for high quality factor. A coil with 28 turns gives $d_{in}/d_{out} = 0.44$. The coil was printed on both sides of the circuit board to maximize total inductance. The capacitor used was a C0G-grade ceramic capacitor as recommended by the manufacturer. Lower capacitors can cause parasitic interactions with the capacitance of the spiral coil. The capacitor was placed as close as possible to the inductor to minimize the parasitic resistance due to traces between the inductor and capacitor. We have selected 270 pF as our capacitance so that the sensor operating frequency is around 1 MHz and is within the specification frequency range of the LDC chip and is less than the self-resonant frequency (SRF) of the coil. The sensor frequency needed to be less than 75% of the SRF to prevent parasitic interactions.

The above design values results in a sensor inductance of 80 μH, parallel resistance $R_p = 29\,\text{k}\Omega$ and quality factor $Q = 52$. The coil design properties are summarized in Table 2.1.

Table 2.1: Coil design parameters.

Parameter	Value
Inductor size (d_{out})	1.6 in.
Number of turns	28
Number of layers	2
Trace width	8 mils
Capacitance	270 pF
Copper thickness	2 oz-cu

2.2.3 Target Design

The conductive target is to be placed parallel to the sensor coil so that the change in distance of the conductor is in the axial direction of the sensor. This conductive target is placed next to the battery whose expansion we need to measure, so when the battery expands, it causes a corresponding displacement in the conductive target. Design factors for the conductive target include the size, material, thickness, and the distance to the sensor coil. The size and thickness of the target was chosen to be sufficiently large to permit maximal eddy current generation in the target. The material used was aluminum which has sufficiently high conductivity to support eddy current generation. In setting the distance between the coil and the target, we considered that the sensitivity of measurement for IDS sensor is greatest when the separation distance is within 20% of the coil diameter. For our setup, this corresponded to a separation distance of 8mm.

2.3 Experimental Setup

In this section we first discuss the experiment fixture which houses the battery and to which sensors that measure expansion are attached. Then we give a summary of experiments which are conducted to measure the battery expansion and sensor performance of the IDS sensor.

2.3.1 Fixture

A schematic of the fixture with the IDS sensor, and the optional temperature calibration and higher accuracy sensors is shown in Fig. 2.1. The fixture consists of three aluminum plates connected through bolts. The battery used for testing is an aged pouch cell (Cathode:

NMC111 Anode: Graphite) with 5 Ah nominal capacity. The battery is placed between the bottom and middle aluminum plates with polyurethane sheets on the top and bottom surfaces to ensure uniform pressure on the battery surface. The usage of these sheets also mitigates non-uniformity in battery expansion across the electrode plane to a degree. Springs are placed between the middle and top aluminum plates provide pressure on battery surface to ensure electrical contact between pouch cell layers. The springs (0-172 kPa) used in this work are softer than the polyurethane sheets (300 kPa). Hence, as the battery expands the springs change length, but the stress on the polyurethane sheets doesn't change significantly. Therefore, we can assume that the thickness of the polyurethane sheets don't change a lot during the aging tests and the only expansion we're measuring is the expansion of the battery. The sensor coil hangs at a fixed distance from the top plate. The middle plate moves upward when the battery expands. The sensor coil detects this change in displacement of the middle place. The reference coil is placed at a fixed distance from the top plate and its measurement is used to compensate for environmental effects like temperature changes. LVDT sensors from Keyence are also used to measure displacement of the middle aluminum plate. These sensors are used to calibrate and compare the IDS sensor measurement.

2.3.2 Testing Procedure

The fixture is placed in a thermal chamber that can be used to change the environment temperature. The cells are cycled using a Biologic cycler. We perform two tests on the battery:

1. **GITT:** A galvanostatic intermittent titration test is performed on the battery. The purpose of this test to calibrate the IDS sensor response using the LVDT sensor. The test first performed at room temperature 25°C and then at higher temperature 45°C to analyze sensor performance at multiple temperatures. The cell is first charged using CC-CV protocol at C/3 C-rate. Then, the fixture is allowed to reach steady state for 2 hours. After this, the GITT is performed at C/3 discharge rate with 10% SOC intervals with 2 hour rests between each discharge to allow the fixture to reach steady state. These steady state sensor reading from both the IDS sensor and LVDT sensor are used for creating a calibration curve for the IDS sensor and also for further analysis.

2. **Cycling:** The cell is cycled at C/3 charge and discharge rate for 5 cycles. The purpose of this test is to compare the IDS sensor readings which are calculated using the calibration curve obtained in the previous test with the LVDT sensor readings and to calculate and analyze the sensor error.

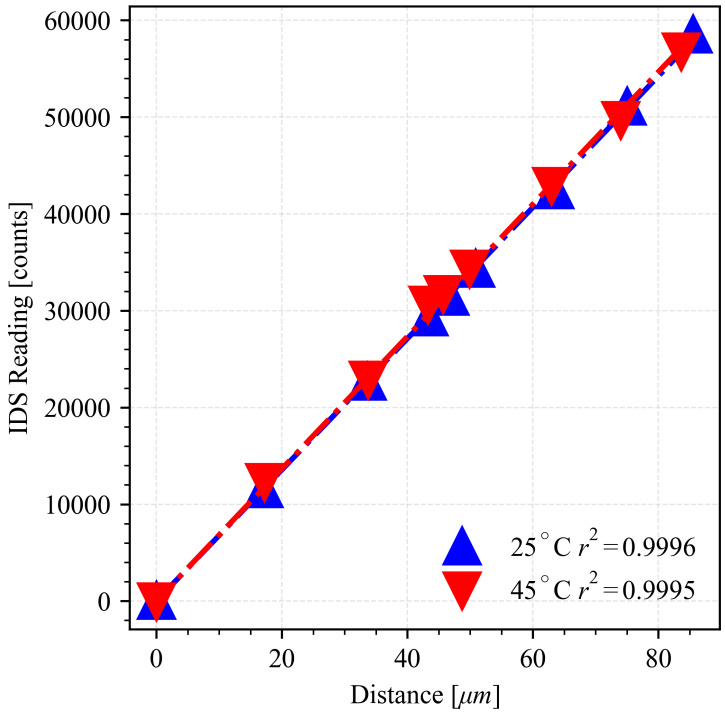


Figure 2.3: IDS sensor reading in sensor counts vs LDVT distance in μm at 25°C and 45°C. We can observe that the relationship between IDS sensor reading and distance is linear with $r^2 > 0.999$ at both temperatures. The slope of the graph is 680 counts/μm at both temperatures.

2.4 Results and Discussion

In this section we will take a look at the sensor calibration at multiple temperature, uncertainty in sensor measurement, and the sensor performance compared to LVDT sensor in both expansion and the differential expansion signals.

2.4.1 Calibrating Sensor

For calibrating the sensor we take sensor data for both IDS and LVDT sensors at 25°C and 45°C. The data points considered for the calibration curve include the steady state expansion measurements taken during the test period after the discharge pulses of GITT. The results are shown in Fig. 2.3. The x-axis of the figure shows the expansion measurement in μm measured by the LVDT sensor. The y-axis shows the reading of the IDS sensor in counts. The IDS sensor reading has a linear relationship with the sensor frequency. The initial sensor values is subtracted for better readability. As we see in the figure, the IDS sensor measurement is linearly proportional to the LVDT distance measurement at both

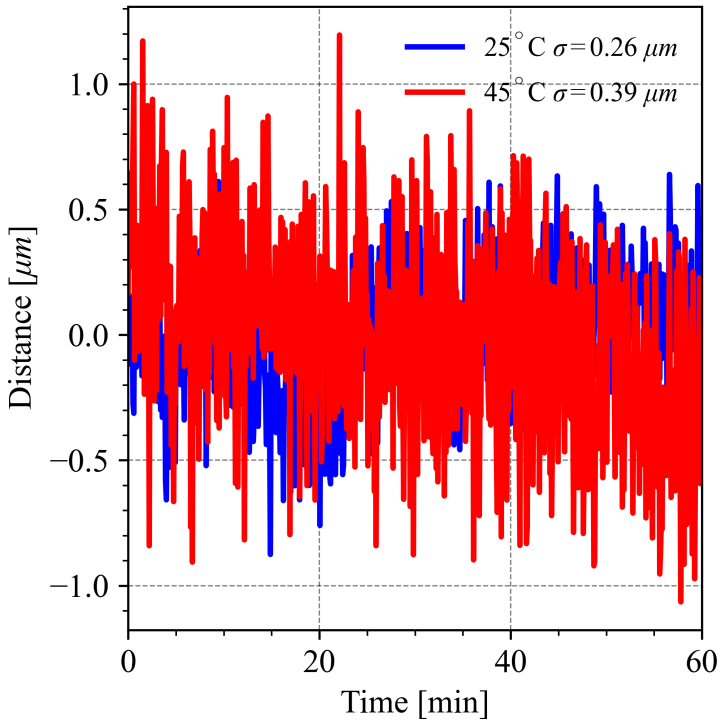


Figure 2.4: Steady state IDS sensor measurement in μm for 1 hour. The sensor measurement has a noise with standard deviation of 0.26 μm at 25°C, and 0.39 μm at 45°C. These values could be considered as the practical resolution for the sensor.

temperatures with coefficient of determination $r^2 > 0.999$. The slope of the graph si $m = 680$ counts/μm at both temperatures. This means that the IDS reading changes by 680 counts when the battery expands by 1 μm. Thus, we can convert the IDS measurement to distance in μm by using:

$$IDS_{\mu m} = \frac{IDS_{\text{counts}}}{m} \tag{2.3}$$

We will use this converted measurement in all further analysis.

2.4.2 Uncertainty in Measurement

The next step is to analyze the uncertainty or the noise in the IDS sensor measurement. To do this we observe the measurement data at steady state for 1 hour at 25°C and 45°C and this is plotted in Fig. 2.4. The x-axis shows the time in minutes and y-axis shows the IDS sensor measurement at steady state converted from counts to μm. The sensor signal is filtered by averaging 100 sensor readings for 5 seconds giving us a sample rate of 5 seconds. Furthermore, median filtering with a window of 11 samples is also performed to

remove the outliers in sensor measurement. Sensor filtering will help reduce noise but can limit the practical C-rate at which measurement can be made. The standard deviation σ of the measurement signal is $0.26\,\mu m$ at 25°C, and $0.39\,\mu m$ at 45°C which is an indicator of sensor noise and is an indicator of uncertainty in sensor measurement. We observe that the measurement signal is noisier at higher temperatures and hence the practical resolution of the sensor is lower at higher temperatures.

2.4.3 Performance of Sensor during Battery Cycling

We compare the performance of the IDS sensor against the LDVT sensor during battery cycling tests which is the most common use case of the sensor. The battery cycling protocol was discussed in the previous section and the results of the testing is shown in Fig. 2.5. Panel a) in the figure shows battery voltage in volts plotted against testing time in hours. Corresponding battery expansion is shown in panel b) where the blue line indicates the IDS expansion measurement and the red line indicates the LVDT measurement. We can observe that the IDS and LVDT sensor measurements are in good agreement with each other. The error in expansion measurement is shown in panel c). The maximum error in measurement is 3.2 μm and RMSE is 0.7 μm. The RMSE in measurement is lower than the sensor resolution ($1\,\mu m$) of the LVDT sensor. The maximum error of measurement is also within the sensor target performance metrics discussed previously.

2.4.4 Differential Expansion

In this section, we compare the differential expansion signals of the two sensors for a C/3 charge. [42] showed that certain prominent features in the second differential of the expansion (henceforth referred to as DE) signal with respect to battery charge, $\frac{d^2\delta}{dQ^2}$, change as the battery ages and these can be used as indicators for battery health. Thus, measuring the location of these features can be used as an indicator of sensor performance in regards to measuring battery SOH. We compare the location of these features from the DE signal of both IDS and LVDT sensors in Fig. 2.6. These features are referred to as P_1 and P_2 in the figure. The first feature P_1 is the location of local maximum in the DE signal. It can be observed that the location of this feature is almost identical for both the sensor measurements. The error in the feature location is 0.02 Ah ($\approx 0.5\%$ SOC). The second feature P_2 is the location of zero crossing of the DE signal. We can see that the error in the location of P_2 is larger than P_1 and the value is 0.08 Ah ($\approx 2\%$ SOC). Due the aforementioned errors in P_1 and P_2, the IDS sensor will underestimate the graphite electrode state of health.

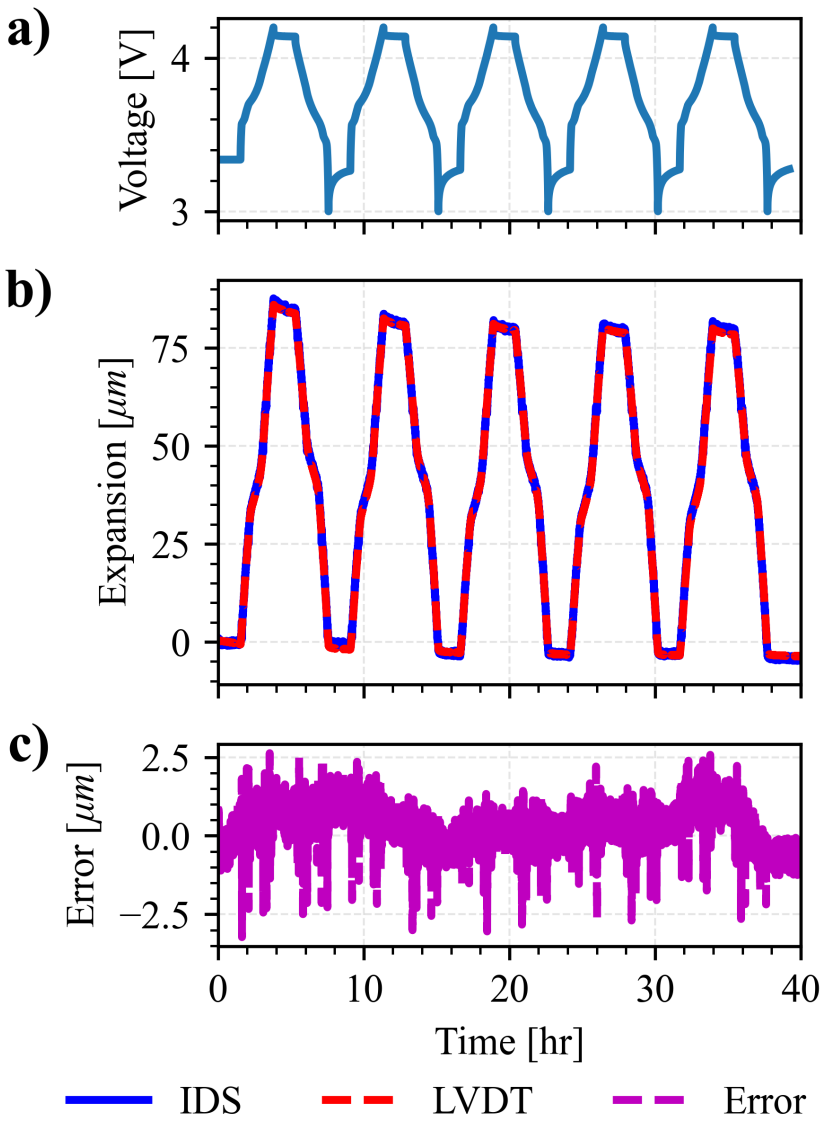


Figure 2.5: Comparing IDS expansion measurement with LDVT expansion measurement for a cell cycled at C/3 current for 5 cycles. Panel a) shows voltage response of the battery. Panel b) shows the expansion measurement plotted for both IDS and LVDT sensors. panel c) shows the error in measurement between IDS and LVDT sensors. Maximum error is 3.2 μm and the RMSE is 0.7 μm.

2.5 Conclusion

In this chapter, we developed an inductive displacement sensor (IDS), which uses the principle of mutual inductance to measure battery expansion. Design considerations for the sensor and the measurement target are discussed. The sensor measurement is shown to be

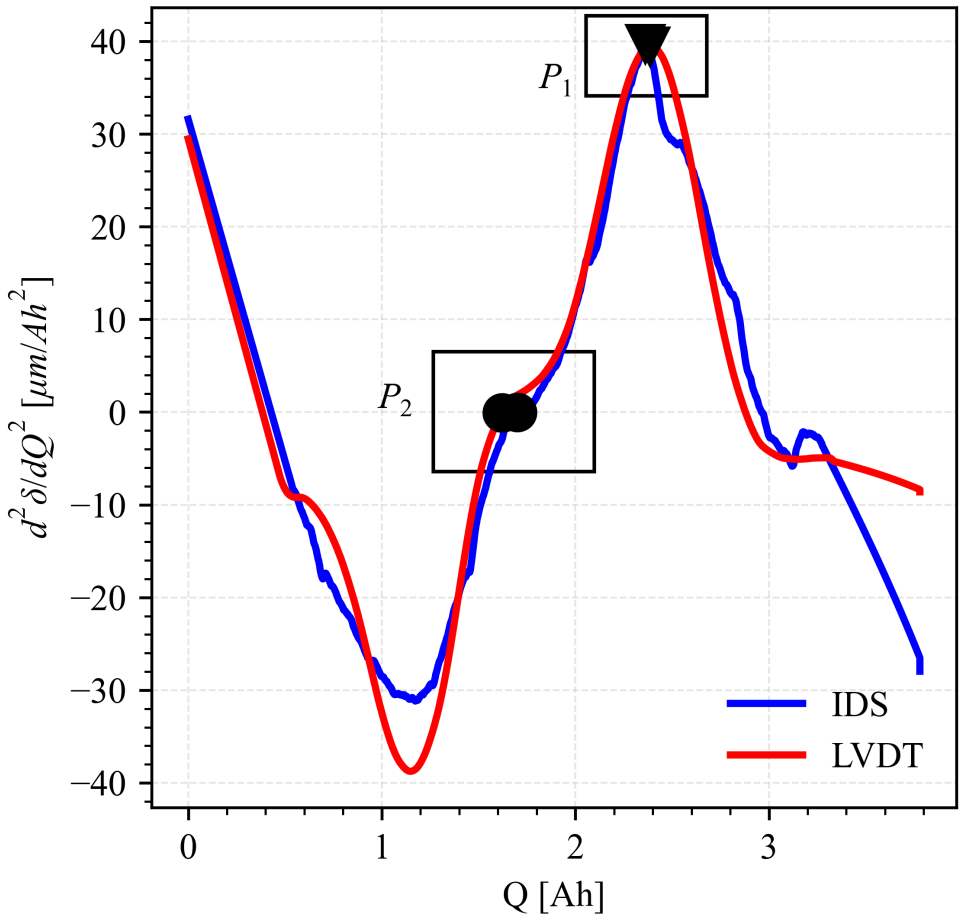


Figure 2.6: Differential expansion signal and battery SOH features locations P_1 and P_2 for both sensors for a C/3 charge. While location of P_1 is almost identical for both sensors, there was a 2% SOC error in the location of the P_2 feature.

linearly proportional to displacement at multiple temperatures with coefficient of determination $r^2 > 0.999$. The uncertainty in measurement is $0.26\,\mu m$ at room temperature and has a higher value of $0.\,\mu m$ at 45°C. When comparing the performance of IDS sensor with the LVDT sensor during battery cycling, we observe that the maximum error in measurement is $3.2\,\mu m$ and the RMSE is $0.7\,\mu m$. The sensor meets our target accuracy requirements and will enable high throughput testing of battery expansion at a low cost.

CHAPTER 3

Battery Electrochemical and Expansion Models

3.1 Introduction

A physics-based degradation modeling approach is used in this thesis to predict battery degradation. This electrochemical model describes the transport and chemical reactions occurring inside the battery and thus captures the internal states of a battery. Constraints on internal states like negative solid-surface concentration are required to prevent degradation mechanisms like lithium plating during high C-rate charging (C-rate is a measure of the rate at which a battery is discharged relative to its maximum capacity). Full-order electrochemical models like the Doyle-Fuller-Newman (DFN) model can predict these internal states accurately but at the expense of computational effort. Reduced order models, such as the single particle model (SPM), are often used in battery state estimation and control. The SPM assumes a uniform current density across the electrodes and neglects the electrolyte dynamics. In this framework, the electrode can be modeled as a single representative spherical particle. The SPM tracks the solid-phase lithium concentration along the radius of a representative spherical particle and uses it to predict battery terminal voltage.

Due to the time-scale separation between the slow dynamic evolution of degradation, e.g. capacity loss over hundreds of cycles, caused by mechanics and chemical reactions, and the relatively fast changes in concentration arising from current flow into and out of the battery, these processes can be modeled approximately by decoupling them. The degradation states are referred to as intra-cycle states in this thesis and can be assumed constant over a single charge-discharge cycle as in the model presented in this chapter.

The main goal of this thesis is to model battery expansion as the battery ages. Battery expansion has two components, first of which is reversible expansion. The cause of reversible expansion is volumetric changes in both electrodes of a Li-ion battery due to lithium intercalation and de-intercalation. The volumetric change depends on the concentration distribution

of lithium across the electrodes, which are the intra-cycle states. The other component is irreversible expansion, caused by degradation mechanisms rather than lithium intercalation. The degradation states change on a slower timescale and are called inter-cycle states.

In this chapter, we first introduce the SPM in Section 3.2. Afterward, in Section 3.3, we link the lithium concentration states in SPM to battery reversible expansion. The expansion model also estimates intercalation-induced particle stress in the electrode particles. Mechanical damage of the electrodes due to particle stress is an important degradation mechanism and will be introduced along with irreversible expansion in Chapter 4. The models discussed in this chapter are used to develop a lithiation state observer in Appendix B.

3.2 Electrochemical Model: Single Particle Model

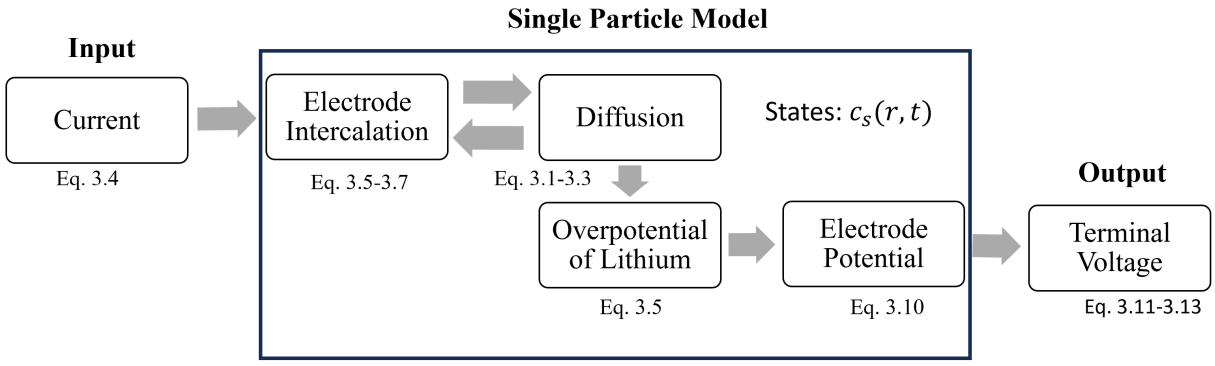


Figure 3.1: Overview of the Single Particle Model (SPM). The input to the model is applied current and the output is terminal voltage. The SPM keeps track of states of lithiation in the negative and positive electrodes and uses these states to predict the voltage.

The SPM is a commonly used control-oriented electrochemical model for the lithium ion battery. It approximates the full order Doyle-Fuller-Newman (DFN) model under low current operation, where the electrode intercalation reaction is uniform across the electrode thickness and decoupled from changes in electrolyte concentration. In this case, the voltage dynamics are dominated by the solid-phase diffusion of lithium. This solid phase diffusion is modeled by using electrodes with a single representative spherical particle. Solid phase diffusion of the spherical particle is solved via discretization methods [53] or Padé approximation [54] to find the states of lithiation across the particle. Eqs. (3.1) to (3.3) show the diffusion equation for a spherical particle along with the requisite boundary conditions at the center and the

surface of the particle.

$$\frac{\partial c_s}{\partial t}(r,t) = \frac{1}{r^2}\frac{1}{\partial r}\left[D_s r^2 \frac{\partial c_s}{\partial r}(r,t)\right] \tag{3.1}$$

$$\frac{\partial c_s}{\partial r}(0,t) = 0 \tag{3.2}$$

$$D_s \frac{\partial c_s}{\partial r}(R_p,t) = \frac{-j_{\text{int}}}{F} = \frac{-(j_{\text{tot}} - j_{\text{SEI}} - j_{\text{pl}})}{F} \qquad \left[\frac{\text{mol}}{\text{m}^2\text{s}}\right] \tag{3.3}$$

$$j_{\text{tot}} = \frac{I}{a_s l A} \qquad \left[\frac{\text{A}}{\text{m}^2}\right] \tag{3.4}$$

Here, $c_s(r)$ represents the state of lithiation across the particle radius, otherwise known as concentration of lithium in the solid particle. These states are referred to as intra-cycle states in this thesis. Also, A is the area, l is the thickness of the electrode, and $a_s = 3\varepsilon_s/R_p$ is the surface area to volume ratio of active material particles that are used to calculate j_{tot} the total current density Eq. (3.4). The intercalation current density j_{int} imposed at the particle surface "drives" the boundary conditions of the lithium concentration through the diffusion equation. j_{SEI} and j_{pl} are side reaction current densities which will be introduced in Chapter 4. In this chapter, we don't consider degradation. Hence, $j_{\text{SEI}} = j_{\text{pl}} = 0$ and $j_{\text{int}} = j_{\text{tot}}$.

We then use the Bulter-Volmer equation Eq. (3.5) to solve for the overpotential of the intercalation reaction η, where i_0 is the exchange current density Eqs. (3.6) and (3.7), $c_{ss}(t) = c_s(R_p,t)$ is the concentration at the surface of the particle, c_e is concentration of lithium in the electrolyte, the k_0 is the reaction rate constant, and the α is the charge transfer coefficient.

$$\eta = \frac{RT}{(1-\alpha)F}\,\text{sinh}^{-1}\left(\frac{j_{\text{int}}}{2i_0F}\right) \tag{3.5}$$

$$i_0^- = k_0\left(\bar{c_e}^-\right)^{(1-\alpha)}\left(c_{s,max}^- \times 1.2 - c_{ss}^-\right)^{(1-\alpha)}\left(c_{ss}^-\right)^{\alpha} \tag{3.6}$$

$$i_0^+ = k_0\left(\bar{c_e}^+\right)^{(1-\alpha)}\left(c_{s,max}^+ - c_{ss}^+\right)^{(1-\alpha)}\left(c_{ss}^+ + 20000\right)^{\alpha} \tag{3.7}$$

We use a non-standard exchange current density Eqs. (3.6) and (3.7) in this work and the reason of it is discussed in Section 5.4.4. The initial concentrations of the electrodes are given by

$$c_{s,0}^+ = c_{s,max}^+(SOC_0 \times (y_{100} - y_0) + y_0) \tag{3.8}$$

$$c_{s,0}^- = c_{s,max}^-(SOC_0 \times (x_{100} - x_0) + x_0) \tag{3.9}$$

where SOC_0 is the initial state of charge, $c_{s,max}$ is the maximum particle concentration,

y_{100}, y_0 are the positive electrode stoichiometric windows and x_{100}, x_0 are the negative electrode stoichiometric windows defined by the voltage limits and electrode physical dimensions [55].

Finally the terminal voltage of the battery is given by Eq. (3.13) where U is the half-cell open circuit potential, and V_R is the voltage drop due to the film resistance.

$$\phi_{\mathrm{s}} = \eta + V_{\mathrm{R}} + U(c_{\mathrm{ss}}) \tag{3.10}$$

$$V_{\mathrm{R}}^{+} = 0 \tag{3.11}$$

$$V_{\mathrm{R}}^{-} = j_{\mathrm{tot}} R_{\mathrm{film}} \tag{3.12}$$

$$V_t = \phi_{\mathrm{s}}^{+} - \phi_{\mathrm{s}}^{-} \tag{3.13}$$

3.3 Battery Expansion Model: Particle to Cell

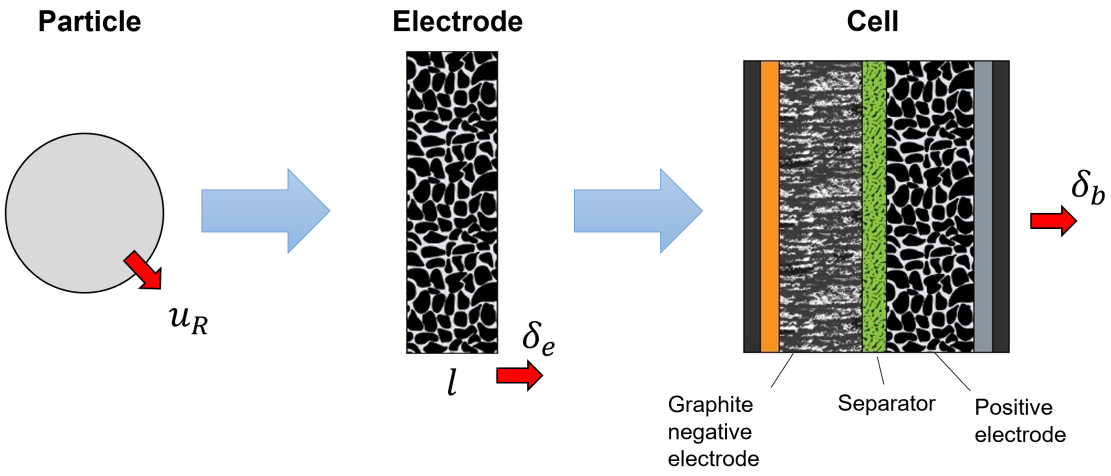


Figure 3.2: Illustration of the Battery reversible expansion model. Lithium intercalation leads to particle stress and strain. Particle strain results in electrode expansion. Battery expansion is the sum of the expansion of negative and positive electrodes.

In this section, we will link the states in the SPM to the observed battery expansion. This is done by first using particle stress and strain model to link particle concentration to particle displacement and stress. Particle stress will be used in the next chapter as a part of the mechanical degradation model. Then, we link the particle displacement to electrode expansion and cell expansion. The battery reversible expansion is illustrated in Fig. 3.2.

3.3.1 Particle Stress and Strain Model

In this section, we derive the relationship between particle expansion and particle stress. The intercalation-induced particle stress model from [56] was used. We first start with the equations for stress-strain relationship:

$$\epsilon_r = \frac{1}{E}[\sigma_r - 2\nu\sigma_t] + \frac{\Delta\mathcal{V}(c_s(r))}{3} \tag{3.14}$$

$$\epsilon_t = \frac{1}{E}[(1-\nu)\sigma_t - \nu\sigma_r] + \frac{\Delta\mathcal{V}(c_s(r))}{3} \tag{3.15}$$

Where ϵ_r and ϵ_t are the particle strains in radial and tangential directions respectively. Stresses are represented by σ_r and σ_t. E is the Young's Modulus, ν is the Poisson's ratio and $\Delta\mathcal{V}(c_s(r))$ is the particle expansion function in terms of volumetric strain expansion identified in [33] based on first principles model in [34]. $c_s(r)$ is the concentration distribution inside the particle. We can solve Eqs. (3.14) and (3.15) to get the equations for the radial (σ_r) and tangential (σ_t) stresses:

$$\sigma_r = \frac{E}{(1+\nu)(1-2\nu)}[(1-\nu)\epsilon_r + 2\nu\epsilon_t] - \frac{E\Delta\mathcal{V}(c_s(r))}{3(1-2\nu)} \tag{3.16}$$

$$\sigma_t = \frac{E}{(1+\nu)(1-2\nu)}[\epsilon_t + \nu\epsilon_r] - \frac{E\Delta\mathcal{V}(c_s(r))}{3(1-2\nu)} \tag{3.17}$$

Next, the Stress equilibrium in the radial direction is given by:

$$\frac{d\sigma_r}{dt} + \frac{2(\sigma_r - \sigma_t)}{r} = 0 \tag{3.18}$$

Strain-displacement relationship is given by:

$$\epsilon_r = \frac{du}{dr} \tag{3.19}$$

$$\epsilon_t = \frac{u}{r} \tag{3.20}$$

Then, we use Equations (3.14) to (3.20) to generate the Displacement equation:

$$\frac{d^2u}{dr^2} + \frac{2}{r}\frac{du}{dr} - \frac{2u}{r} = \frac{1+\nu}{1-\nu}\frac{d}{dr}\left(\frac{\Delta\mathcal{V}(c_s(r))}{3}\right) \tag{3.21}$$

with the boundary conditions:

$$u(0,t) = 0 \tag{3.22}$$

$$\sigma_r(R_p,t) = 0 \tag{3.23}$$

Eq. (3.21) reduces to:

$$\frac{d}{dr}\left(\frac{1}{r^2}\frac{d}{dr}\left(r^2u\right)\right) = \frac{1+\nu}{1-\nu}\frac{d}{dr}\left(\frac{\Delta\mathcal{V}(c_s(r))}{3}\right) \tag{3.24}$$

Integrating twice we get:

$$u(r) = \frac{1+\nu}{1-\nu}\frac{1}{3}\frac{1}{r^2}\left(\int_0^r \rho^2\Delta\mathcal{V}(c_s(\rho,t))d\rho\right) + Ar + \frac{B}{r^2} \tag{3.25}$$

Integrating the Displacement equation using the boundary conditions gives us a solution for the displacement u. Based on Eq. (3.22) the integration constant $B = 0$. A is found using Eq. (3.23) and is given by

$$A = \frac{1-2\nu}{1-\nu}\frac{2}{3R_p^3}\int_0^{R_p} \rho^2\Delta\mathcal{V}(c_s(\rho,t))d\rho \tag{3.26}$$

Finally the displacement is given by

$$u(r) = \frac{1+\nu}{1-\nu}\frac{1}{3r^2}\left(\int_0^r \rho^2\Delta\mathcal{V}(c_s(\rho,t))d\rho\right) + \frac{1-2\nu}{1-\nu}\frac{2r}{3R_p^3}\left(\int_0^{R_p} \rho^2\Delta\mathcal{V}(c_s(\rho,t))d\rho\right) \tag{3.27}$$

We substitute this solution back in Eqs. (3.14) and (3.15) to get the stresses. The radial stress and tangential stress are given by:

$$\sigma_r(r,t) = \frac{2E}{3(1-\nu)}\left(\frac{1}{R_p^3}\int_0^{R_p} \rho^2\Delta\mathcal{V}(c_s(\rho,t))d\rho - \frac{1}{r^3}\int_0^r \rho^2\Delta\mathcal{V}(c_s(\rho,t))d\rho\right) \tag{3.28}$$

$$\sigma_t(r,t) = \frac{E}{3(1-\nu)}\left(\frac{2}{R_p^3}\int_0^{R_p} \rho^2\Delta\mathcal{V}(c_s(\rho,t))d\rho + \frac{1}{r^3}\int_0^r \rho^2\Delta\mathcal{V}(c_s(\rho,t))d\rho - \Delta\mathcal{V}(c_s(r,t))\right) \tag{3.29}$$

We use Hydrostatic stress σ_h in our mechanical damage model (Section 4.4), which is given

by:

$$\sigma_h(r,t) = \frac{\sigma_r(r,t) + 2\sigma_t(r,t)}{3} \tag{3.30}$$

$$\sigma_h(r,t) = \frac{2E}{3(1-\nu)}\left(\frac{1}{R_p^3}\int_0^{R_p}\rho^2\Delta\mathcal{V}(c_s(\rho,t))d\rho - \frac{\Delta\mathcal{V}(c_s(r,t))}{3}\right) \tag{3.31}$$

The assumptions made in this model are:

1. We are modeling only intercalation induced stress
2. Intercalation induced stress is considered to be linear function of the concentration and the partial molar volume instead of using a piece linear function of the graphite stoichiometry
3. The diffusion in the particle is assumed unaffected by the stress gradient in the particle, i.e., we are not modeling stress-induced diffusion.
4. We are not modeling the stress across the SEI layer and assume that the entire particle is made of a single material (graphite).

3.3.2 Particle Expansion

The displacement at the surface of the particle is found by setting $r = R_p$ in Eq. (3.27), giving us:

$$u_R(t) = \frac{1}{(R_p)^2}\int_0^{R_p}\rho^2\Delta\mathcal{V}\left(c_s(\rho,t)\right)d\rho \tag{3.32}$$

This displacement at the particle surface is the value of particle expansion we use to calculate the battery expansion.

3.3.3 Electrode Expansion due to Intercalation

The electrode in a Li-battery is made of active material, binder and conductive material. In our model, we assume that the expansion of electrode components other than the active material during charging-discharging is negligible. This is valid under constant pressure operation and pseudo steady state, which results in constant porosity of the electrodes [57, 58].

Next, we define some of the dimensional (length, area and volume) conversions in the SPM. The specific interfacial area of the electrode with particle radius R_p and solid-phase

volume fraction ε_{s} (referred to as active material ratio in this work) is given by [59] as:

$$\begin{aligned} a_s &= \frac{\text{total surface area}}{\text{total volume}} \\ &= \underbrace{\frac{\text{volume of solid}}{\text{total volume}}}_{\varepsilon_{\mathrm{s}}} \frac{\text{total surface area/particle}}{\text{volume of solid/particle}} \\ &= \varepsilon_{\mathrm{s}} \frac{4\pi R_{\mathrm{p}}^2}{\frac{4}{4}\pi R_{\mathrm{p}}^3} = \frac{3\varepsilon_{\mathrm{s}}}{R_{\mathrm{p}}}. \end{aligned} \tag{3.33}$$

Let us define the thickness change of the electrode due to electrode intercalation as:

$$\delta_{\mathrm{e}} = \Delta l. \tag{3.34}$$

We further assume that the electrode only expands in the through-plane direction [60, 33]. So, the volume change of electrode due to intercalation is:

$$\Delta V_{\mathrm{e}} = A\delta_{\mathrm{e}}, \tag{3.35}$$

where A is the electrode cross-sectional area. We can also calculate the volume change of electrode due to intercalation by using the displacement at the surface of the particle u_R shown in Eq. (3.32), and the electrode active surface area $\varepsilon_{\mathrm{s}} 4\pi R_{\mathrm{p}}^2$:

$$\Delta V_{\mathrm{e}} = \varepsilon_{\mathrm{s}} \left(4\pi R_{\mathrm{p}}^2\right) u_R. \tag{3.36}$$

Combining Eqs. (3.33), (3.35) and (3.36), gives us the following equation for the change in electrode thickness.

$$\delta_{\mathrm{e}} = a_s l u_R \tag{3.37}$$

3.3.4 Total Expansion

The total electrode expansion is the sum of the expansion of individual electrodes. Pouch cell Li-ion batteries contain multiple layers, So the single layer expansion is multiplied by the number of layers to find the total expansion. Also the cell level expansion is influenced by separator, current collectors and casing. The elasticity of these layers are approximated with a linear spring. The total battery expansion is the sum of the expansion of negative

and positive and is given by: Eq. (3.38)

$$\delta_b = \kappa_b(\delta_e^+ + \delta_e^-) \tag{3.38}$$

where κ_b is a tunable parameter that depends on the number of electrode layers and the battery stiffness. δ_e^+ is expansion of positive electrode and δ_e^- is expansion of negative electrode. Further details on calculating κ_b can be found in [33].

3.4 Conclusion

This chapter describes the SPM modeling framework used in this thesis. SPM is used to predict the faster timescale intra-cycle lithiation states of the degradation model and the battery voltage. Then, a model for reversible battery expansion based on SPM is described. Reversible expansion is caused by lithium intercalation and is linked to the lithium concentration states of SPM. The concentration distribution of lithium in electrode particles leads to the development of particle stress and strain. The particle strain causes battery expansion, and particle stress causes battery degradation.

CHAPTER 4

Degradation Model Mechanisms

4.1 Introduction

Physics-based degradation models use additional systems of partial differential equations coupled with electrochemical models to describe the changes in the battery's electrical and mechanical response as the battery ages. The states of these degradation models evolve on a slower timescale compared to lithiation states of the electro-chemical models and are referred to as inter-cycle states in this thesis. We model only the dominant degradation mechanisms int this work, which are: Solid Electrolyte Interface (SEI) growth [13, 14, 15], lithium plating [16, 17], and particle cracking of the anode and cathode materials [18, 19].

We describe the modeling approach for each of the battery degradation mechanisms and their impact on changes in battery performance metrics: capacity, resistance, and reversible and irreversible expansion. We introduce asymmetric equivalent stress to the mechanical damage model, which allows us to capture degradation in cells cycled at different currents for charge and discharge. The concentration dependence of particle stress in the negative electrode was considered in the mechanical damage mechanism, helping us capture the DOD dependence on degradation. We also introduced a current-dependent dynamic term in the lithium plating model mechanism to account for spatial non-uniformity of electrolyte dynamics that SPM doesn't capture at higher C-rates. The inter-cycle degradation mechanisms are implemented within an intra-cycle SPM and solved using PyBaMM [61]. The governing equations for SPM are given in Section 3.2.

This chapter is organized as follows. First, the degradation mechanisms of SEI growth, Lithium plating and Mechanical damage are introduced in chapters Section 4.2, Section 4.3 and Section 4.4 respectively. Then, we link the degradation mechanisms to resistance growth and battery expansion in Section 4.5. Afterwards in Section 4.6, we discuss how the different degradation mechanisms interact with each other.

4.2 SEI Growth

The most commonly modeled aging mechanism is SEI formation and growth. The first SEI layer forms on the surface of the negative electrode (graphite for this study) during the formation process of the cell [20], from the reaction of lithium-ions with the electrolyte. This SEI layer initially protects the electrode against further reactions with the electrolyte but over time leads to loss of cyclable lithium, leading to capacity fade and also an increase in battery resistance. The growth of the SEI layer also causes an increase in battery thickness [2]. Researchers have proposed various models for the SEI growth, including kinetically limited SEI growth [13], solvent diffusion limited [14, 16] and electron migration limited [15]. The SEI model used in our work is adopted from [16]. The equation for current density involved in the SEI formation j_{SEI} is given by

$$j_{\text{SEI}} = -k_{\text{SEI}} F c_{EC}^{s} exp\left(\frac{-\alpha_{\text{SEI}} F}{RT}\eta_{\text{SEI}}\right) \tag{4.1}$$

$$-D_{\text{SEI}}\frac{c_{EC}^{s} - c_{EC}^{0}}{\delta_{\text{SEI}}} = -\frac{j_{\text{SEI}}}{F} \tag{4.2}$$

where k_{SEI} is the kinetic rate constant, c_{EC}^{0} is the concentration of Ethylene Carbonate (EC) in the bulk electrolyte, which is assumed to be constant in our model, c_{EC}^{s} is the concentration of EC at the graphite surface, calculated by Eq. (4.2), D_{SEI} is the diffusivity of SEI layer, δ_{SEI} is the SEI layer thickness, α_{SEI} is the SEI charge transfer coefficient and η_{SEI} is the overpotential of SEI growth given by:

$$\eta_{\text{SEI}} = \eta^{-} + U^{-}\left(c_{\text{ss}}^{-}\right) - U_{\text{SEI}} \tag{4.3}$$

where η^{-} is negative electrode overpotential, $U^{-}\left(c_{\text{ss}}^{-}\right)$ is the surface concentration dependent negative electrode open circuit potential (OCP), U_{SEI} is the potential of SEI reaction. Eqs. (4.1) and (4.2) are solved together for j_{SEI}, showing the kinetic and diffusion limited mechanism that governs the SEI growth:

$$j_{\text{SEI}} = \frac{-c_{EC}^{0} F}{1/(k_{\text{SEI}} \exp\left(\frac{-\alpha_{\text{SEI}} F}{RT}\eta_{\text{SEI}}\right)) + \delta_{\text{SEI}}/(D_{\text{SEI}})}. \tag{4.4}$$

The material build up of SEI is given by:

$$\frac{\partial c_{\text{SEI}}}{\partial t} = -\frac{a_{s}^{-} j_{\text{SEI}}}{2F} \tag{4.5}$$

where, c_{SEI} is concentration of formed SEI, a_s^- is the specific surface area of active material in the negative electrode given by:

$$a_s = \frac{3\varepsilon_{\text{s}}}{R_{\text{p}}} \tag{4.6}$$

where R_{p} is electrode particle radius and ε_{s} is the volume fraction of active material. The active material volume fraction is a dynamic state in the model given by Eq. (4.30) and decreases due to mechanical damage as discussed in Section 4.4. Eq. (4.5) assumes that the SEI is formed only on the active surface area and not on the mechanically damaged electrode surface. Using the molar concentrations of Li and SEI per unit volume of the electrode calculated by the integral of Eq. (4.5) we compute the thickness of the SEI film δ_{SEI}:

$$\delta_{\text{SEI}} = \frac{1}{a_{s,0}^-} \left(c_{\text{SEI}} \Omega_{\text{SEI}}\right) \tag{4.7}$$

where $a_{s,0}^-$ is the initial (fresh cell) active surface area to volume ratio of the negative electrode and the product of $c_{\text{SEI}}\Omega_{\text{SEI}}$ gives us the volume fraction of SEI layer in the negative electrode. The volume fraction is converted to thickness by multiplying with the inverse of the surface area to volume ratio since the SEI layer is formed on the surface of the particle. The active material volume fraction a_s^- in our model decreases due to aging and cannot be used for scaling from volume to thickness because it will give us a higher estimate of SEI thickness. Hence we use the fresh cell active surface area to volume ratio $a_{s,0}^-$ for scaling.

There are several effects of SEI growth on battery performance. SEI growth leads to lithium loss $n_{\text{Li,SEI}}$ thus reducing cell capacity. SEI growth also leads to a resistance increase $R_{\text{film,SEI}}$, affecting battery terminal voltage as shown in Eq. (4.45) and Eq. (3.12). This resistance increase is primarily due to the increase in transport losses due to an increase in transport length from the bulk electrolyte to the surface of the active material through the thickening SEI layer. Finally, an increase in the thickness of the SEI layer goes towards both porosity changes affecting the cell resistance shown in Eq. (4.8) and electrode irreversible thickness growth of the battery as shown in Eq. (4.9). The parameters to be tuned in the SEI growth model are: $k_{0,\text{SEI}}$, D_{SEI} and $E_{a,SEI}$. The method and process for tuning these

parameters is shown in Section 5.2.5.

$$R_{\text{film,SEI}} = \frac{\delta_{\text{SEI}}}{\kappa_{\text{SEI}}} \tag{4.8}$$

$$\delta_{\text{irrev,SEI}} = b_{\text{SEI}}\delta_{\text{SEI}} \tag{4.9}$$

$$\dot{n}_{\text{Li,SEI}} = -Al^{-}a_s^{-}j_{\text{SEI}} \tag{4.10}$$

where κ_{SEI} is conductivity of SEI layer, b_{SEI} is scaling factor for irreversible expansion, A is the area, l^{-} is the thickness of the anode. The tuning process for a consistent model of Eqs. (4.8) to (4.10) are discussed further in Section 4.5.

4.3 Lithium Plating

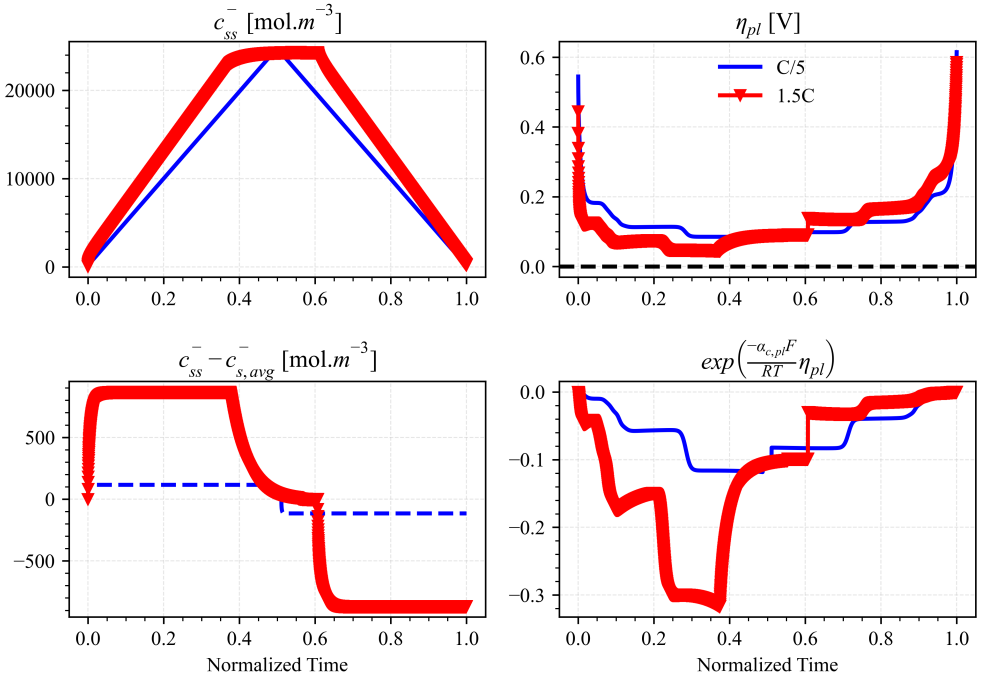


Figure 4.1: Comparison of variables used in Li plating model at C/5 (blue), 1.5C (red). The variables compared are: c_{ss}^{-}, which influences the concentration gradient $c_{\text{ss}}^{-} - c_{\text{s,avg}}^{-}$ which in turn influences η_{pl}. We also compare exp $\left(\frac{-\alpha_{c,pl}F}{RT}\eta_{pl}\right)$ which directly influences the plating current j_{pl} for two C-rates

Lithium plating occurs when lithium-ions deposit as metallic lithium on the surface of the particle instead of intercalating into the particle under conditions when metallic lithium formation is more thermodynamically favorable than the intercalation reaction. This leads

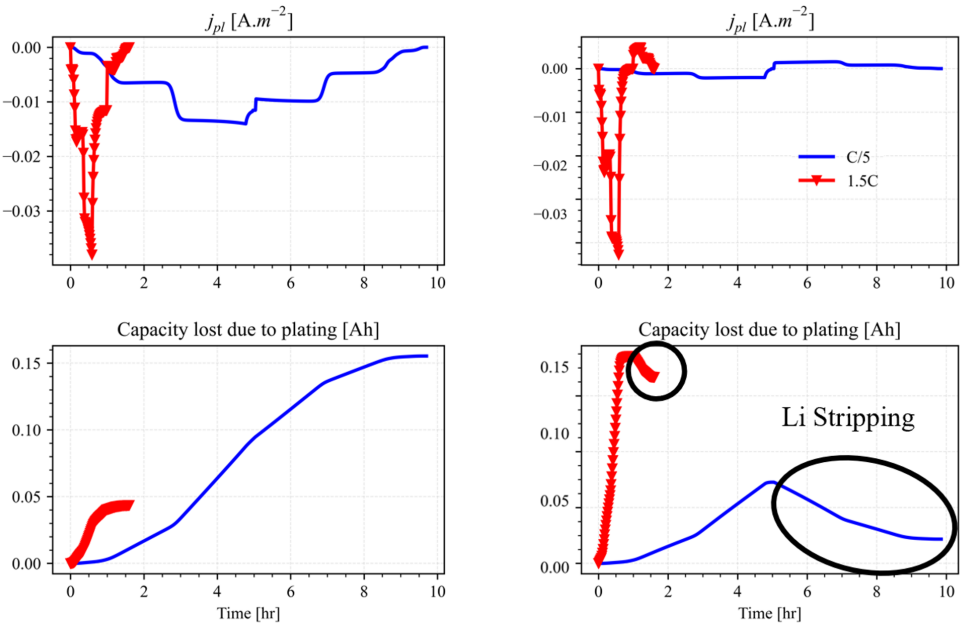


Figure 4.2: Plating model comparison. a) shows the plating current and capacity loss for the conventional $i_{0,pl}$ formulation while b) shows the same for the new $i_{0,pl}$ formulation. The conventional $i_{0,pl}$ has higher capacity loss due to Li plating at C/5, the modified $i_{0,pl}$ shows higher capacity loss at 1.5C. This is because the modified $i_{0,pl}$ increases the gradient in magnitude of j_{pl} for the two C-rates while also adding the effect of Li stripping during discharge.

to loss of cyclable lithium, capacity fade, increase in cell thickness [21] and could potentially result in thermal events at the cell level due to internal shorts caused by dendrite formation. Lithium plating is commonly modeled using either Tafel or Bulter-Volmer kinetics [16, 22, 17]. The lithium plating model is adopted from [16, 62] and uses Tafel kinetics for the plating current density j_{pl} :

$$j_{pl} = -i_{0,pl} \exp\left(\frac{-\alpha_{c,pl} F}{RT} \eta_{pl}\right) \tag{4.11}$$

$$i_{0,pl} = k_{0,pl} c_e k_{\mathrm{dy}}(I) F \tag{4.12}$$

$$\frac{\partial c_{\mathrm{pl}}}{\partial t} = \frac{a_s^- j_{\mathrm{pl}}}{F} \tag{4.13}$$

where $i_{0,pl}$ is the exchange current density of Li deposition, c_{pl} is concentration of accumulated plating, $\alpha_{c,pl}$ is charge transfer coefficient, $k_{0,pl}$ is the Li plating kinetic rate constant, c_e is

concentration of Li in electrolyte. The overpotential of Li plating η_{pl} is given by:

(4.14)

$$\eta_{\mathrm{pl}} = \eta^{-} + U^{-}\left(c_{\mathrm{ss}}^{-}\right). \tag{4.15}$$

We use a new approach in re-formulating the original $i_{0,pl} = k_{0,pl} c_e F$ in our model Eq. (4.12), by including the term $k_{\mathrm{dy}}(I)$, which is a dynamic lumped modification introduced to capture spatial non-uniformity in electrolyte dynamics. This modification is needed to overcome the well-known limitation of the SPM for predicting lithium plating due to the assumption of uniform intercalation current across the electrode. Specifically, Fig. 4.2 shows that the plating overpotential remains above zero for the duration of the charge, and hence the SPM would not predict significant plating at either C/5 or 1.5C at any temperature. The non-uniformity of the intercalation current predicted by the P2D model can better explain the localized plating at the separator interface due to the increased local lithium concentration in the anode. Here we add the $k_{\mathrm{dy}}(I)$ term to capture C-rate dependent plating, which builds over time due to the evolution of a solid phase surface concentration gradient across the electrode. The dynamic term $k_{\mathrm{dy}}(I)$ that we propose is a function of C-rate to capture the higher amount of plating occurring during the smaller interval corresponding to high C-rate but with filtered time response that is approximated using first-order dynamics (τ_{dy}):

(4.16)

$$\frac{dk_{\mathrm{dy}}}{dt} = \frac{1}{\tau_{\mathrm{dy}}}\left(-k_{\mathrm{dy}} + \frac{I}{I_{1\mathrm{C}}}\right) \tag{4.17}$$

We found that a reasonable time constant for the first-order dynamics of k_{dy} is related to the relaxation of solid phase concentration gradient. Thus we use the value of $k_{\mathrm{dy}} = \frac{c_{\mathrm{ss}}^{-} - c_{\mathrm{avg}}^{-}}{c_{\mathrm{s,max}}^{-}}$ (shown in Fig. 4.1) which represents the concentration gradient as the additional dynamic term in the formulation of $i_{0,pl}$. Here c_{ss}^{-} is surface concentration, c_{avg}^{-} is the average concentration and $c_{\mathrm{s,max}}^{-}$ is the maximum concentration of lithium in graphite. As shown in Fig. 4.1, the η_{pl} curve for 1.5C reaches lower values compared to C/5, thus leading to higher magnitude of the Tafel driven kinetics $\exp\left(\frac{-\alpha_{c,pl} F}{RT}\eta_{pl}\right)$ term in Eq. (4.11) which determines the plating current. The ratio between the maximum magnitudes of this variable at 1.5C and C/5 is 2.67 higher which compensates for the shorter duration (2 hrs for a charge-discharge cycle at 1.5C compared to 10 hours for a charge-discharge cycle at C/5) that the higher value lasts in the high C-rate. Fig. 4.2 clarifies the need of the additional dynamic term k_{dy} in the exchange current density, by demonstrating that the conventional formulation of $i_{0,pl}$ without the dynamic term k_{dy} results to lower capacity loss due to Li plating for

1.5C compared to C/5. The lower capacity loss for 1.5C is because the magnitude of j_{pl} at 1.5C is not significantly higher to compensate for the considerably less time spent at the higher C-rate operation. Using the modified formulation of Eq. (4.12) gives us the increase in gradient in the magnitudes of j_{pl} for different C-rates, compared to the conventional formulation, which results in capacity loss of Li plating at 1.5C being higher than C/5 as seen in Fig. 4.2 b).

The additional dynamic term k_{dy} also introduces the effect of Li stripping during discharge, because the sign of the term is negative. This causes a positive j_{pl} during discharge leading to recovery of lost capacity. Even though the rate of recovery is higher at 1.5C compared to C/5, the total recovery is higher at C/5. This is because if you integrate j_{pl} over the time spent stripping, the cumulative stripped lithium is higher at C/5 as shown in Fig. 4.2 b). Higher recovery of lost capacity also makes the capacity loss of Li plating at 1.5C much higher compared to C/5.

Finally, the thickness of the plated lithium is modeled similarly to the SEI:

$$\delta_{\text{pl}} = \frac{1}{a_{s,0}^{-}} \left(c_{\text{pl}} \Omega_{\text{pl}}\right) \tag{4.18}$$

where Ω_{pl} is Li partial molar volume.

The effects of lithium plating on battery aging performance metrics are similar to the effect of SEI growth. These include lithium loss $n_{\text{Li,pl}}$ Eq. (4.19), resistance increase $R_{\text{film,pl}}$ Eq. (4.20), and battery expansion $\delta_{\text{irrev,pl}}$ Eq. (4.21). The parameters we tune in the Li plating model are $k_L i$, conductivity of plated Li layer κ_{pl}, and scaling factor for irreversible expansion b_{pl}.

$$\dot{n}_{\text{Li,pl}} = -A l^{-} a_s^{-} j_{\text{pl}} \tag{4.19}$$

$$R_{\text{film,pl}} = \frac{\delta_{\text{pl}}}{\kappa_{\text{pl}}} \tag{4.20}$$

$$\delta_{\text{irrev,pl}} = b_{\text{pl}} \delta_{\text{pl}}^2 \tag{4.21}$$

The method for tuning these parameters is discussed in Section 5.2.6.

4.4 Mechanical Damage

The electrodes of a lithium-ion battery expand during intercalation of lithium-ions and contract during de-intercalation. When the batteries are cycled, this expansion and contraction leads to cycling stresses in the electrodes leading to fatigue damage of the electrode materials

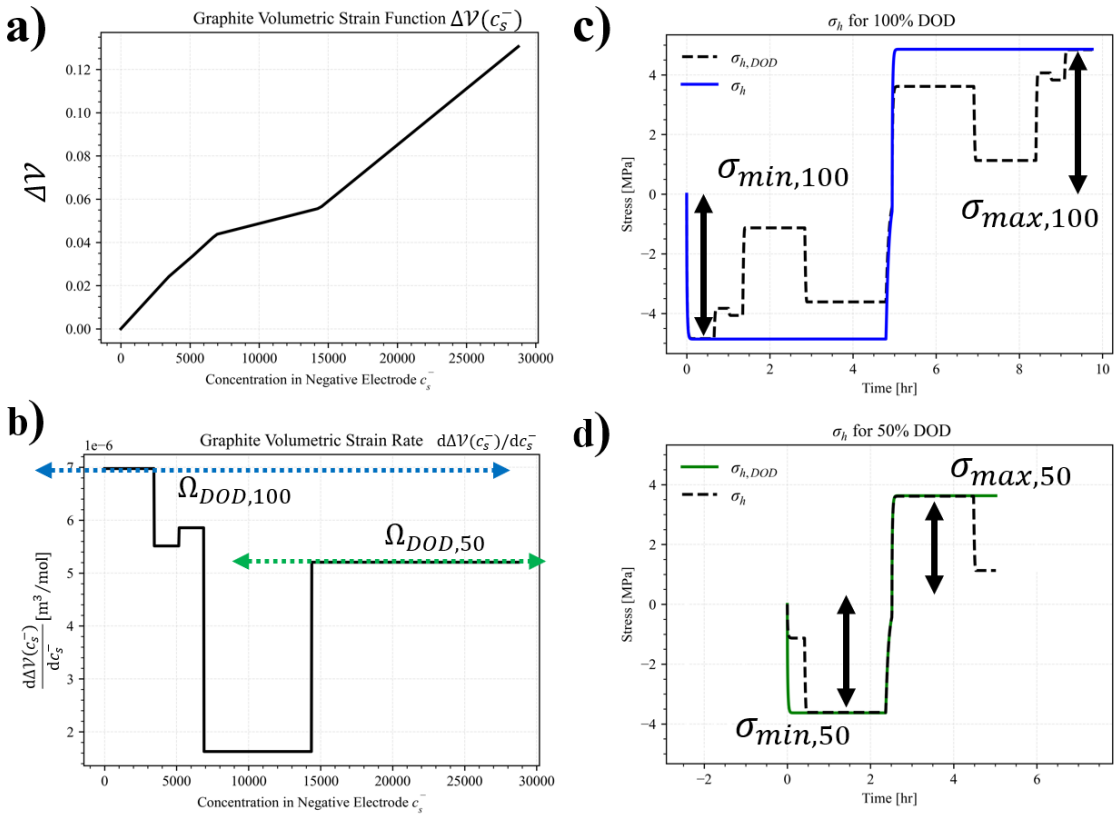


Figure 4.3: a) Volumetric strain of the negative electrode as a piecewise linear function of particle stoichiometry (concentration). b) Volumetric strain rate of the negative electrode. Strain rates for 100% DOD ($\Omega_{\text{DOD},100}$) and 50% DOD ($\Omega_{\text{DOD},50}$) estimated using Eq. 4.35. c) Values of σ_h at C/5 100% DOD estimated using concentration dependent stress Eq. 4.31 (black) and simplified stress Eq. 4.36 (blue). d) Values of σ_h at C/5 50% DOD estimated using concentration dependent stress Eq. 4.31 (black) and simplified stress Eq. 4.36 (green). The strain rate in the negative electrode is concentration dependent which results in different magnitudes of minimum and maximum stress at different DOD and thus different rate of capacity loss

and leads to particle cracking of the electrode active materials. This particle cracking causes loss of active material and leads to capacity loss [18, 27, 12]. Researchers have also considered mechanical damage of the SEI layer to be the cause of capacity loss [19, 63], which is not considered in this paper.

The probabilistic S-N curve (Wohler curve) has been used to predict material fracture under cyclic loading in [18] and stresses in a particle during cycling were related to capacity loss in the battery. This correlation can be extended to loss of individual electrode capacity referred to as loss of active material (LAM) due to stresses in the electrode particle [12, 3,

64, 65]. The individual electrode capacity $C_{\mathrm{p,n}}$ is given by:

$$C_{\mathrm{p,n}} = \frac{\varepsilon_{\mathrm{s}}^{\pm} A l^{\pm} c_{\mathrm{s,max}}^{\pm} F}{3600} \tag{4.22}$$

where, A is area of electrode, l is thickness of electrode and ε_s is the active material volume fraction which changes $\Delta\varepsilon_{\mathrm{s}}$ every cycle ΔN proportional to the stress at the surface of the particle as follows:

$$\frac{\Delta\varepsilon_{\mathrm{s}}}{\Delta N} \propto -\left(\frac{\sigma_{\mathrm{a}}}{\sigma_{\mathrm{critical}}}\right)^{m_{\mathrm{LAM}}} \tag{4.23}$$

$$\frac{\Delta\varepsilon_{\mathrm{s}}}{\Delta N} \propto -\left(\frac{\sigma_{\mathrm{max}} - \sigma_{\mathrm{min}}}{\sigma_{\mathrm{critical}}}\right)^{m_{\mathrm{LAM}}} \tag{4.24}$$

where m_{LAM} comes from Basquin power law and is treated as a tuning parameter in our model, $\sigma_{\mathrm{critical}}$ is critical stress and σ_{a} is the stress amplitude at the particle surface given by:

$$\sigma_{\mathrm{a}} = \frac{\sigma_{\mathrm{max}} - \sigma_{\mathrm{min}}}{2} \tag{4.25}$$

where σ_{min} is the minimum stress and σ_{max} is the maximum stress. Eq. (4.23) takes only the amplitude of the cyclic stress into consideration and is valid only for symmetric cycling. When there is asymmetric cycling i.e when the charge and discharge rates are different, the resultant mean stress σ_{m} can affect the fatigue life [66]

$$\sigma_{\mathrm{m}} = \frac{\sigma_{\mathrm{max}} + \sigma_{\mathrm{min}}}{2}. \tag{4.26}$$

To include the effect of mean stress, we can define the equivalent fully reversed normal stress amplitude σ_{ar}. This value according to [67] can be calculated as:

$$\sigma_{\mathrm{ar}} = \sigma_{\mathrm{a}} + M_{\sigma} \times \sigma_{\mathrm{m}} \tag{4.27}$$

where M_{σ} is mean-stress sensitivity factor. Substituting the equivalent stress σ_{ar} in Eq. (4.23), we have:

$$\frac{\Delta\varepsilon_{\mathrm{s}}}{\Delta N} \propto -\left(\frac{(1+M_{\sigma})\sigma_{\mathrm{max}} + (M_{\sigma}-1)\sigma_{\mathrm{min}}}{\sigma_{\mathrm{critical}}}\right)^{m_{\mathrm{LAM}}} \tag{4.28}$$

Using Taylor's series expansion and redefining the coefficients to simplify tuning, we substi-

tute the following approximation for active material loss due to fracture:

$$\frac{\Delta\varepsilon_{\mathrm{s}}}{\Delta N} \approx -\beta'_{\mathrm{LAM},1}\left(\frac{|\sigma_{\max}|}{\sigma_{\mathrm{critical}}}\right)^{m_{\mathrm{LAM}}} - \beta'_{\mathrm{LAM},2}\left(\frac{|\sigma_{\min}|}{\sigma_{\mathrm{critical}}}\right)^{m_{\mathrm{LAM}}} \tag{4.29}$$

We then extend Eq. (4.29), which is the inter-cycle change by assuming the same rate will apply in intracycle, to a continuous time equation as suggested in [12]. Converting the discrete form of the LAM rate to the continuous form also accounts for the effect of depth of discharge on LAM.

$$\frac{d\varepsilon_s}{dt} = -\beta_{\mathrm{LAM},1}\left(\frac{|\sigma_{\max}|}{\sigma_{\mathrm{critical}}}\right)^{m_{\mathrm{LAM}}} - \beta_{\mathrm{LAM},2}\left(\frac{|\sigma_{\min}|}{\sigma_{\mathrm{critical}}}\right)^{m_{\mathrm{LAM}}} \tag{4.30}$$

where the $\beta_{\mathrm{LAM},1}$, $\beta_{\mathrm{LAM},2}$ and m_{LAM} are tuning parameters.

The stresses in the particle are computed in Section 3.3, and shown below:

$$\sigma_h(r,t) = \frac{2E}{3(1-\nu)}\left(\frac{1}{R_p^3}\int_0^{R_p}\rho^2\Delta\mathcal{V}(c_s(\rho,t))d\rho - \frac{\Delta\mathcal{V}(c_s(r,t))}{3}\right) \tag{4.31}$$

$$\sigma_{\min} = \min\left(\sigma_h(R_p,t)\right) \tag{4.32}$$

$$\sigma_{\max} = \max\left(\sigma_h(R_p,t)\right) \tag{4.33}$$

where E is the Young's modulus of the electrode material, $\Delta\mathcal{V}$ is the volumetric strain function of the electrode given in Table 5.3, ν is the poisson's ratio, and R_p is the particle electrode radius.

From the degradation data, we have observed that the rate of LAM in the negative electrode was correlated with DOD. Cells cycled at 100% DOD lost active material in the negative electrode at a faster rate than 50% DOD. The difference in degradation rates can be explained by the concentration dependence of stresses in the negative electrode. While the $\Delta\mathcal{V}$ is linear in the positive electrode, it is piecewise-linear in the negative electrode [33] as shown in Fig. 4.3 a). This means that the negative electrode expands at different rates at different SOCs as shown in Fig. 4.3 b), thus resulting in different stresses at different SOCs as shown in Fig. 4.3 c) and d). The concentration dependence of stress results in different maximum and minimum stresses for different DOD, thus resulting in different degradation rates similar to the experimentally observed degradation rates.

The computation of $\sigma_{\min}$ and $\sigma_{\max}$ can be simplified by using the highest strain rates

corresponding to the DOD:

$$\Delta\mathcal{V}(c_s^-) = \Omega_{\text{DOD}} c_s^- \tag{4.34}$$

$$\Omega_{\text{DOD}} = \max_{\{min(c_s^-(t)) < c_s^- < max(c_s^-(t))\}} \frac{\partial \Delta\mathcal{V}}{\partial c_s^-} \tag{4.35}$$

where Ω_{DOD} is the maximum volumetric strain rate corresponding to the SOC window in which the cell was cycled. For 100% DOD (corresponding to 0-100% SOC window), the strain rate corresponds to the slope of the $\Delta\mathcal{V}$ curve at low electrode stoichiometries (denoted by $\Omega_{\text{DOD},100}$), and for 50% DOD (corresponding to 50-100% SOC window), the strain rate corresponds to slope at high electrode stoichiometries (denoted by $\Omega_{\text{DOD},50}$), which is lower than the strain rate corresponding to lower stoichiometries as shown in Fig. 4.3 b).

$$\sigma_{\text{h,DOD}}(R_p, t) = \frac{2E}{3(1-\nu)} \left(\frac{1}{R_p^3} \int_0^{R_p} \rho^2 \Omega_{\text{DOD}} c_s(\rho, t) d\rho - \frac{\Omega_{\text{DOD}} c_s(R_p, t)}{3} \right) \tag{4.36}$$

Here, the first term on the RHS can be simplified by using the calculation for average particle concentration and the second term corresponds to the surface particle concentration:

$$c_{\text{s,avg}}(t) = \frac{3}{R_p^3} \int_0^{R_p} \rho^2 c_s(\rho, t) d\rho \tag{4.37}$$

$$c_{\text{ss}}(t) = c_s(R_p, t) \tag{4.38}$$

Thus Eq. (4.36) can be simplified as:

$$\sigma_{\text{h,DOD}}(t) = \frac{2E\Omega_{\text{DOD}}}{9(1-\nu)} (c_{\text{s,avg}}(t) - c_{\text{ss}}(t)) \tag{4.39}$$

which says that the stresses in the particle are proportional to the volumetric strain rate and the concentration gradient in the particle. Then, the maximum and minimum stresses used in Eq. (4.30) can be calculated as:

$$\sigma_{\min} = \min\left(\sigma_{\text{h,DOD}}(t)\right) \tag{4.40}$$

$$\sigma_{\max} = \max\left(\sigma_{\text{h,DOD}}(t)\right) \tag{4.41}$$

The main effect of mechanical damage ($\Delta\varepsilon_{\text{s}}^{\pm}$ from Eq. (4.30)) on battery performance is the reduction of active material ($C_{\text{p,n}}$ from Eq. (4.22)) in the electrode ($\text{LAM}_{\text{p,n}}$). Note that the electrode degradation connects to cell capacity degradation computed as in Eq. (A.2)

based on utilization $(x_0, x_{100}, y_0, y_{100})$ of the degraded electrodes when the cell is cycled with the manufacturer's specified voltage range $(V_{\min}, V_{\max})$. Electrode LAM also leads to an increase in the current densities and thus, intercalation and side-reaction current densities. The increase in intercalation current density leads to an increase in electrode overpotentials, thus affecting the battery terminal voltage and also the resistance. Data suggests that LAM also contributes to irreversible expansion growth. The parameters to be tuned in the mechanical damage model are LAM coefficients in negative and positive electrodes $\beta^{-}_{\text{LAM},1}$, $\beta^{-}_{\text{LAM},1}$, $\beta^{+}_{\text{LAM},1}$ and $\beta^{+}_{\text{LAM},1}$, and the LAM exponent m_{LAM}. The method for tuning these parameters is shown in Section 5.2.6.

4.5 Effects of degradation mechanisms on battery performance

4.5.1 Side Reaction Currents

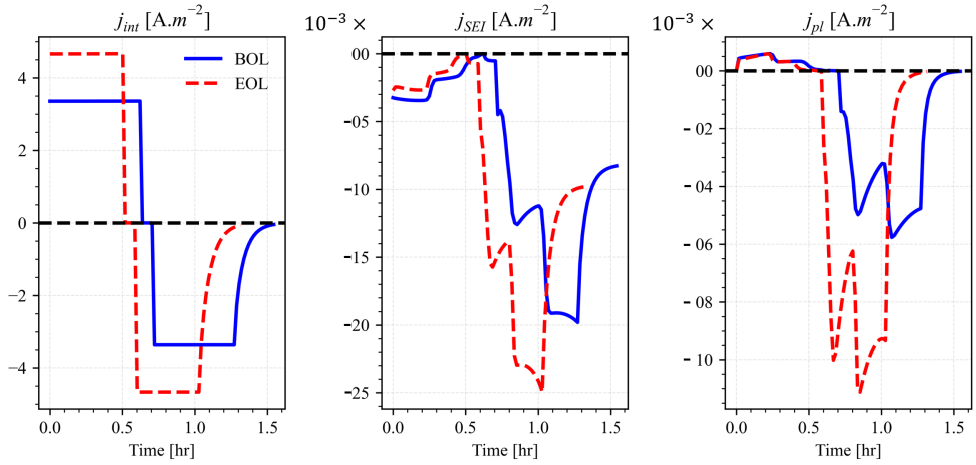


Figure 4.4: Modeled current densities of intercalation, SEI, and plating at both BOL (blue) condition and EOL (red). We observe an increase in all three current densities during 1.5C cycling at EOL (33% Capacity Loss) compared to BOL.

The current balance in the negative electrode is given by:

$$j_{\text{tot}} = j_{\text{int}} + j_{\text{pl}} + j_{\text{SEI}} \tag{4.42}$$

The total current density in the negative electrode is equal to the sum intercalation current density and the side reaction current densities. A comparison of the side reaction current

densities and the actual reaction rates for fresh and aged cell cycled at 1.5C is shown in Fig. 4.4. The values of side reaction current densities are three to four orders of magnitude lower than the intercalation current density. The model also predicts that the current densities increase in magnitude as the cell ages.

Side reaction current of SEI and Li plating reactions is given by:

$$I_{\text{side}} = -AFl^{-}a_s^{-}\left(j_{\text{SEI}} + j_{\text{pl}}\right). \tag{4.43}$$

The rate of loss of lithium inventory is given by:

$$\frac{dn_{\text{Li}}}{dt} = \frac{I_{\text{side}}}{F} + \frac{3600}{F}\left(x\frac{dC_n}{dt} + y\frac{dC_p}{dt}\right). \tag{4.44}$$

The above equation clarifies the contributions of SEI, plating and $LAM_{\text{n,p}}$ to LLI, which depends on the cycling window (x, y) from the operating voltage Eqs. (A.3) and (A.4), and depth of discharge.

4.5.2 Resistance Growth

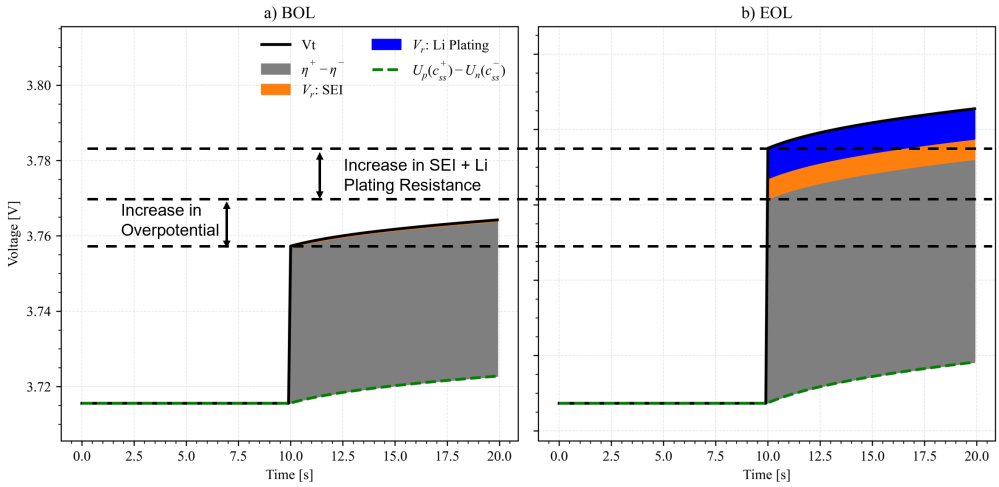


Figure 4.5: (Simulated) Components of terminal voltage for 1C charging step on a cell at BOL and EOL after cycling at 1.5C-rate and 100% DOD. At EOL, we find higher electrode overpotentials (grey) and also higher voltage rise due to an increase in SEI resistance (orange) and Li plating resistance (blue).

We observe an increase in cell resistance as the battery ages. This increase in resistance is commonly attributed to SEI growth. However, SEI growth alone does not explain the increase in cell resistance observed in cells cycled at higher C-rate, where the SEI growth is

very small. So, to explain the resistance growth observed, even in the room temperature data, we include the contribution of plated lithium to the film resistance. A physical reason for this is that the presence of plated lithium can increase the difficulty of lithium-ion transport across the electrodes. A simplified approach to capture this effect is shown below in which the contribution of lithium plating to resistance is modeled in a similar form as the contribution of SEI growth to resistance:

$$R_{\text{film}} = \frac{\delta_{\text{SEI}}}{\kappa_{\text{SEI}}} + \frac{\delta_{\text{pl}}}{\kappa_{\text{pl}}} \tag{4.45}$$

The value of film resistance greatly impacts the value of DC resistance of the cell as it ages. It depends on one set of values for the conductivities of SEI layer κ_{SEI} and plated lithium κ_{pl}, and can be tuned so that the value of DC resistance of the model matches with data. The tuning of the κ_{SEI} and κ_{pl} for all the cycling conditions considered is explained in Section 5.2.7. In our model, we assume that the film resistance in the battery comes entirely from the side reactions in the negative electrode. The cells used for degradation modeling have a NMC111 chemistry, which exhibits less degradation than cathodes with higher Nickel content [68], thus justifying our assumption. A possible extension of this work is adding cathode dissolution [69] as an additional degradation mechanism for NMC cathodes with higher Nickel content.

We can analyze the simulated contribution of SEI and Li plating to resistance growth by examining at the voltage components of a 1C pulse at BOL and EOL from a cell aged at 1.5C in Fig. 4.5. The film resistance voltage values due to SEI growth (orange) and Li plating (blue) are the major contributions to the increase in the battery resistance. These values of δ_{SEI} and δ_{pl} are very small for a fresh cell but increase as the battery ages. We can also observe an increase in electrode overpotentials (grey) due to an increase in intercalation current densities, which also leads to an increase in battery resistance.

4.5.3 Battery Expansion

Lithium intercalation and de-intercalation result in volumetric changes in both electrodes of a Li-ion battery and depend on the concentration distribution across the electrodes. These changes can be measured either by the bulk force [32] or expansion measurements [33], see [58] for a review of sensors used for measuring volume change in batteries. Expansion measurements can also be used for estimating the battery State of Charge (SOC) [34] as this expansion is a reversible function of SOC, which may be particularly helpful for the Lithium-Iron Phosphate chemistry. The Reversible expansion also gives us an indication of SOH because the reversible expansion swing depends on capacity [1].

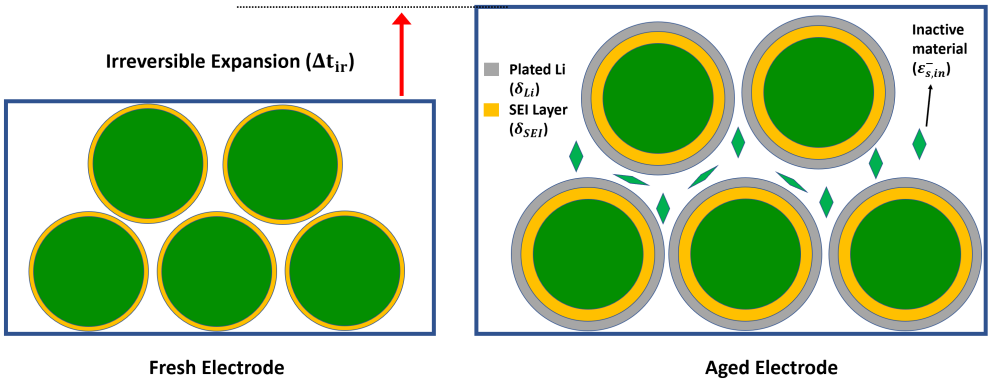


Figure 4.6: The model for irreversible changes in battery thickness (irreversible expansion) is depicted in the Figure. Growth of SEI layer δ_{SEI}, formation of plated lithium δ_{pl} and LAM which results in the formation of inactive material $\varepsilon_{\text{s,in}}$ contribute to irreversible expansion.

Another component of battery expansion is the irreversible thickness change (referred to as irreversible expansion in this work) that occurs in addition to reversible expansion as the battery ages. This irreversible expansion has been attributed to active material loss in [70] and SEI growth in [2]. We observed significant irreversible expansion in aged cells cycled at high C-rates, where SEI growth is low, and also at low-temperature [1] where both SEI growth and active material loss are low. Hence, to account for the observed irreversible expansion in the data, we include the contribution of Li plating to irreversible expansion growth in the model. However, an irreversible expansion rate that was much higher than capacity loss and resistance growth was found at EOL for batteries cycled at high C-rates Fig. 5.9, capturing this behavior required tuning a quadratic dependence of irreversible expansion rate on plating growth δ^2_{pl}. Lastly, we also observe that the irreversible expansion is proportional to the active material loss in the negative electrode and positive electrodes. This loss is represented as the inactive material volume fraction $\varepsilon_{\text{s,in}}$ given by:

$$\varepsilon_{\text{s,in}} = \varepsilon_{\text{s,0}} - \varepsilon_{\text{s}} \tag{4.46}$$

where $\varepsilon_{\text{s,0}}$ is the fresh cell active material volume fraction and ε_{s} is given by Eq. (4.30). A schematic for irreversible expansion is shown in Fig. 4.6. In this work, we attempt to create a simple irreversible expansion model where we further assume that the irreversible expansion is proportional to the values of δ_{SEI}, δ^2_{pl}, $\varepsilon^{-}_{\text{s,in}}$ and $\varepsilon^{+}_{\text{s,in}}$ giving us:

$$\delta_{\text{irrev}} = b_{\text{SEI}}\delta_{\text{SEI}} + b_{\text{pl}}\delta^2_{\text{pl}} + b^{-}_{\text{in}}\varepsilon^{-}_{\text{s,in}} + b^{+}_{\text{in}}\varepsilon^{+}_{\text{s,in}} \tag{4.47}$$

where b_{SEI}, b_{pl}, b_{in}^{-} and b_{in}^{+} are the scaling factors. These scaling factors can be tuned to match the values of the irreversible expansion of tested cells. Further discussion on tuning one set of irreversible expansion coefficients that can predict irreversible expansion beyond the tuned dataset is found in Section 5.2.8.

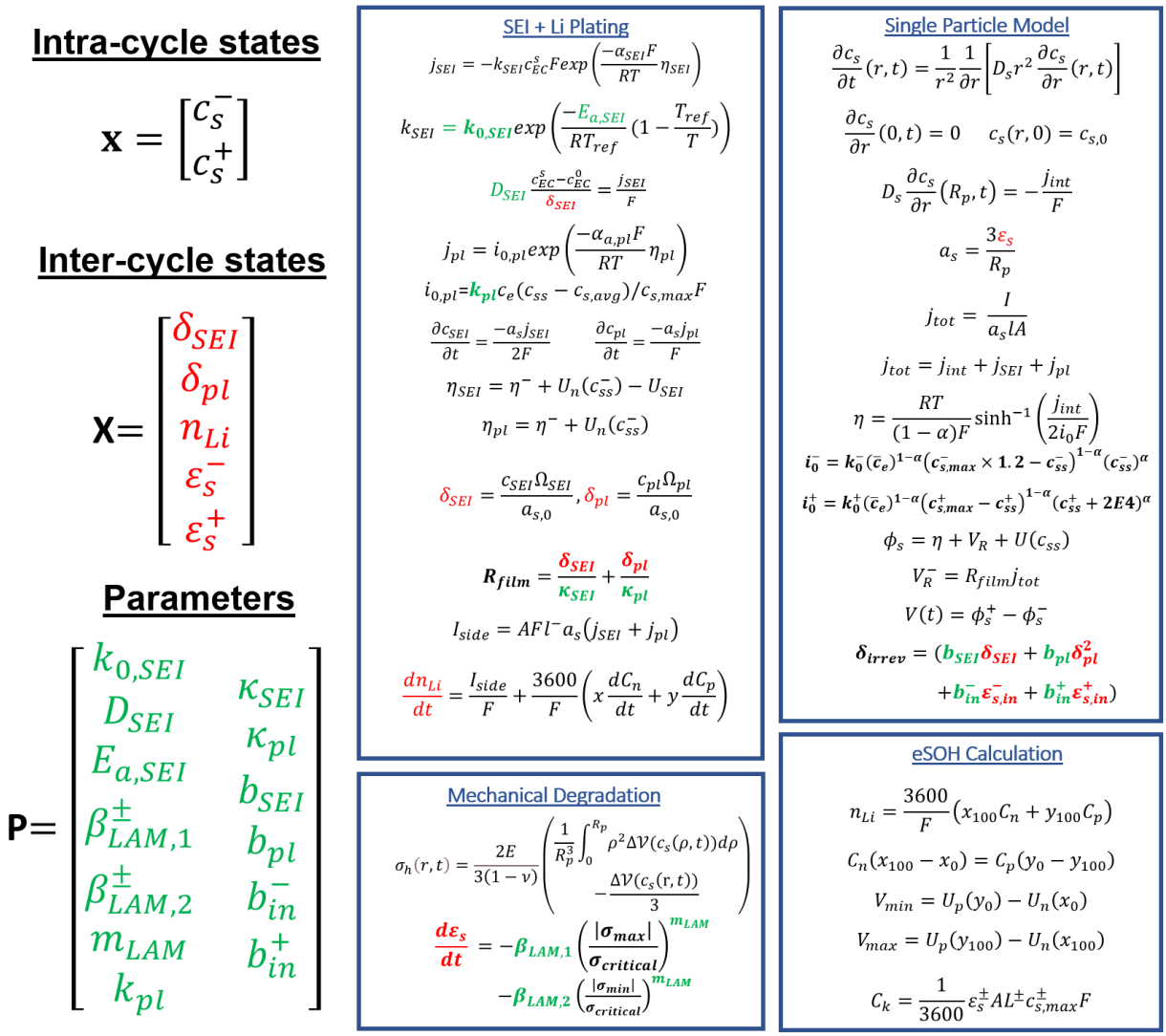


Figure 4.7: Summary of degradation model and SPM equations

4.6 Interactions Between the Degradation Mechanisms

The interactions between degradation mechanisms and with the battery are discussed in this section. A summary of degradation model and SPM equations is given in Fig. 4.7. First, let's explore mechanical degradation. The hydrostatic stress at the particle's surface is directly

proportional to the lithium concentration gradient in the particle. This stress then leads to particle damage resulting in loss of active material (LAM) of the electrode, causing a decrease in the active material ratio ε_{s}, which decreases the active material to surface ratio a_{s}. This in turn, causes an increase in current density, leading to a higher concentration gradient in the particle, resulting in higher particle stress. This decrease in a_{s} results in an increase of the SEI growth and Li plating current densities. The main effect of SEI growth and Li plating is the increase in negative electrode film resistance R_{film} and loss of lithium inventory [LLI] given by $n_{\mathrm{Li,loss}}$. The increase in resistance affects the overpotentials of reactions occurring in the battery, including side reactions like SEI growth and Li plating. The battery terminal voltage is also affected by this resistance change causing the voltage limits to be reached faster and thus reducing the battery capacity when cycling. The LLI due to SEI formation also causes a change in the stoichiometric limits for positive electrode $[y_0, y_{100}]$ and for negative electrode $[x_0, x_{100}]$ which also results in changes in the voltage output of the battery.

4.7 Conclusions

In this chapter, we model battery degradation in a Single Particle Model (SPM) framework with SEI growth and Lithium plating as side reactions, which result in loss of lithium inventory (LLI) and with mechanical damage as an additional mechanism, which results in loss of active material (LAM). In the mechanical damage model, which uses particle stress to estimate LAM, we include a novel equivalent stress to predict damage when the charge and discharge have different current values. Also, concentration-dependent stress in the negative electrode is added to predict different amounts of damage for various SOC windows the cells are cycled in. In the lithium plating model, an additional dynamic term was introduced to improve model performance at higher C-rates. Finally, for the first time, we relate observed irreversible expansion to Li Plating, SEI growth, and mechanical damage variables using a linear relationship (quadratic in the case of Li-plating).

CHAPTER 5

Tuning of Degradation Model Parameters

5.1 Introduction

Prior works on physics-based degradation models included manually [4, 12] and automatically [30, 28] tuned parameters to different values to fit simulated capacity loss to observed capacity loss using aging data for the entire battery lifetime. To compute the cost function in the parameter optimization, simulations of the entire battery lifetime need to be performed, each of which can take several minutes, which leads to the optimization taking a long time to converge. To make the optimization computationally possible as field or lab data accumulates, it is necessary to speed up the time for each iteration using accelerated battery lifetime simulations. This speed-up is achieved by simulating intra-cycle degradation, and extrapolating the changes in electrode state of health (eSOH) parameters across multiple cycles using an adaptive algorithm [3]. In this chapter we introduce a methodology of using accelerated aging simulations to tune degradation model parameters automatically. The tuning results in a single set of parameters that predicts all three SOH variables: capacity, resistance, and expansion throughout the battery lifetime for cells cycled under various current rates and SOC windows, even for cycling conditions not used for tuning.

This chapter is organized as follows. The methodology to tune the degradation model is introduced in Section 5.2. Section 5.3 describes the experimental setup and data used to tune the models. Results of model tuning and the model performance are discussed in Section 5.4. Finally, Section 5.6 summarizes the contributions.

5.2 Degradation Model Tuning Process

In this section, we develop a framework to automatically tune the degradation model parameters using battery aging data. This framework utilizes accelerated battery aging simulations to speed up lifetime aging simulations, leading to faster interactions and thus resulting in

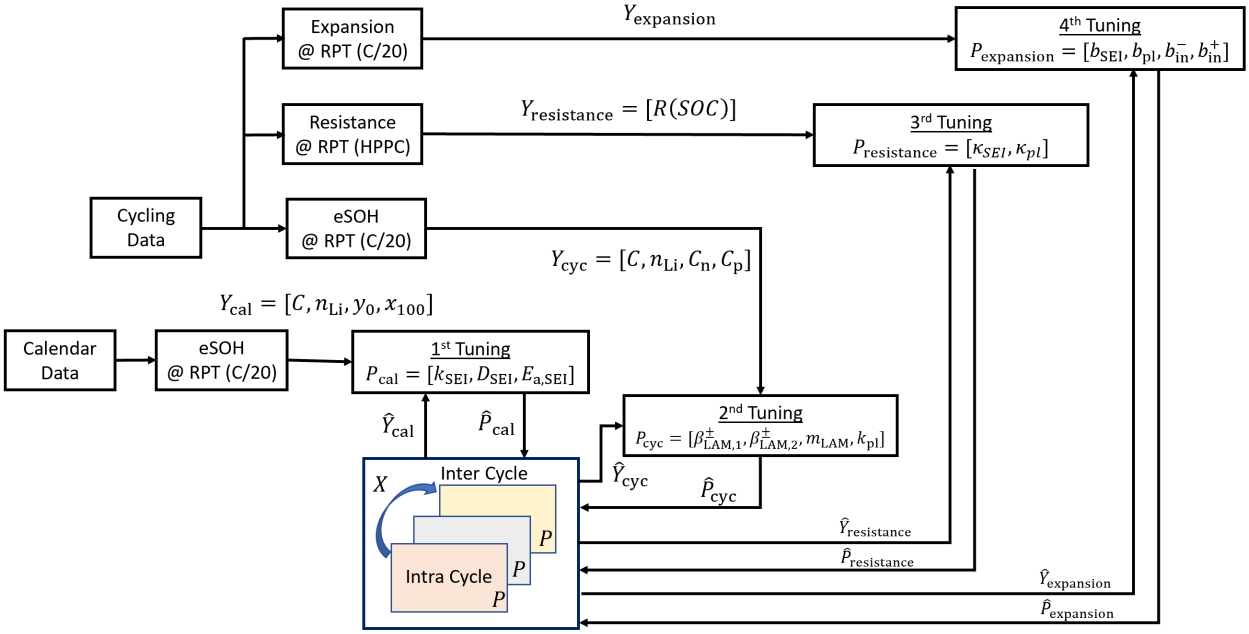


Figure 5.1: A summary of degradation model tuning process. Here P represents the vector of tunable degradation mechanisms parameters, and X represents the model states that change as the battery ages. Voltage and expansion data can be processed at RPTs to extract eSOH parameters $\tilde{Y}$. The methodology to extract eSOH parameters is explained in Chapter A. An optimization algorithm is used to find P that minimizes the error between $\tilde{Y}$ and $\hat{Y}$ (extracted from model states). We adopt a sequential tuning process, i.e. tuning SEI degradation model P_{cal} first using data from calendar aging data where other degradation mechanisms aren't active and thus don't contribute to battery degradation. We then use the tuned parameters to tune the other degradation models P_{cyc} using cycling aging data.

easier parameterization of models. A description of the algorithm used for accelerated simulations is given in Section 5.2.1. Then, in Section 5.2.2 we define the degradation variables (states) in the model and the vector of degradation model parameters to be tuned, followed by the algorithm used to tune the parameters in Section 5.2.3. After that, in Section 5.2.4, we describe the sequential tuning process and finally the results of parameter tuning for calendar aging and cycling aging in Sections 5.2.5 and 5.2.6. A summary of this process is given in Fig. 5.1. Finally, in Sections 5.2.7 and 5.2.8, we describe the process of tuning the parameters for the resistance growth and expansion model.

5.2.1 Accelerated Simulations

Since batteries age over many hundreds of cycles, physics-based simulations of the entire lifetime of a battery can take many minutes or even hours. This is prohibitively slow for iteratively refining the model of the degradation mechanisms and their interaction or tuning

the degradation mechanism parameters to match experimental data. To speed this lifetime simulation up, we use an adaptive inter-cycle extrapolation algorithm introduced by Sulzer et al. [3]. This allows simulation of the entire lifetime in just a few seconds, enabling rapid iteration to match experimental data. A brief description of the algorithm is presented in this section, and we refer the reader to [3] for further details.

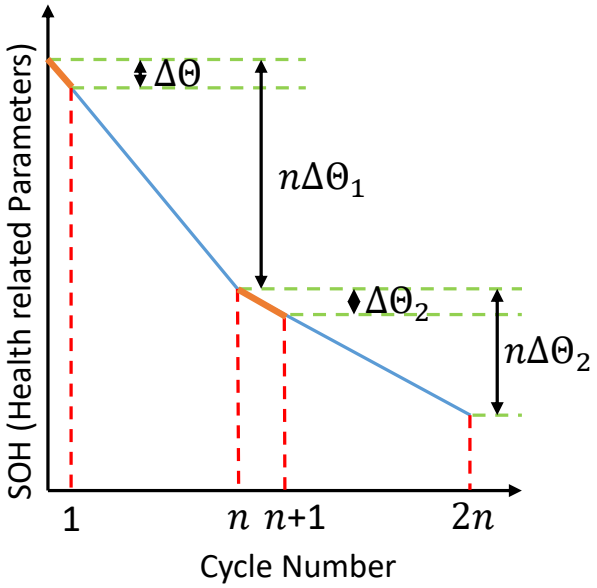


Figure 5.2: Inter-cycle extrapolation, from [3]. The change in SOH parameters over one cycle, Δy_1, is assumed to be constant for the next n cycles, resulting in a $n\Delta y_1$ change over n cycles. The change in SOH over the n^{th} cycle is then calculated and extrapolated to the $2n^{\text{th}}$ cycle, etc. Here SOH represents an internal degradation variable of the model, of which there can be several, for example SEI thickness (k_{SEI}) or active material volume fraction in either electrode ($\varepsilon_{\text{s}}^{\pm}$).

The adaptive inter-cycle extrapolation algorithm is based on two key ideas: first, since the degradation timescale is slow relative to the cycling timescale, the change in the degradation variables over one cycle can be extrapolated over several cycles (Figure 5.2); and second, this can be done adaptively for optimal accuracy-efficiency trade-off. We first explain the fixed-step inter-cycle extrapolation algorithm, as introduced for example by Kupper et al. [71] and Vora et al. [72]. At each iteration of this algorithm, we first calculate the amount of degradation over a single cycle by directly simulating the cycle, then linearly extrapolate the amount of degradation over n cycles. The hyper-parameter n must be selected ahead of time to take large enough steps while remaining accurate in non-linear regions, which is difficult to do: different degradation models will have different optimal step sizes.

This difficulty in hyper-parameter selection naturally suggests that the algorithm should

be made adaptive, with the extrapolation step size depending on the rate of change of degradation rate. Since the underlying degradation is continuous from cycle to cycle, we can thus write an ODE

$$\frac{\mathrm{d}\boldsymbol{\Theta}}{\mathrm{d}t} = \Delta\boldsymbol{\Theta}, \tag{5.1}$$

where $\boldsymbol{\Theta}$ represents the vector of slowly changing degradation variables. We can then solve this ODE using any adaptive time-stepping algorithm (Runge-Kutta 3(2) in this thesis). At each timestep in the ODE solver, we must solve a full charge/discharge cycle obtain $\Delta\boldsymbol{\Theta}$. We use PyBaMM [61] to simulate these single cycles.

5.2.2 Degradation Mechanism States and Parameters

We now describe the vector of degradation mechanism states X based on the degradation mechanisms discussed in the previous sections. These are the four state variables for the degradation equations Eqs. (4.7), (4.18) and (4.30) (δ_{SEI}, δ_{pl}, $\varepsilon_{\text{s}}^{-}$, and $\varepsilon_{\text{s}}^{+}$), plus the total lithium inventory, n_{Li}, which is used instead of the particle concentration state variables to track LLI since degradation variables should evolve on the slow degradation timescale [3].

$$\boldsymbol{X} = \left[n_{Li}, \delta_{\text{SEI}}, \delta_{\text{pl}}, \varepsilon_{\text{s}}^{-}, \varepsilon_{\text{s}}^{+}\right]^{T} \tag{5.2}$$

The first state here is the amount of cyclable lithium in the battery n_{Li} which decreases due to the lithium loss in the battery. The state variable is the thickness of the SEI layer δ_{SEI}, which increases due to the formation of new SEI as the battery ages. Next, we have δ_{pl} which is the thickness of plated lithium. The last two states are active material ratios of the negative and positive electrodes, $[\varepsilon_{\text{s}}^{-}, \varepsilon_{\text{s}}^{+}]$ which decreases according to Eq. (4.30). Next, we define the vector of degradation mechanism parameters P to be tuned to match the model with data. Depending on the available data and the interaction between the degradation mechanisms, we can tune a particular sub-model individually or tune two or more sub-models simultaneously.

5.2.3 Parameter fitting

This section introduces a tuning methodology to fit the degradation mechanism model output to the data. We want to take advantage of the fact that the simulation time for a battery's lifetime takes only a few seconds. Least squares optimization can be used on the simulation output and the data to get the tuned model parameters. However, it is not possible to calculate the derivatives for optimization in our case. So we utilize derivative-free least squares optimization algorithm DFO-LS [31], which does not require us to provide derivatives

for optimization and does not attempt to estimate them internally.

1. Define vector of degradation mechanism parameters P to be tuned for a particular problem.

$$P = \left[p^1, p^2, \ldots, p^{n_1}\right]^T \tag{5.3}$$

2. Define a vector of data to be fitted against the model outputs.

$$Y = \left[y^1, y^2, \ldots, y^{n_2}\right]^T \tag{5.4}$$

   The data chosen here are eSOH parameters extracted from voltage and expansion data. The methodology to extract eSOH parameters is explained in Appendix A. The model states X can also be processed to extract the eSOH parameters from the simulation. eSOH parameters are chosen here since they provide additional information on degradation mechanisms, compared to using only capacity.

3. Run DFO-LS to solve least squares optimization problem to estimate degradation mechanism model parameters.

$$\hat{P} = \arg\min_{P} f(x) = \sum_{k=1}^{n_3} \frac{1}{m_{n_3}} \sum_{j=1}^{n_2} w^j \sum_{i=1}^{m_{n_3}} \left(\tilde{y}_i^j - \hat{y}^j(x_i, P)\right)^2 \tag{5.5}$$

   where $\hat{y}^j(x_i, P)$ is the corresponding model output to the data $\tilde{y}^j$ for the observation point x_i. The model outputs and observation points can be taken from one or more cells, where number of cells is given by n_3. The number of observation points m_{n_3} refers to the number of reference performance tests (RPTs) conducted on the cell. Since the number of RPTs is different for each cell, the cost for each cell is normalized with the number of RPTs m_{n_3} to have equal weight applied to data from each cell. Data from multiple cells is necessary to tune temperature dependency in calendar aging and C-rate dependency in cycling aging. Appropriate weights w^j are applied to normalize the outputs. These weights depend on the model outputs Y selected for tuning.

5.2.4 Sequential Tuning Process

Tuning multiple degradation models simultaneously with data from multiple aging conditions would be extremely difficult since battery degradation is nonlinear. This leads to solver being unable to find the solution due to local minima. To resolve this issue we adopt a sequential

tuning process, i.e. tuning certain degradation models first using data from conditions where other degradation mechanisms aren't active and thus don't contribute to battery degradation. We then use the tuned parameters from the initial tuning and tune the other degradation models. Specifically, we use the following sequence.

1. Use calendar aging data for multiple temperatures to tune the SEI model. In this case the contribution of mechanical damage and Li plating to aging would be negligible.

2. Use multiple cycling aging data sets with different C-rates and DODs to tune the Li plating and mechanical damage models simultaneously.

5.2.5 Parameterization of Degradation Mechanisms during Calendaring Aging

First, we tune the degradation due to SEI growth using the data from the calendar aged cells in both cold (-5°C) and hot temperature (45°C) conditions. The reason for doing this is to capture the temperature dependency of SEI growth, being faster at high temperatures and slower at colder temperatures. To capture this temperature dependency, we introduce an Arrhenius equation for k_{SEI}:

$$k_{\text{SEI}} = k_{0,\text{SEI}} exp\left(\frac{-E_{a,SEI}}{RT_{\text{ref}}}(1 - \frac{T_{\text{ref}}}{T})\right) \tag{5.6}$$

where $E_{a,SEI}$ is activation energy of SEI reaction, T_{ref} is reference temperature of $298.15K$ and $k_{0,\text{SEI}}$ is kinetic rate constant at T_{ref}. During calendar aging, there is no mechanical degradation because there is no cycling of the current in the cell and thus no stresses in the particle. We want to tune the SEI degradation parameters, SEI kinetic rate constant $k_{0,\text{SEI}}$, SEI layer diffusivity D_{SEI} and SEI kinetic rate Arrhenius coefficient $E_{a,\text{SEI}}$ to fit the battery capacity C, amount of cyclable lithium n_{Li}, which is related to the loss of lithium inventory (LLI), and the stoichiometric limits y_0 and x_{100}. So, P and Y here are:

$$P_{\text{cal}} = [k_{0,\text{SEI}}, D_{\text{SEI}}, E_{a,\text{SEI}}]^T \tag{5.7}$$

$$Y_{\text{cal}} = [C, n_{\text{Li}}, y_0, x_{100}]^T \tag{5.8}$$

The reduced data for fitting in the vector Y are described in Section 5.3. These values are calculated from the periodic C/20 discharges taken with each RPT using the method from [1]. Data sets from the calendar aged cells at 100% SOC at -5°C and 45°C were used to tune the model. The weights used in the optimization function Eq. (5.5) for each of the

four states of health Y_{cal} are given by:

$$W = [1/5, 5, 1, 1] \tag{5.9}$$

The weights are chosen such that all the outputs in Y_{cal} have approximately equal importance.

5.2.6 Parameterization of Degradation Mechanisms during Cycling Aging

Next, we tune the mechanical degradation model parameters $\beta^-_{\text{LAM},1}$, $\beta^-_{\text{LAM},2}$, $\beta^+_{\text{LAM},1}$, $\beta^+_{\text{LAM},2}$ and m_{LAM} along with Lithium plating kinetic rate constant k_{pl} to fit the battery capacity C, amount of cyclable lithium n_{Li}, and the electrode capacities C_n and C_p. The parameters $k_{0,\text{SEI}}, D_{\text{SEI}}$ and $E_{a,\text{SEI}}$ used here are the ones tuned in the calendar aging section. P and Y here are:

$$P_{\text{cyc}} = \left[\beta^-_{\text{LAM},1}, \beta^-_{\text{LAM},2}, \beta^+_{\text{LAM},1}, \beta^+_{\text{LAM},2}, m_{\text{LAM}}, k_{\text{pl}}\right] \tag{5.10}$$

$$Y_{\text{cyc}} = [C, n_{\text{Li}}, C_n, C_p]^T \tag{5.11}$$

The parameters P_{cyc} were tuned based on the data sets Y_{cyc} extracted from the RPTs of the cycling cells at charge-discharges rates of C/5-C/5-100%DOD, 1.5C-1.5C-100%DOD, and C/5-1.5C-100%DOD. The reason for tuning the model using the three cells together is to establish the C-rate dependency of the mechanical damage and Li plating models. Using data from a single C-rate would be insufficient to get the C-rate dependency correct in the model. If we use only the symmetric cycling cells, the tuning algorithm will attribute the LAM completely to $\beta^-_{\text{LAM},2}$ and $\beta^+_{\text{LAM},1}$, that is the values of $\beta^-_{\text{LAM},1}$ and $\beta^+_{\text{LAM},2}$ will be 0. Hence, the asymmetric cycling cell (C/5 charge, 1.5C discharge) has to be added to tuning. The weights used for tuning here are given by:

$$W = [1, 25, 1, 1] \tag{5.12}$$

The weights are chosen such that all the outputs in Y_{cyc} have approximately equal importance.

5.2.7 Parametrization of Resistance model

The growth in film resistance is given by Eq. (4.45). There are two parameters in the equation which are needed to be tuned to match data: κ_{SEI} and κ_{pl}

$$P_{\text{resistance}} = [\kappa_{\text{SEI}}, \kappa_{\text{pl}}] \,. \tag{5.13}$$

These parameters were tuned manually to get the best resistance fit at both low C-rate (C/5) and high C-rate (1.5C). The tuned conductivity values are shown in Table 5.4.

5.2.8 Parameterization of Expansion model

The irreversible expansion model is given by Eq. (4.47) and introduced the scaling factors b_{SEI}, b_{pl}, b_{in}^{-} and b_{in}^{+}

$$P_{\text{expansion}} = \left[b_{\text{SEI}}, b_{\text{pl}}, b_{\text{in}}^{-}, b_{\text{in}}^{+}\right] . \tag{5.14}$$

The parameters $P_{\text{expansion}}$ were tuned based on the expansion data extracted from the RPTs of the cycling cells at charge-discharges rates of C/5-C/5-100%DOD, 1.5C-1.5C-100%DOD, and C/5-1.5C-100%DOD. These are the same cells that were used to tune the mechanical damage and lithium plating models. A least squares estimation algorithm was used to find scaling factor values. The tuned scaling factors are shown in Table 5.4.

5.3 Experiments and Data

The cells used in this study are manufactured in University of Michigan Battery Lab and have a fresh cell capacity of 5 Ah. Anode is made from Artificial Graphite (Hitachi MAGE3), and the cathode is comprised of polycrystalline NMC111 (Toda North America). The binder

Table 5.1: Time for Experiments and Simulations

	Cycling conditions	
	Calendar Aging	C/5 Cycling
Experiment	250 days	150 days
Full Simulations	4 minutes	3 minutes
Accelerated Simulations	17 seconds	10 seconds
Parameter Tuning	3 minutes	4 minutes

used in the electrodes is PVDF and the electrolyte is 1M $LiPF_6$ in 3:7 EC:EMC w/ 2% by weight of VC. Further details regarding the cell and cell parameters are given in [33].

All the cells considered in this chapter are cycled at **room temperature** $25\,^{\circ}C$. The data used to tune (train) the model is from operating at 100% DOD for cells cycled at C/5, 1.5C, and mixed C-rate (C/5 charge, 1.5C discharge) from 3V to 4.2V. The aging process of the cells used in this study is summarized in Section 5.3.1 followed by the aging characterization method and eSOH (Electrode State of Health) estimation in Section 5.3.2.

5.3.1 Aging Methodology

The cells used in this study were placed in a battery fixture located in a thermal chamber set at 25°C. Then, two different types of aging were performed on the batteries:

5.3.1.1 Calendar Aging

Calendar aging at two different state of charge (SOC) was performed. One cell was fully charged (100% SOC), and the second cell was discharged to 50% SOC before being placed in the fixture. These cells were then calendar aged for 250 days.

5.3.1.2 Constant Current Cycling Aging

Here the batteries were cycled at a constant current for 100% depth of discharge (DOD) and 50% DOD. The cycling is composed of a constant current (CC) charge at C/5 until the battery reaches 4.2 V, followed by constant voltage charging (CV) at 4.2 until the current drops below C/50. Then a CC discharge was performed till the battery reached 3.0 V. For the 50% discharge case, the DOD is with respect to nominal capacity.

5.3.2 Performance Testing and eSOH calculation

The above cells were cycled to at least 80% capacity retention, and the characterization tests were performed periodically. These tests include C/20 charge-discharge cycle required for eSOH estimation. The C/20 charge voltage data is used for estimating eSOH parameters by using the voltage fitting method as described in Appendix A.2. The eSOH parameters estimated here are capacities of positive and negative electrodes C_{p} and C_{n} and the electrode utilization range/ stoichiometric limits for positive electrode $[y_0, y_{100}]$ and for negative electrode $[x_0, x_{100}]$.

5.4 Results and Discussion

The degradation model is tuned using the methodology shown in Section 5.2. The tuned model is used to predict various metrics as the battery ages, including capacity, degradation modes of LAM and LLI, cycling voltage, DC resistance, irreversible expansion, and total expansion (reversible and irreversible expansion) for cells cycled under various conditions, including those not used to tune the model.

The simulations of training cells will be represented by dashed lines in this section. The data used for prediction (testing) is from operating at 100% DOD for 2C, 50% DOD for C/5, and 50% DOD for mixed C-rate cycling. The 50% DOD cells are cycled between a SOC window of 50%-100%. The simulations of the prediction cells will be represented by solid lines in this section.

5.4.1 Model Tuning Results

The results of model tuning of the first two sequential steps are discussed here.

A comparison of the capacity and key eSOH indicators extracted from the model simulation and experimental data for calendar aging are shown in Fig. 5.3. We see that C_{p} and C_{n} do not change much in both data and model. The positive and electrode stoichiometric limits are also in good agreement with the data as do cell capacity and LLI. LLI is calculated from n_{Li} shown in Eq. (A.5).

A comparison of the capacity and key eSOH indicators extracted from the model simulation and experimental data for cycling aging aging are shown in Fig. 5.4. We see that eSOH and LLI from the simulations are in excellent agreement with the data. The stoichiometric limits in the simulations also show similar trends to the data.

5.4.2 Capacity Prediction

The first aging metric we will analyze is the battery capacity. Percent capacity retention for cells cycled with 100% DOD at various C-rates are shown in Fig. 5.5 a). The model predicts the capacity well for the conditions it was tuned at i.e. at C/5, 1.5C and mixed C-rate aging (C/5 Charge and 1.5C Discharge) with RMSE of capacity prediction under 2%, but under-predicts capacity loss at the higher current of 2C with RMSE of capacity prediction of over 4%. The under-prediction of capacity can be traced to the under-prediction of LAM in the negative electrode. Also, the model fidelity at higher C-rates deteriorates because we are using an SPM and a phenomenological factor Eq. (4.17) which does not account for the spatial variability in degradation due to electrolyte concentration depletion and increased

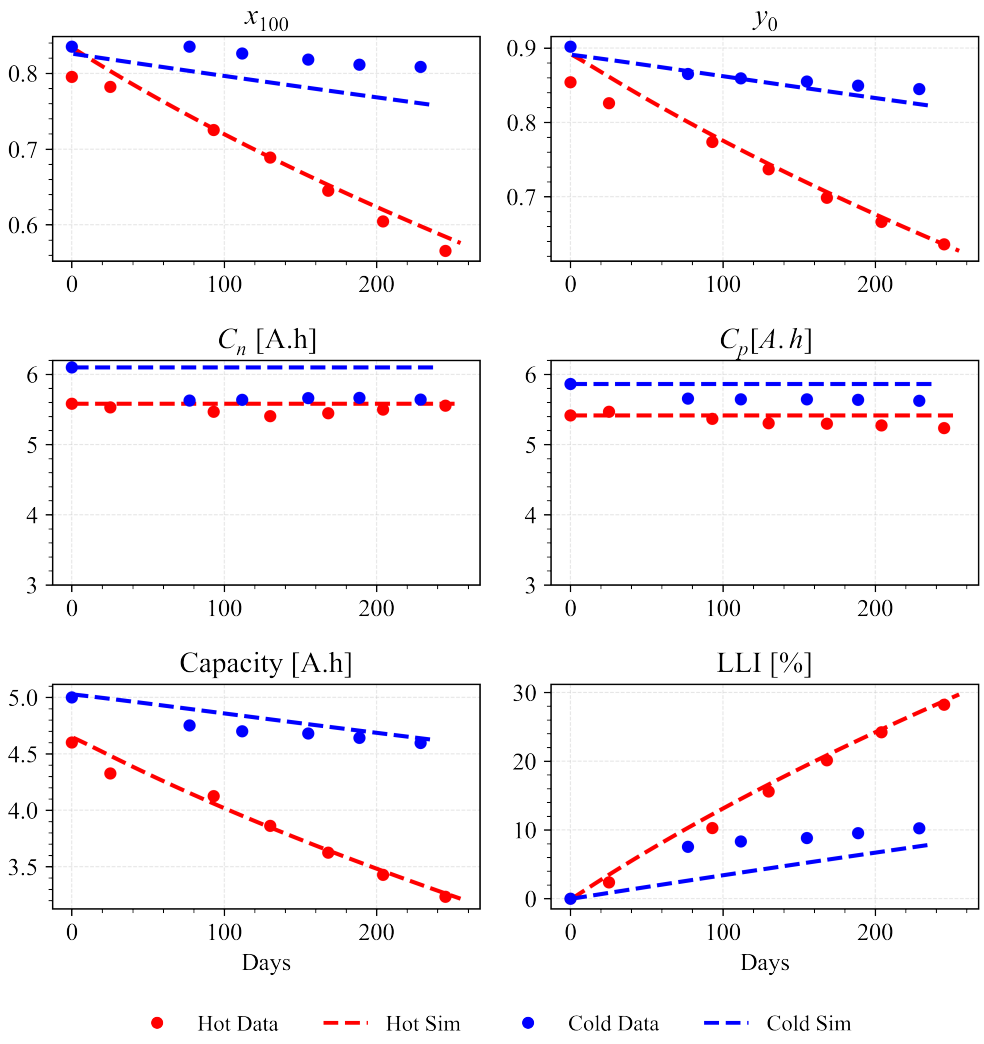


Figure 5.3: The SEI growth model is tuned to match capacity loss and lithium loss for calendar aged cells stored at 100% SOC at 45°C (red) and -5°C (blue). Capacity, LLI, and eSOH parameters are shown here for data(markers), and simulations (lines).

rates of plating at the separator interface.

The percent capacity retention for cells cycled with 50% DOD is compared with 100% DOD cells are shown in Fig. 5.5 b). Both the data and model for C/5 cycling aging show similar capacity loss rates at both 50% and 100% DOD, which is captured well by our model with RMSE of capacity prediction at 1.1% over the battery lifetime.

5.4.3 Degradation Mechanism and Modes

Here we analyze the three degradation modes of the battery: Loss of Active material in negative and positive electrode ($\mathrm{LAM_{NE}}$,$\mathrm{LAM_{PE}}$) and Loss of Lithium Inventory (LLI). The

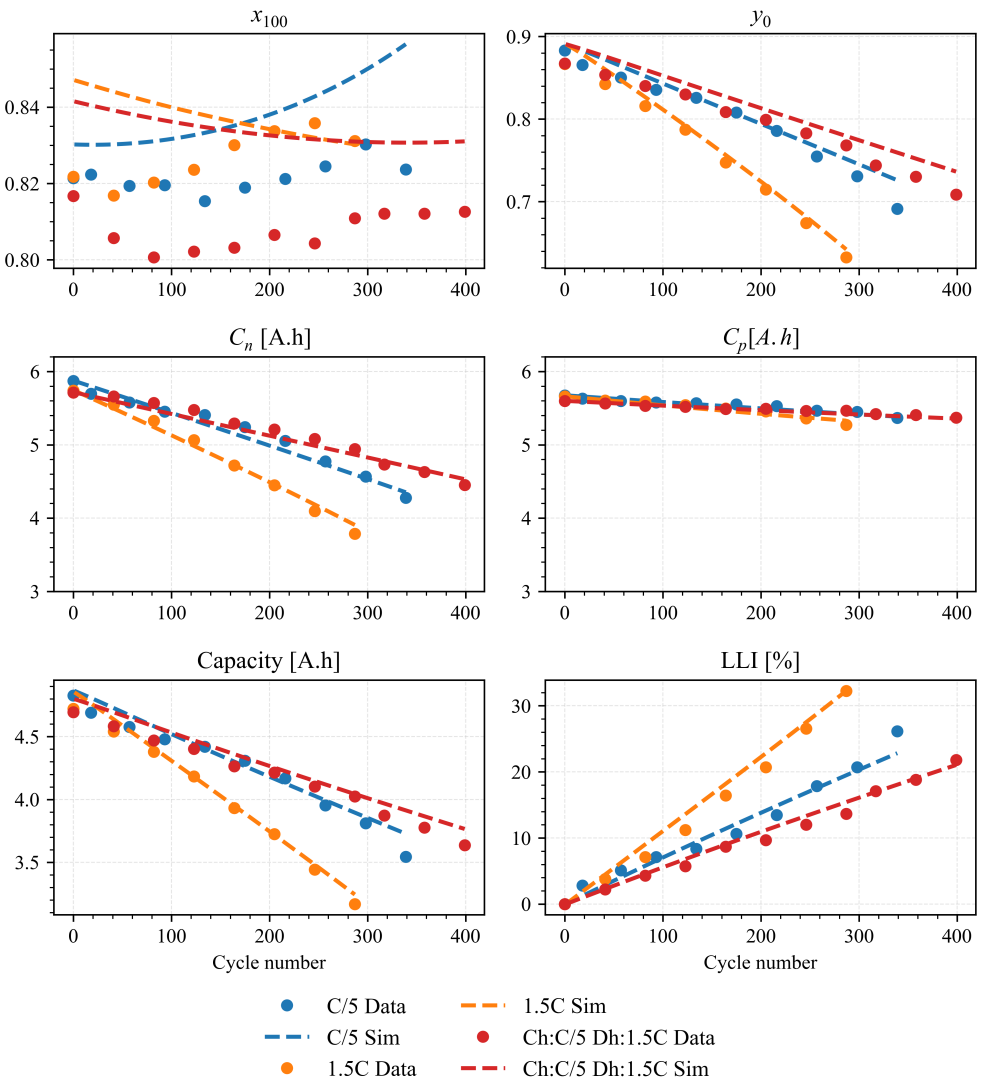


Figure 5.4: The mechanical damage model and lithium plating model is tuned to match capacity loss, lithium loss and active material loss for cells cycled at C/5 (blue), 1.5C (red) and C/5 Charge 1.5C Discharge (orange) for 100% DOD. Capacity, LLI, and eSOH parameters are shown here for data(markers), and simulations (lines).

value of the degradation modes represents the change in the internal states of the battery. These metrics are shown for 100% DOD cycle aged cells in Fig. 5.6 and are calculated as shown in Eqs. (A.5) to (A.6). We observe that the values of LAM_{NE} are much higher than the values of LAM_{PE} both for the simulations and in data. Also, from Eq. (4.44), we deduce that both side reactions (I_{side}) and LAM (C_p, C_n) contribute to LLI. But, because LAM_{NE} is very high, it also contributes significantly to the value of LLI. This means that the dominant aging mechanism in these cells is LAM_{NE}, which is captured by the model at multiple c-rates.

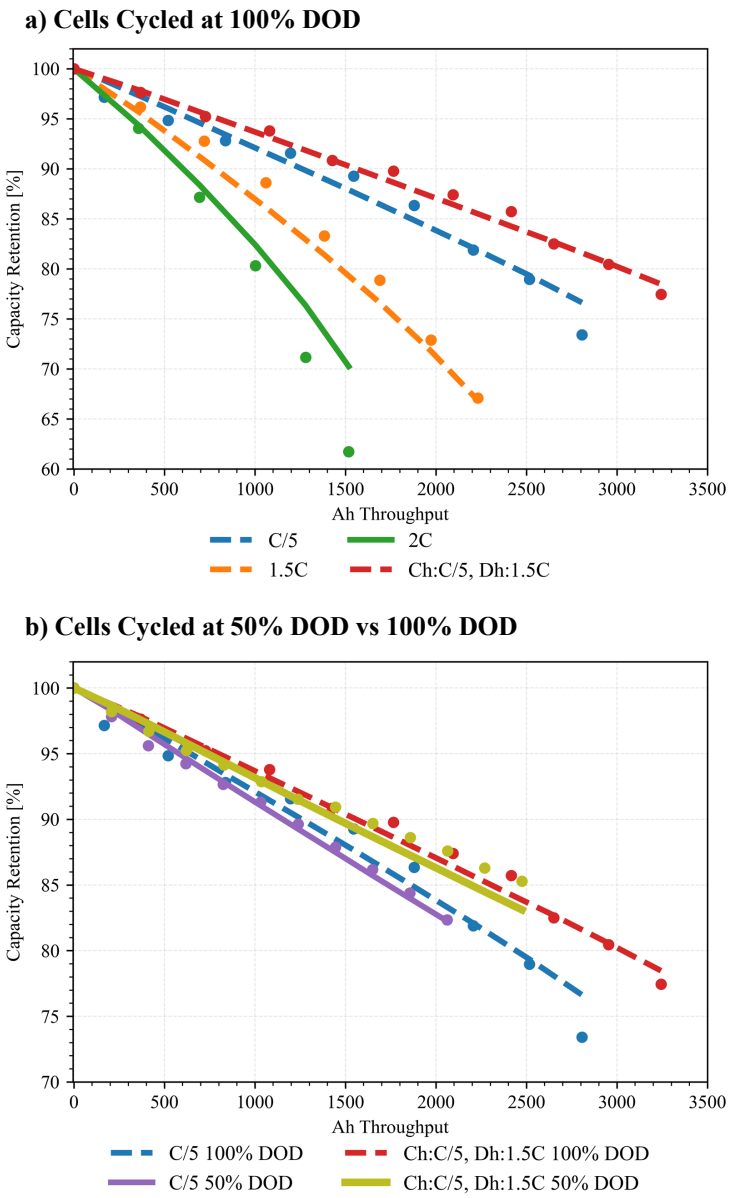


Figure 5.5: Capacity Prediction for a) 100% DOD cells b) 50% DOD vs 100% DOD cells. Cell nominal capacity is 5 Ah and the cells were cycled at 25°C

. Data is shown as markers and the simulation is shown as lines. Dashed lines show the simulations on trained cells, and solid lines show predictions on untrained cells.

5.4.4 Resistance Prediction

In this section, we will analyze the prediction of resistance growth for all cells and also the resistance profile vs SOC as the cell ages for select cells. Fig. 5.7 a) shows the resistance growth in % for various cells cycled for 100% DOD. Resistance is calculated by using HPPC (Hybrid Pulse Power Characterization) test data performed during RPT. Both charge and

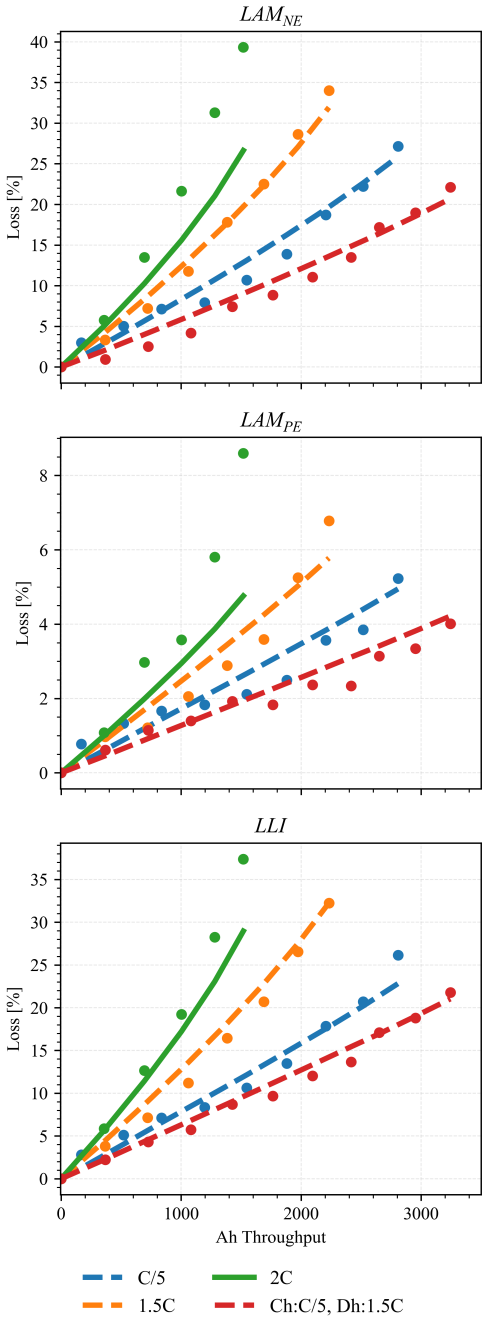


Figure 5.6: Degradation Modes Prediction for 100% DOD Cells. Cell nominal capacity is 5 Ah and the cells were cycled at $25°C$

. Data is shown as markers and the simulation is shown as lines. These plots show that the dominant mode of degradation is LAM in the negative electrode.

discharge pulses at 1C run at regular SOC intervals are used to estimate resistances at different SOCs. These resistances are finally averaged over all SOCs and normalized with respect to the fresh cell averaged resistance to calculate resistance growth. For C/5 and 1.5

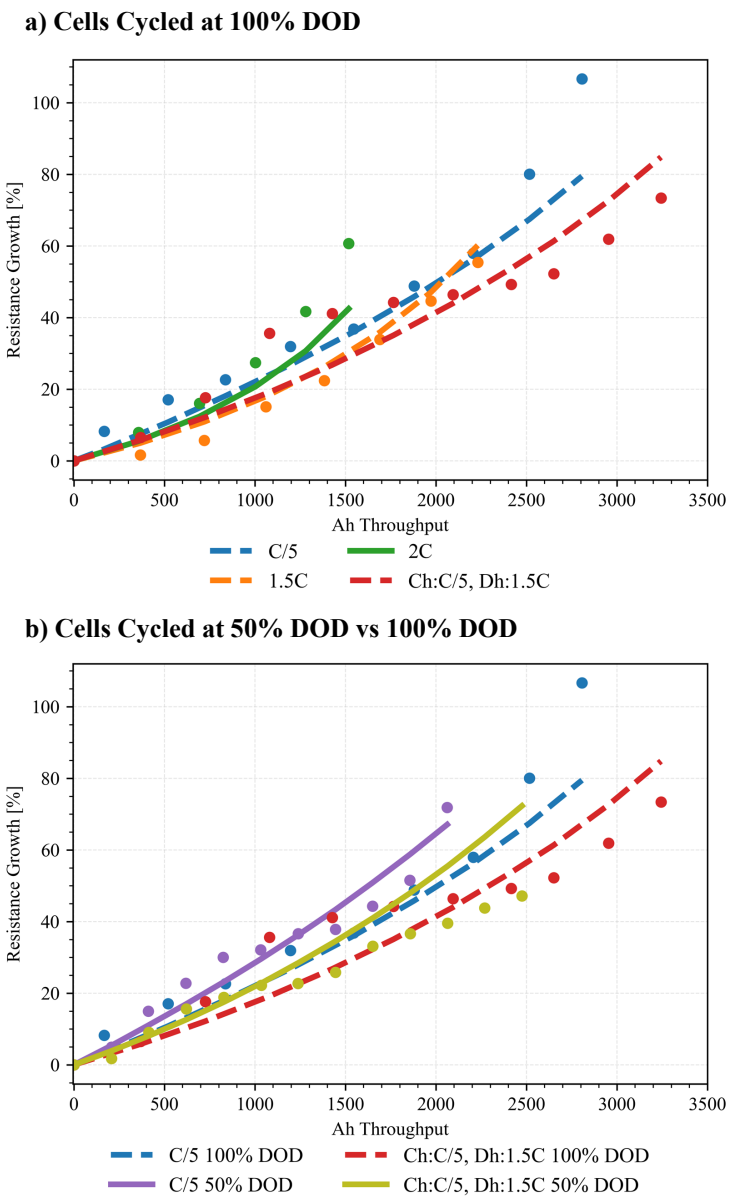


Figure 5.7: Resistance Growth Prediction for a) 100% DOD cells b) 50% DOD vs 100% DOD cells. Cell nominal capacity is 5 Ah and the cells were cycled at 25°C. HPPC test data with 1C pulses averaged over various SOCs is used to calculate cell resistance. Data is shown as markers and the simulation is shown as lines. Dashed lines show the simulations on trained cells, and solid lines show predictions on untrained cells. The resistance is averaged over charge and discharge pulses and over SOC.

cycle aged cells, the resistance growth is predicted well for most of the life. But at EOL for C/5 we see a sharp increase in resistance which isn't predicted by the model. For a 2C cycle aged cell we predict resistance growth well until MOL (middle of life) after which the

error in prediction increases. The underprediction might be due to higher Li plating in the cell which is not predicted by our model. For mixed C-rate cell, prediction of resistance growth is sufficient at BOL and EOL but the model under-predicts the resistance growth at MOL. From the resistance growth data at mixed C-rate we can see that there is an initial exponential growth, which transitions to another exponential growth at MOL, resulting in two different resistance growth rate, one at BOL and the other from MOL to EOL. This growth rate might correspond to two different resistance growth mechanisms in the cell, one which is dominant at BOL, and the other at MOL. Our model doesn't predict this behavior since the simulations show only a single growth rate at both BOL and MOL. This behavior can also be observed in data for other cells, but to a lower extent. For cells cycled at 50% DOD shown in Fig. 5.7 b), the model predicts higher resistance growth compared to 100% DOD cells, which is also observed in the data. The higher resistance growth at 50% DOD is because the SEI growth is higher at higher SOC range thus resulting in higher resistance growth.

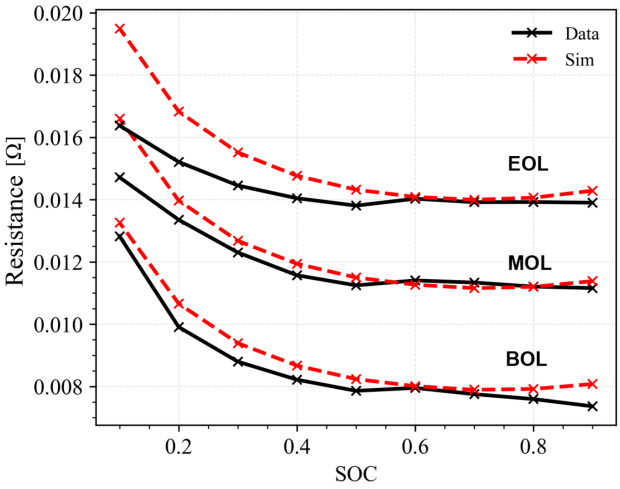


Figure 5.8: Resistance vs SOC at BOL, MOL, and EOL for C/5 100% DOD Cycling Aging Cell. HPPC test data with 1C pulses is used to calculate cell resistance. Resistance plotted is the average of charge and discharge resistance. Data is shown in black and simulation is shown in red. The model captures variation in resistance with SOC and also the resistance growth as the battery ages.

Fig. 5.8 shows the DC resistance vs SOC plots at BOL, MOL, and EOL for cell cycled at C/5. From the data (black) we see that the resistance is very high at low SOC but decreases as the SOC increases. At MOL and EOL we also see that the resistance values are almost same from middle SOCs to high SOC. This shape of resistance profiles depends on the overpotentials of the negative and positive electrode as shown in Fig. 4.5, which depends on the exchange current density i_0. The conventional formulation of exchange current density

shown below doesn't seem to capture the resistance profile in our model

$$i_0 = k_0 \left(\bar{c_e}\right)^{(1-\alpha)} \left(c_{s,max} - c_{ss}\right)^{(1-\alpha)} \left(c_{ss}\right)^{\alpha}. \tag{5.15}$$

A similar analysis is also found in literature [73]. To correct the issue, we modify the exchange current density as shown below:

$$i_0^- = k_0 \left(\bar{c_e}^-\right)^{(1-\alpha)} \left(c_{s,max}^- \times 1.2 - c_{ss}^-\right)^{(1-\alpha)} \left(c_{ss}^-\right)^{\alpha} \tag{5.16}$$

$$i_0^+ = k_0 \left(\bar{c_e}^+\right)^{(1-\alpha)} \left(c_{s,max}^+ - c_{ss}^+\right)^{(1-\alpha)} \left(c_{ss}^+ + 20000\right)^{\alpha}. \tag{5.17}$$

After implementing the modifications in exchange current density we find good model (red) prediction for resistance vs SOC profile at BOL as seen in Fig. 5.8. As the cell ages we see that we predict values well at middle to higher SOCs but not very good at lower SOCs. This is because the overpotentials are higher when the battery ages (since the current densities in the electrodes are higher due to LAM) as discussed in Section 4.5.1.

5.4.5 Irreversible Expansion Prediction

We discuss the prediction results of the irreversible expansion model in this section. These results are shown for full DOD cells in Fig. 5.9 a). We see that the values of irreversible expansion predicted by the model have a good fit with data for C/5 and 1.5C for most of the battery life. At mixed C-rate, the model over-predicts irreversible expansion for most of the life, but the prediction error is low at EOL. The RMSE of irreversible expansion is under 20 μm for the trained cells but has a higher value of 30 μm for 2C cell, with most of the error coming at EOL. Table 5.4 shows us that positive electrode expansion scaling factor b_{in}^+ has a value of 0. This means that in the tuned expansion model, the positive electrode doesn't contribute to the irreversible thickness change. As discussed earlier in Section 5.4.3, LAM_{PE} is much lower than LAM_{NE}, thus the change in inactive material volume fraction $\varepsilon_{\text{s,in}}$ in positive electrode is negligible compared to the negative electrode. So the expansion model isn't very sensitive to the values of b_{in}^+, compared to the other scaling factors, thus resulting in $b_{\text{in}}^+ = 0$.

The prediction of irreversible expansion for 50% DOD cells are shown in Fig. 5.9 b). We observe that the model predicts slightly higher irreversible expansion for both C/5 and mixed C-rate cycled aged cells. Data shows similar irreversible expansion at C/5 for both 50% and 100% DOD cells but the model predicts higher irreversible expansion because the predicted SEI growth is higher for 50% DOD cells, with RMSE of prediction error less than 20 μm (0.5% of fresh cell thickness). Higher SEI growth for 50% DOD cells is because the

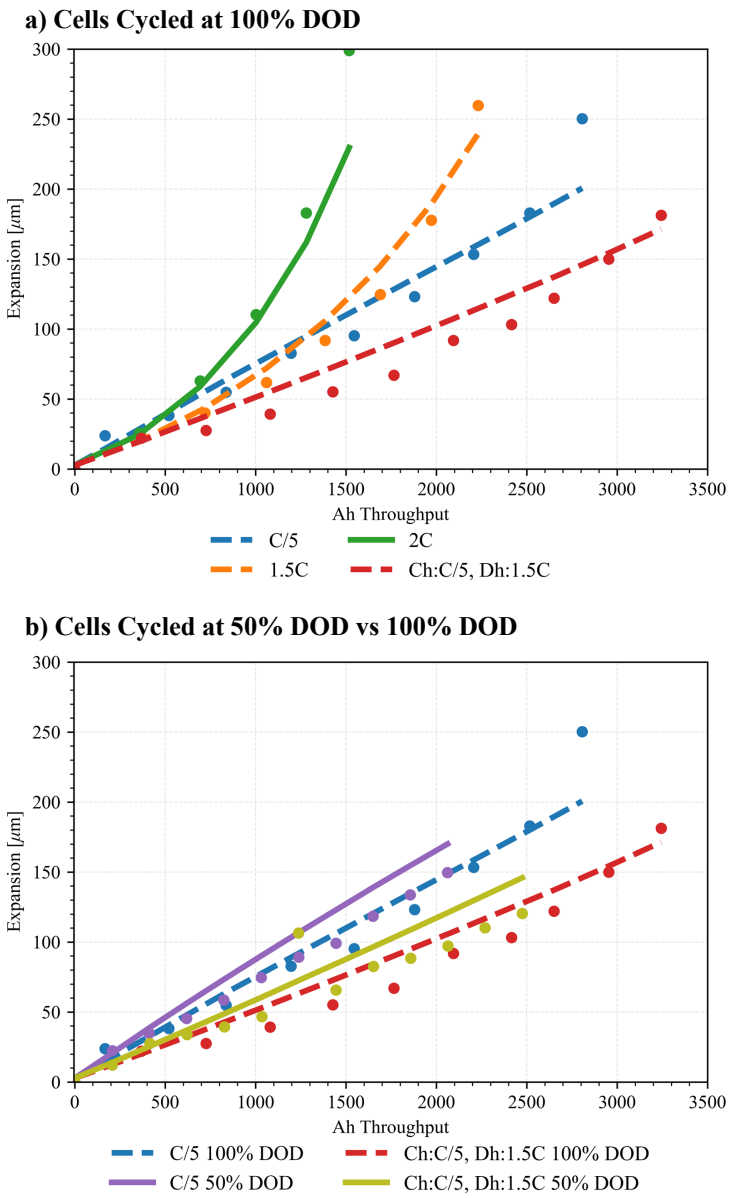


Figure 5.9: Irreversible Expansion Prediction for a) 100% DOD cells b) 50% DOD vs 100% DOD cells. Cell nominal capacity is 5 Ah and the cells were cycled at 25°C

. Data is shown as markers and the simulation is shown as lines. Dashed lines show the simulations on trained cells, and solid lines show predictions on untrained cells.

cells are cycling under higher SOC windows, resulting in lower SEI overpotentials, and thus larger SEI growth. Note that the current model has been tuned and thus predicts irreversible expansion when all cells have the same applied pressure. Applied pressure influences battery aging and irreversible expansion [1] and isn't explored in this work. Additional modeling is required to capture the effect of applied pressure.

5.4.6 Voltage and Total Expansion prediction for cycling at BOL, MOL, and EOL

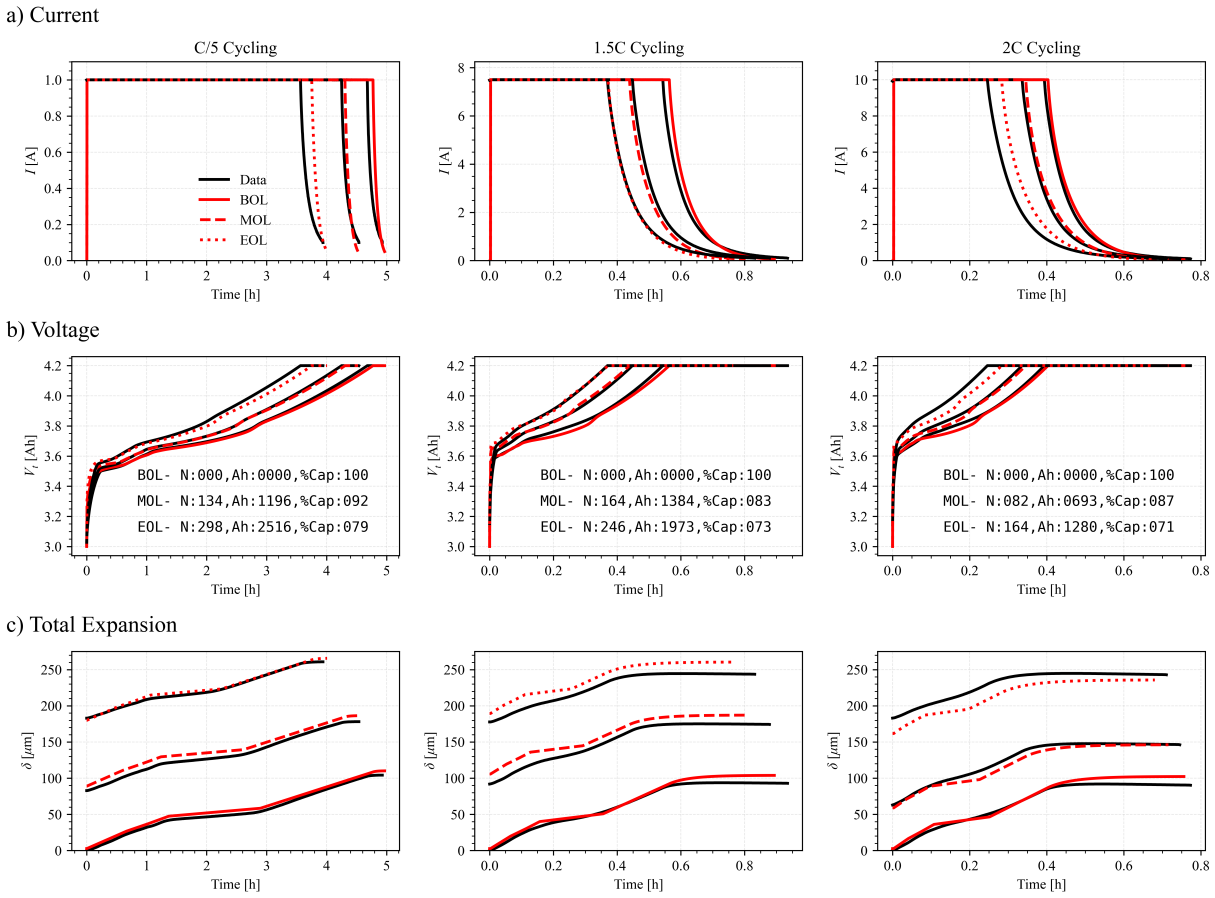


Figure 5.10: Cycling Current, Voltage and Expansion profile at BOL, MOL and EOL for C/5, 1.5C and 2C cycling aging. Data is shown in black, and the simulation is shown in red.

In this section, we show the cycling voltage and expansion prediction for cells cycled at C/5, 1.5C and 2C in Fig. 5.10. At C/5 model captures both the CC and CV phase for voltage and current well throughout life. But the voltage model error here increases as the cell ages from 22.7 mV at BOL to 37.2 mV at EOL. The main contribution to this error is capacity prediction at EOL. At 1.5 and 2C, data shows a longer CV phase whose duration increases as the cell ages, because of the higher overpotentials and higher resistance in an aged cell compared to a fresh cell. These overpotentials have a larger affect at higher C-rates compared to lower C-rates. The model captures both the CC and CV phase for voltage and current well throughout life for 1.5C. The good fit of the CV phases shows that we are capturing the overpotentials and resistance correctly in our model. The model error here increases as the cell ages from 19.9 mV at BOL to 22 mV at EOL. For 2C cycling aging,

the error is very high at EOL mainly because we underpredict capacity loss as discussed in Section 5.4.2.

In Fig. 5.10 c) we see that the model shows a good match with data for the expansion during cycling at different C-rates throughout life. The total expansion here shown here is a combination of reversible and irreversible expansion. Most of the model error comes from the mismatch in irreversible expansion prediction (previously discussed in Section 5.4.5), which determines the initial condition of the value of expansion at the start of the cycle. From the plot, we observe that the error in the prediction of reversible expansion is small.

5.4.7 Contribution of Degradation Mechanisms

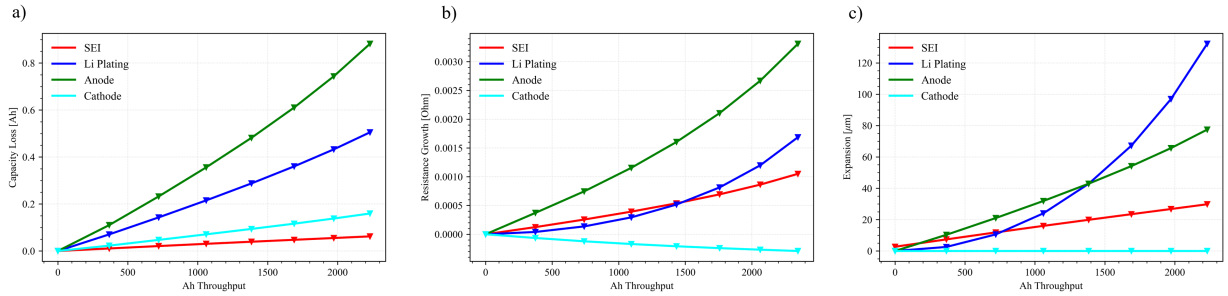


Figure 5.11: Contribution of degradation mechanisms (SEI growth, Li plating, Negative electrode damage, Positive electrode damage) to capacity loss, resistance growth, and irreversible expansion for cell cycled at 1.5C

The contribution of the individual degradation mechanisms (SEI growth, Li plating, Negative electrode damage, and Positive electrode damage) to capacity loss, resistance growth, and irreversible expansion for the cell cycled at 1.5C is shown in Fig. 5.11. The methodology to estimate these contributions is discussed in Section 6.3.3. From the figure, we observe that the negative electrode mechanical damage is the largest contributor to both capacity loss and expansion growth, followed by Lithum plating. Positive electrode mechanical damage and SEI growth only contribute a small amount to capacity loss. For the resistance growth, again negative electrode mechanical damage has the largest contribution. SEI growth and Li plating have similar contributions to resistance growth at EOL, with Li plating rising at quadratic rate. Finally for the irreverible expansion, Li plating contributes the most at EOL, followed by negative electrode mechanical damage and then SEI growth. SEI growth contributes to around 10% of all total irreversible expansion. While the capacity loss trend of Lithium plating is linear, the trend of resistance growth is quadratic and matches the large increase in resistance observed in data. We find a similar quadratic rate of irreversible expansion in data, but a linear proportionality of expansion growth to δ_{pl} gives us a linear

Table 5.2: List of Model Parameters and their values

Parameter	Symbol	Unit	Negative Electrode	Positive Electrode
Electrode Thickness	l	μm	62[33]	67[33]
Radius of particle	R_{p}	μm	10†	3.5[33]
Solid Diffusivity	D_s	m^2/s	8×10^{-14}†	8×10^{-15}[33]
Reaction Rate	k_0	$\frac{\mathrm{Am}^{-2}}{(\mathrm{m}^3\mathrm{mol})^{1.5}}$	3.18×10^{-6}†	3.38×10^{-6}†
Max conc. of Li	$c_{\mathrm{s,max}}$	$\mathrm{mol}/\mathrm{m}^3$	28746[33]	35380[33]
Charge transfer coeff.	α	-	0.5[33]	0.5[33]
Area of Electrode	A	m^2	0.205[33]	
Conc. of Li in electrolyte	c_{e}	$\mathrm{mol}/\mathrm{m}^3$	1000[33]	

$$U^-(x)[V] = 0.063 + 0.8\exp(-75 * (x + 0.007)) - 0.0120\tanh(\tfrac{x-0.127}{0.016}) - 0.0118\tanh(\tfrac{x-0.155}{0.016})0.0035\tanh(\tfrac{x-0.220}{0.020}) - 0.0095\tanh(\tfrac{x-0.190}{0.013}) - 0.0145\tanh(\tfrac{x-0.490}{0.020}) - 0.0800\tanh(\tfrac{x-1.030}{0.055})[33]$$

$$U^+(y)[V] = 4.3452 - 1.6518y + 1.6225(y^2) - 2.0843(y^3) + 3.5146(y^4) - 2.2166(y^5) - 0.5623\exp(109.451y - 100.006)[33]$$

$$\Delta\mathcal{V}^-(x)[-] = (x < 0.12)(0.2x) + (0.12 \leq x < 0.18)(0.16x + 5\mathrm{e}{-3}) + (0.18 \leq x < 0.24)(0.17x + 3\mathrm{E}{-3})[33]$$

$$\Delta\mathcal{V}^+p(y)[-] = -1.1\mathrm{E}{-2}(1 - y)[33]$$

† This thesis

rate. To achieve the quadratic rate as shown in the figure and in data, we assume a quadratic proportionality to thickness of plated lithium layer, that is δ_{pl}^2.

5.5 Model Parameters

A list of model electrochemical parameters of the cells used in our analysis and their values are given in Table 5.2. The model parameters are listed for SPM.

A list of degradation model parameters is given in Table 5.3. A list of tuned degradation model parameters is given in Table 5.4.

5.6 Conclusions

In this chapter, we present a model and framework for tuning using cycle life data that predict changes in battery performance, including voltage, resistance, capacity, and expansion due to battery aging. This is achieved by tracking the electrode-specific state of health parameters

Table 5.3: Degradation Model Parameters

Parameter	Symbol	Unit	Value
Charge transfer coefficient of SEI formation	α_{SEI}	-	0.5[3]
SEI Partial molar volume	Ω_{SEI}	m^3/mol	9.6×10^{-5}[3]
Charge transfer coefficient of Li plating	α_{Li}	-	0.65[64]
Li metal Partial molar volume	Ω_{pl}	m^3/mol	1.30×10^{-5}[64]
Potential of SEI formation	U_{SEI}	V	0.4[3]
Negative electrode Young's modulus	E^-	Pa	15×10^9[3]
Positive electrode Young's modulus	E^+	Pa	375×10^9[3]
Negative electrode critical stress	$\sigma^-_{\text{critical}}$	Pa	60×10^6[3]
Positive electrode critical stress	$\sigma^+_{\text{critical}}$	Pa	375×10^6[3]
Negative electrode Poisson's ratio	ν^-	-	0.2[3]
Positive electrode Poisson's ratio	ν^+	-	0.3[3]

Table 5.4: Tuned Degradation Model Parameters

Parameter	Symbol	Unit	Value
SEI kinetic rate constant	$k_{0,\text{SEI}}$	m/s	4.61×10^{-16}
SEI layer diffusivity	D_{SEI}	m^2/s	4.57×10^{-19}
SEI kinetic rate Arrhenius coefficient	$E_{a,\text{SEI}}$	J/mol	1.87×10^4
Li plating kinetic rate constant	$k_{0,\text{pl}}$	m/s	2.54×10^{-9}
Negative electrode LAM coefficient 1	$\beta^-_{\text{LAM},1}$	1/s	4.92×10^{-9}
Negative electrode LAM coefficient 2	$\beta^-_{\text{LAM},2}$	1/s	1.81×10^{-7}
Positive electrode LAM coefficient 1	$\beta^+_{\text{LAM},1}$	1/s	1.01×10^{-7}
Positive electrode LAM coefficient 2	$\beta^+_{\text{LAM},2}$	1/s	1.44×10^{-9}
LAM exponent	m_{LAM}	-	1.078
Ionic conductivity of SEI	κ_{SEI}	S/m	1/30000
Ionic conductivity of plated Li	κ_{pl}	S/m	1/30000
SEI expansion scaling factor	b_{SEI}	-	544
Li plating expansion scaling factor	b_{pl}	μm^{-1}	11004
Negative electrode expansion scaling factor	b^-_{in}	μm	413
Positive electrode expansion scaling factor	b^+_{in}	μm	0

or eSOH over life. Battery degradation was attributed to the mechanisms of SEI growth, Li plating, and mechanical damage using physics-based models. A sequential tuning procedure is adopted, where we first tune the SEI model using calendar aging data and then tune the Li plating and mechanical damage model using cycling aging data. C-rate dependency of battery aging was captured by using data from both high and low C-rates to tune the model. The tuned model is first used to predict capacity and resistance prediction under different C-rates and depth of discharges. The model captures the trend for most conditions

but underpredicts capacity loss at 2C. The trends for resistance growth were captured by including the contribution of lithium plating to battery resistance. Finally, we capture the voltage and expansion response across life for several C-rates and DODs for both symmetric and asymmetric cycling, showing that physics-based degradation models can be used to understand and predict changes in battery electrical and mechanical behavior, along with capacity loss, as the battery ages.

CHAPTER 6

Modeling Degradation at Multiple Pressures

6.1 Introduction

A physics-based model of the effect of pressure on battery aging will be presented in this chapter. In Chapter 4, we have created a physics-based battery model that can predict capacity loss, resistance growth, and battery expansion for various cycling conditions at room temperature (25°C). In this chapter, we extend the previously developed model to include the effect of pressure on battery aging.

We use the data first presented in [1] to develop and tune the model. These cells were cycled at a higher temperature of (45°C) and a high current of 2C charge and discharge at various pressures ranging from 0 kPa to 172 kPa. We analyze the data to get insights into which degradation mechanism is responsible for the effect of pressure on aging in Section 6.2. The model in Chapter 4 was tuned using only data at room temperature and hence needs to be re-tuned for the higher temperature data, which is discussed in Section 6.3. Then, we tune the degradation mechanism responsible for aging and predict aging at various pressures using the tuned model in Section 6.4. The model predictions are shown in Section 6.5. Finally, Section 6.6 summarizes the contributions.

6.2 Analyzing Degradation Data at Different Pressures

In this section, we analyze the degradation data to see how pressure affects capacity loss, resistance growth, and irreversible expansion. The purpose of the analysis is to determine the dependence of the degradation model on the applied pressure.

These cells were cycled at 45°C and at a current of 2C. The pressures these cells were cycled at are 0 kPa, 35 kPa, 69 kPa, 103 kPa, 138 kPa, and 172 kPa. In this section, we

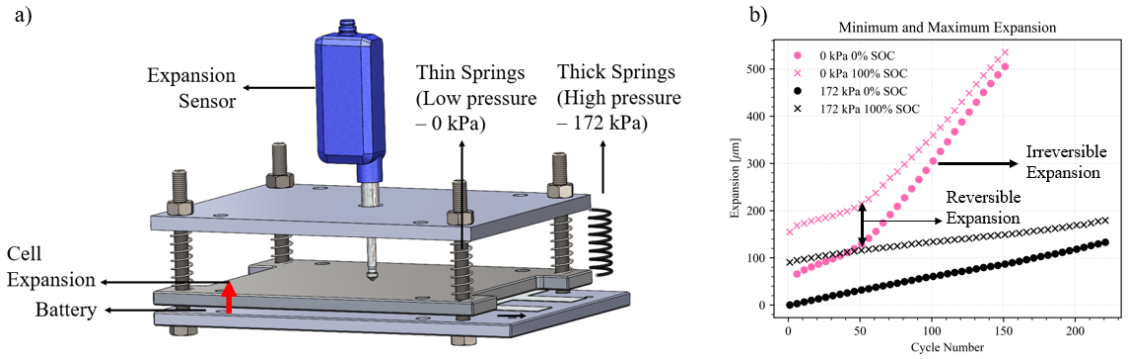


Figure 6.1: a) Battery fixture used to cycle cell and collect electrical and mechanical (expansion) data. Different springs were used to apply different pressures on the cell. b) Minimum and maximum battery expansion at each cycle under 0 kPa and 172 kPa, respectively. Minimum expansion occurs at the fully discharged state and is used as the value of irreversible expansion in this work. We also observe that the 0 kPa cell has a sharp increase in expansion due to gassing.

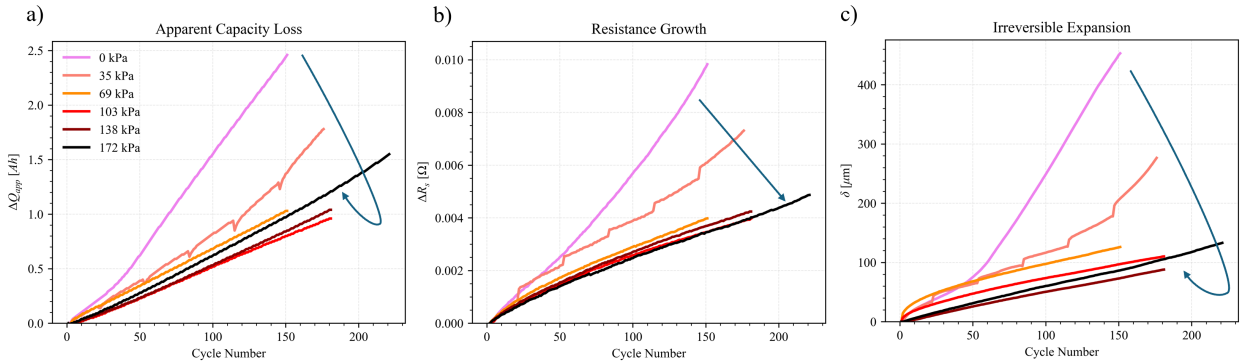


Figure 6.2: a) Apparent Capacity Loss, b) Resistance Growth and c) Irreversible Expansion for various pressures. 35 kPa cell has 25°C RPTs conducted at regular intervals, resulting in associated capacity recovery, high resistance growth, and irreversible during those tests.

first discuss the experimental procedure used to collect aging data at multiple pressures. After discussing the process used to collect data, we analyze how the cells age at different pressures by processing the degradation data and then using the analysis to determine the dependence of the degradation model on the applied pressure.

Compared to the cells used in the previous chapter, the cells cycled at higher pressures do not have reference performance tests (RPT) performed at regular intervals. This presents a challenge in analyzing degradation data from the continuous cycling data.

6.2.1 Experimental Procedure

The cells used to collect the pressure degradation data have the NMC111 and Graphite chemistry and are in pouch cell format. The cells were manufactured in the University of Michigan Battery Lab Pilot line and had a fresh cell capacity of 5 Ah. Further details about the battery specifications are given in [33]. Each cell was placed in a fixture with three plates, with the cell located between the bottom and the middle plate as shown in Fig. 6.1 a). Four springs were placed between the top and middle plate to apply uniform pressure on the middle plate and thus on the cell. Springs of different stiffness were used to apply different pressures on the cells. The middle plate is free to move and moves upwards when the cell expansion during cycling and due to aging. The linear variable differential transformer (LVDT) Keyence GT2-H12K expansion sensor with accuracy better than 1 μm captures the displacement of the middle plate and thus the expansion of the battery. The cells were placed in a Cincinnati Sub-Zero thermal chamber set to 45°C and cycled using a Biologic cycler at a current of 10 A (2 C-rate).

6.2.2 Apparent Cell Capacity

In this work, we analyze the apparent capacity loss instead of the thermodynamic or low C-rate capacity because of the absence of RPT data for these cells (except for 35 kPa). Apparent cell capacity is calculated by coulomb counting from 4.2V to 3V at a 2C discharge rate. Apparent capacity is lower than thermodynamic capacity because of voltage drop due to cell resistance. Apparent capacity loss vs cycle number for cells cycled at 45°C and at different pressures is shown in Fig. 6.2 a). We can see that initially, as the pressure increases, the capacity loss decreases, i.e., the capacity loss is highest at low pressures and lowest at high pressures. But, after 103 kPa, the capacity loss then increases for for the 138 kPa and 172 kPa cells. Hence, the capacity loss first decreases with pressure and then increases with the lowest capacity loss occurring at 103 kPa. The capacity loss for 15 and 138 kPa is very similar. The 35 kPa cell shows recovery of capacity at RPTs, resulting in dips in apparent capacity, as observed in the data.

6.2.3 Negative Electrode Capacity

LAM in the negative electrode is the dominant degradation mechanism as shown in Fig. 6.8. Estimation of negative electrode LAM is typically done by peak alignment or voltage fitting methods, but those methods do not work for high C-rate data. So, an alternative method using expansion data is derived in Appendix A.4. The estimated negative electrode capacity

for various pressures is shown in Fig. A.10. We observe that C_n loss decreases initially as the pressure decreases and then increases, similar to the trends observed in capacity loss. As with the capacity loss, lowest C_n loss occurs at 103 kPa. This means that we have higher LAM in negative electrode at lower pressures. This trend in C_n can help us inform impact of pressure on the mechanical damage model as discussed in Section 6.4. There is an outlier in the estimated C_n at 138 kPa, which will be further discussed in Appendix C. Thus, we don't consider the 138 kPa cell while tuning the pressure-dependent degradation mechanism.

6.2.4 Resistance

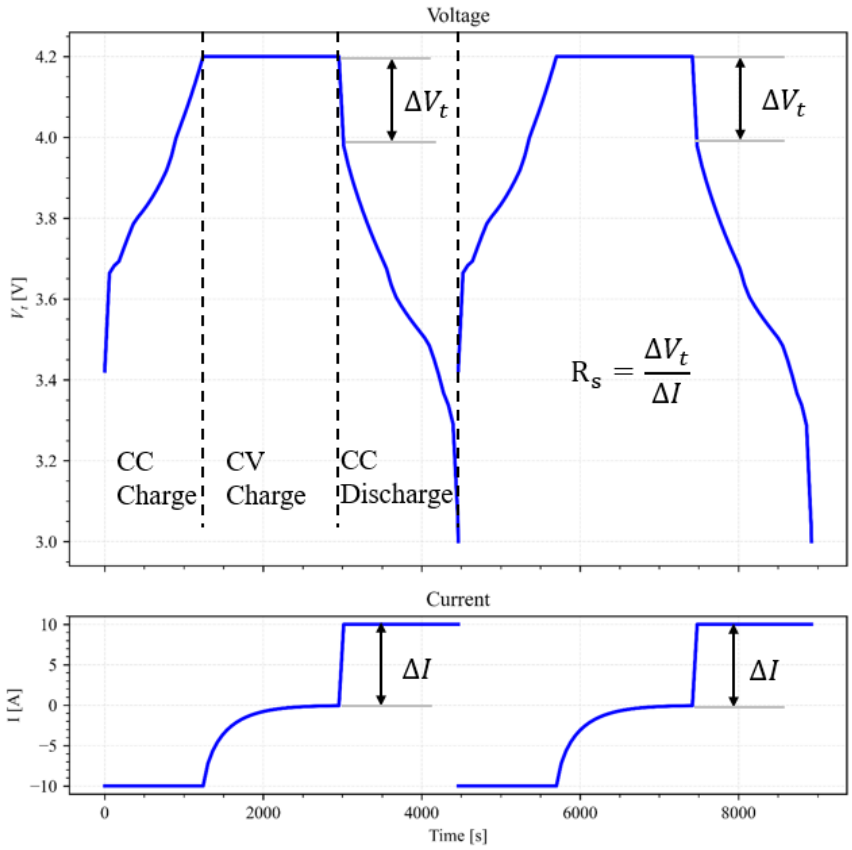


Figure 6.3: Resistance is estimated for each cycle at the start of discharge where current changes suddenly

Estimation of resistance growth is usually performed using HPPC tests that are part of RPTs. This presents a challenge for us since there are no reference performance tests performed for cells cycled at various pressures and thus we have no HPPC data. So, we have to utilize the continuous cycling data which is the only data present to estimate the

resistance growth. The DC resistance can be estimated when there is sudden change in current using:

$$R_s = \frac{\Delta V}{\Delta I} \tag{6.1}$$

Sudden changes in current occurs three times during continuous cycling: start of charge, start of discharge and end of discharge. Of these three events we cannot use start of charge and end of discharge since these occur at low SOCs where the slope of voltage curve is very high thus resulting in large resistance estimation errors. Thus, in this work we use the voltage and current signals at start of start of discharge to estimate DC resistance of the battery at that cycle as shown in Fig. 6.3 . We can further process the data to estimate resistance growth:

$$\Delta R = \frac{R_s - R_{s,0}}{R_{s,0}} \times 100 \tag{6.2}$$

where $R_{s,0}$ is the fresh cell resistance.

Resistance growth vs cycle number for cells cycled at $45°C$ and at different pressures is shown in Fig. 6.2 b). We can see that as the pressure increases, the resistance growth rate decreases. This means that resistance growth is highest at 0 kPa and is lowest at 172 kPa. Also, as the pressure increases, the resistance growth converges, with cells cycled at 0-172 kPa having similar resistance growth values. This trend is slightly different from the capacity loss trend, wherein the capacity loss first increased and then decreased with pressure. We also observe a high resistance growth during the RPT, resulting in the steps in resistance growth in the data.

6.2.5 Expansion

The irreversible expansion growth that occurs with aging is estimated using the battery expansion cycling data. The data for 0 kPa and 35 kPa cells is shown in Fig. 6.1 b). The figure shows minimum and maximum battery expansion at every cycle, with the minimum expansion occurring when the battery is fully discharged and the maximum expansion occurring when the battery is fully charged. In this work we will use the changes in the minimum cycling expansion as the irreversible expansion of the battery. The number is normalized for the fresh cell with the fresh cells having an expansion of 0 μm. We use the minimum expansion instead of maximum expansion because the maximum of the cells includes changes in both the irreversible expansion and reversible expansion of the cells and we are trying to analyze only the irreversible part of the expansion. In the figure, we also see that the 0 kPa

cell has a sharp increase in expansion after the beginning of life (BOL). This sharp increase in expansion isn't present in the 35 kPa, which indicate an abnormality at 0 kPa that occurs due to cells gassing. Gassing results in very high expansion values at 0 kPa of about 500 μm (12.5% strain) at end of life (EOL) compared to value of around 300 μm (7.5% strain) for the 35 kPa cells.

Irreversible expansion vs cycle number for cells cycled at $45°C$ and at different pressures is shown in Fig. 6.2 c). We can see that as the pressure increases, the expansion rate decreases initially and then increases, similar to the trends observed for capacity. Here the minimum expansion occurs at 138 kPa instead of the 103 kPa value where the minimum in capacity loss was observed. Also, similar to resistance, the values of expansion converge at higher pressures, i.e., the values of expansion at 103, 138, and 172 kPa have similar values.

6.3 Modeling Degradation at High Temperatures

In the previous chapter Chapter 5, we have discussed the degradation model and the method to tune the degradation model at room temperature (25°C). In this work, we adopt the same degradation model and mechanisms with updated SPM model parameters for a higher temperature (45°C) and then retune the model for the higher temperature, thus resulting a different set of degradation model parameters for 45°C compared to room temperature. The method of tuning for high temperature and the reasons for using a different set of degradation model parameters at high temperature is discussed in this section.

6.3.1 Tuning Degradation Model Parameters

1. SEI: Compared to room temperature, the contribution of SEI growth to battery aging is higher at 45°C. The trends in Loss of Lithium Inventory (LLI) in the model (which is SEI growth dominated) using the parameters tuned in Chapter 5 don't match the observed data at 45°C. One of the reasons for this is that the SEI parameters were tuned using calendar aging data in Chapter 5. Recently [74] has shown that there is boosted SEI growth during cycling compared to calendar aging, and this effect is more pronounced at 45°C where the SEI growth is higher compared to 25°C. Thus, in this work, instead of using calendar aging data to tune the SEI growth model, we use cycling aging data at a low C-rate (C/5).

2. Mechanical Damage and Li plating: The mechanical properties of the battery change as the temperature increases. In our mechanical damage model which uses particle stress, both the Young's modulus E and critical stress σ_{critical} decrease as the temperature

increases. As shown in Eqs. (4.30) and (4.31) E in the numerator of the mechanical damage equation and σ_{critical} is in the denominator. While we know that both these parameters decrease with increase in temperature, we don't know which parameter decreases more compared to the other. Thus, the parameters which we used at room temperature don't work at high temperatures since the ratio between E and σ_{critical} is different at higher temperature, resulting in a need to re-tune the parameters at $45°C$.

3. Resistance: If necessary, the conductivities of the SEI layer and the plated lithium layer κ_{SEI} and κ_{pl} need to retuned to match the resistance growth at higher temperatures. In this work, the values of κ_{SEI} and κ_{pl} tuned at room temperature work even at high temperature, so we don't need to re-tune these parameters.

4. Expansion: As discussed previously, since the mechanical properties of the battery are different higher temperature, we need to retune the the scaling factors in the expansion model: b_{SEI}, b_{pl}, b_{in}^{-} and b_{in}^{+}. These parameters are re-tuned using the same method in Chapter 5.

6.3.2 Results

Fig. 6.4 shows the eSOH simulation of cells used for training the degradation model parameters are discussed in the previous section. These cells are cycled at C/5, 2C and asymmetric C-rate (Ch: C/5 D:1.5C) respectively. We use the 2C cell here instead of 1.5C used in Chapter 5 because we need higher model accuracy at 2C which is the C-rate the cells cycled at different pressures were cycled at. As shown in the figure, the model shows a good agreement with the data for the trained cells.

Fig. 6.5 shows capacity, resistance growth and irreversible expansion for both the data and model for cells cycled at 45° C. The training cells simulation is shown in dotted lines while the prediction cell simulation is shown in solid lines. The data is shown as markers. The different colors show different cycling currents as shown in the figure legend. We see that there is good match between data and model for both the training and prediction cells at high temperatures.

The values of tuned degradation model parameters at room temperature, hot temperature and the ratio (hot/room) between them is shown in Table 6.1. For the SEI model we see that kinetic rate constant $k_{0,\text{SEI}}$ has a higher value, and SEI layer diffusivity has a lower value D_{SEI}. The lower value of D_{SEI} is necessary to capture the correct shape of capacity loss and LLI and the higher value of $k_{0,\text{SEI}}$ shows the boosted value at cycling aging compared to calendar aging. At hot temperature we observe a lower value of Li plating kinetic rate

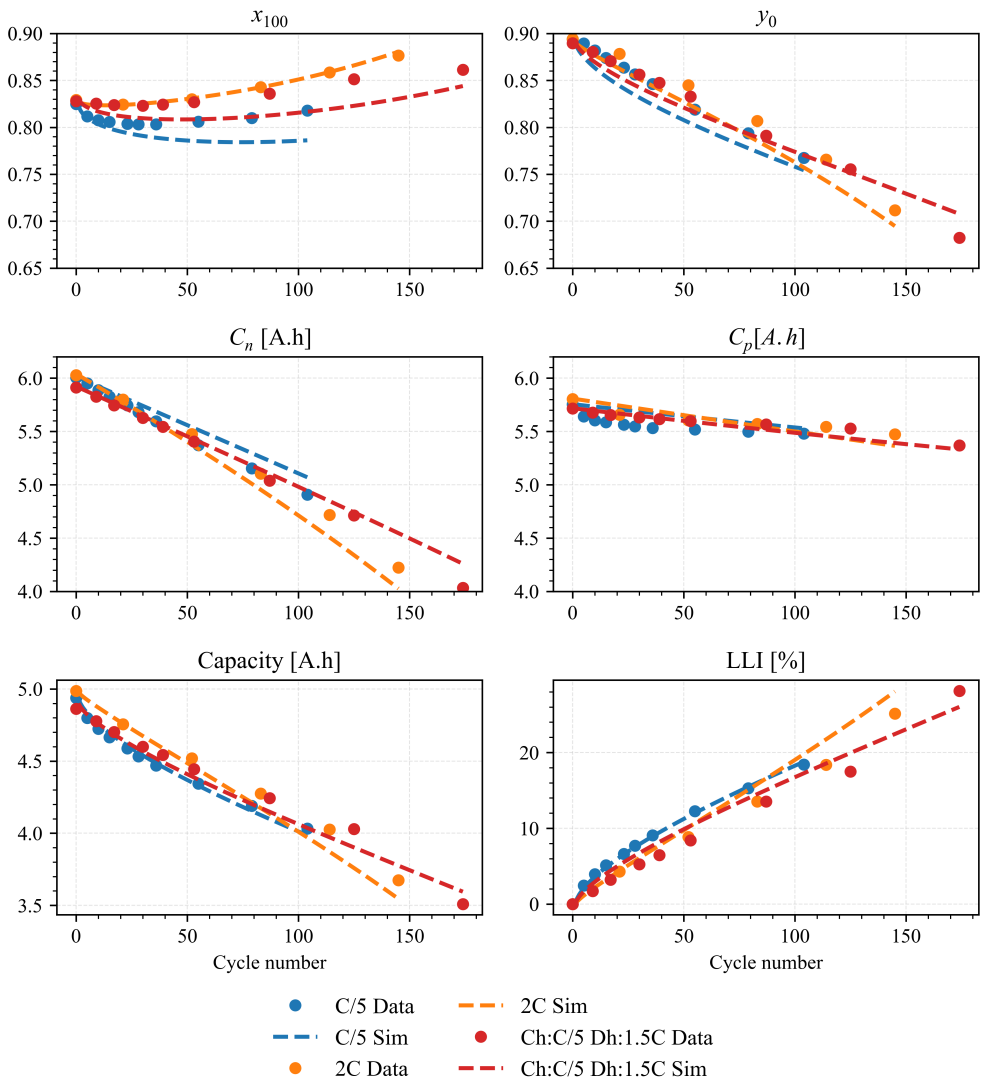


Figure 6.4: eSOH simulation and data for cells used for training degradation model parameters

constant $k_{0,\mathrm{pl}}$, which can be assumed as an Arrhenius temperature dependence of the rate constant. We observe higher values of both negative and positive electrode LAM coefficients at hot temperature compared to room temperature. The higher values of LAM coefficients are necessary to capture the higher values of C_n and C_p loss at high temperature and the lower values of stresses in the mechanical damage model. The lower value of stresses in the positive and negative electrode particles at high temperature are due to the lower values of diffusion at high temperatures.

The RMSE in Capacity, Resistance Growth and Expansion between data and model is shown in Table 6.2. For capacity, we have similar errors in both room and hot tempera-

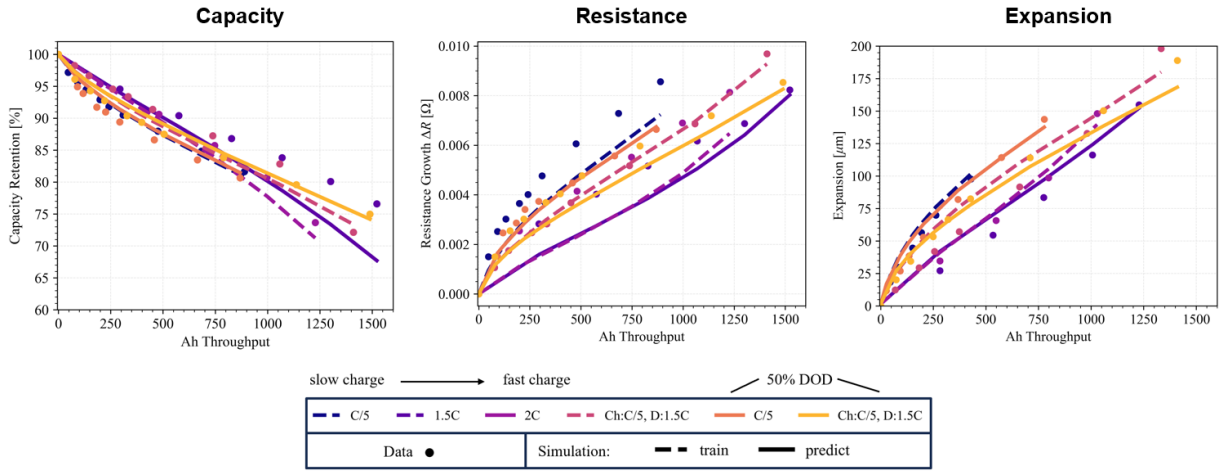


Figure 6.5: Capacity, Resistance and Expansion Simulation vs Data for cells cycled under various currents at Hot Temp ($45°C$)

Table 6.1: Tuned Degradation Model Parameters shown at room temperature, hot temperature

Parameter	Symbol	Unit	Room	Hot
SEI kinetic rate constant	$k_{0,\mathrm{SEI}}$	m/s	4.61×10^{-16}	5.49×10^{-14}
SEI layer diffusivity	D_{SEI}	m^2/s	4.57×10^{-19}	7.11×10^{-20}
SEI kinetic rate Arrhenius coeff.	$E_{a,\mathrm{SEI}}$	J/mol	1.87×10^{4}	1.87×10^{4}
Li plating kinetic rate constant	$k_{0,\mathrm{pl}}$	m/s	2.54×10^{-9}	7.33×10^{-10}
Negative electrode LAM coeff. 1	$\beta^{-}_{\mathrm{LAM},1}$	1/s	4.92×10^{-9}	8.76×10^{-6}
Negative electrode LAM coeff. 2	$\beta^{-}_{\mathrm{LAM},2}$	1/s	1.81×10^{-7}	1.5×10^{-6}
Positive electrode LAM coeff. 1	$\beta^{+}_{\mathrm{LAM},1}$	1/s	1.01×10^{-7}	6.84×10^{-8}
Positive electrode LAM coeff. 2	$\beta^{+}_{\mathrm{LAM},2}$	1/s	1.44×10^{-9}	9.7×10^{-9}
LAM exponent	m_{LAM}	-	1.078	1.0005
Ionic conductivity of SEI	κ_{SEI}	S/m	1/30000	1/30000
Ionic conductivity of plated Li	κ_{pl}	S/m	1/30000	1/30000
SEI expansion scaling factor	b_{SEI}	-	544	296
Li plating expansion scaling factor	b_{pl}	μm^{-1}	11004	9608263
Neg electrode expansion scaling	b^{-}_{in}	μm	413	477
Pos electrode expansion scaling	b^{+}_{in}	μm	0	0

ture. Meanwhile, for resistance growth, hot temperature has much higher error for most conditions compared to room temperature showing deterioration of model performance at hot temperature. Lastly for expansion, we see that the errors are lower at hot compared to room temperature.

Table 6.2: Comparison of RMSE in Capacity, Resistance Growth and Expansion. Expansion in μm is converted to strain by dividing with the cell thickness of 4000μm. Thus an error of 0.5% corresponds to 20μm

	Capacity [%]		Resistance Growth [%]		Expansion (Strain [%])	
Cycling Condition	Room	Hot	Room	Hot	Room	Hot
C/5	1.45	0.6	10.2	22.9	0.45	0.16
1.5C	1.57	4.82	3.4	21.9	0.31	0.27
2C	4.2	1.76	7.8	22.6	0.74	0.16
Ch:C/5 D:1.5C	1.77	0.74	9.8	6.2	0.36	0.39
C/5 50-100% SOC	0.68	2.34	4.8	11.8	0.39	0.19
Ch:C/5 D:1.5C 50-100% SOC	1.9	2.41	6.7	19.2	0.45	0.22

6.3.3 Contribution of Degradation Mechanisms to Capacity Loss, Resistance Growth and Irreversible Expansion

In this section, we will discuss the contribution of each degradation mechanism to capacity loss, resistance growth and irreversible expansion and the methodology used to calculate the contributions from aging simulations. Then, we analyze the contributions to determine which mechanism is dominant and might be pressure-dependent.

6.3.3.1 Capacity Loss

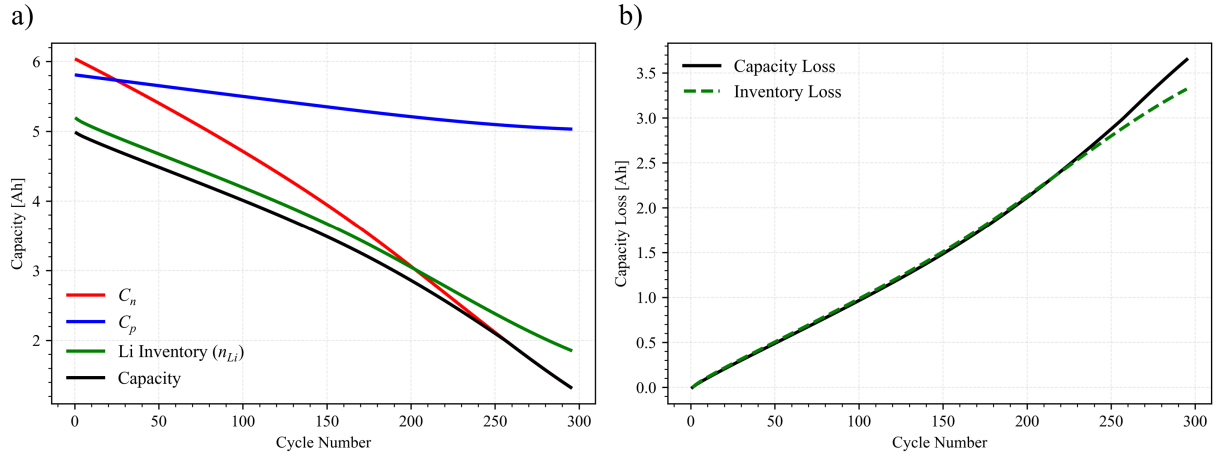


Figure 6.6: a) Modeled Negative electrode capacity, positive electrode capacity, lithium inventory (moles of cyclable lithium) and the battery capacity for a cell cycled at 2C and at 45°C b) Capacity loss and inventory loss

Fig. 6.6 a) shows negative electrode capacity, positive electrode capacity, lithium inventory (moles of cyclable lithium), and the battery capacity for a cell cycled at 2C and at $45°C$. Fig. 6.6 b) shows the capacity loss and inventory loss for the same cell. We can observe that until the negative electrode capacity line crosses the inventory line, the capacity loss and inventory loss are the same. This means that the cell is lithium inventory limited. After that, the cell capacity tracks the negative electrode capacity, making the cell negative electrode capacity limited.

Now we discuss how to calculate the contribution of degradation mechanisms to capacity loss. For SEI and Li plating, the capacity loss in the Ah is equivalent of lithium loss due to the side reactions.

$$\Delta C_{\text{SEI}} = \Delta n_{\text{Li,SEI}} \frac{F}{3600} \tag{6.3}$$

$$\Delta C_{\text{pl}} = \Delta n_{\text{Li,pl}} \frac{F}{3600} \tag{6.4}$$

$$\tag{6.5}$$

In the simulated case with an N:P ratio of 1.2, we see that the cell is inventory-limited before 40% capacity loss. When the cell is inventory-limited, we can say that:

$$\Delta n_{\text{Li}} = \Delta C \tag{6.6}$$

Also, total lithium loss is sum of lithium loss from each mechanism:

$$\Delta n_{\text{Li}} = \Delta n_{\text{Li,SEI}} + \Delta n_{\text{Li,pl}} + \Delta n_{\text{Li,mech}} \tag{6.7}$$

giving us:

$$\Delta n_{\text{Li,mech}} = \Delta n_{\text{Li}} - \Delta n_{\text{Li,SEI}} - \Delta n_{\text{Li,pl}} \tag{6.8}$$

We can approximate the contribution of negative electrode and positive electrode to the lithium loss by splitting the lithium loss due to mechanical damage using the ratio between negative electrode and positive electrode capacity loss.

$$\Delta n^{-}_{\text{Li,mech}} = \frac{\Delta C_{\text{n}}}{\Delta C_{\text{n}} + \Delta C_{\text{p}}} \Delta n_{\text{Li,mech}} \tag{6.9}$$

$$\Delta n^{+}_{\text{Li,mech}} = \frac{\Delta C_{\text{p}}}{\Delta C_{\text{n}} + \Delta C_{\text{p}}} \Delta n_{\text{Li,mech}} \tag{6.10}$$

We can then convert the individual electrode lithium loss to capacity loss:

$$\Delta C^{-}_{\text{mech}} = \Delta n^{-}_{\text{Li,mech}} \frac{F}{3600} \tag{6.11}$$

$$\Delta C^{+}_{\text{mech}} = \Delta n^{+}_{\text{Li,mech}} \frac{F}{3600} \tag{6.12}$$

6.3.3.2 Resistance Growth

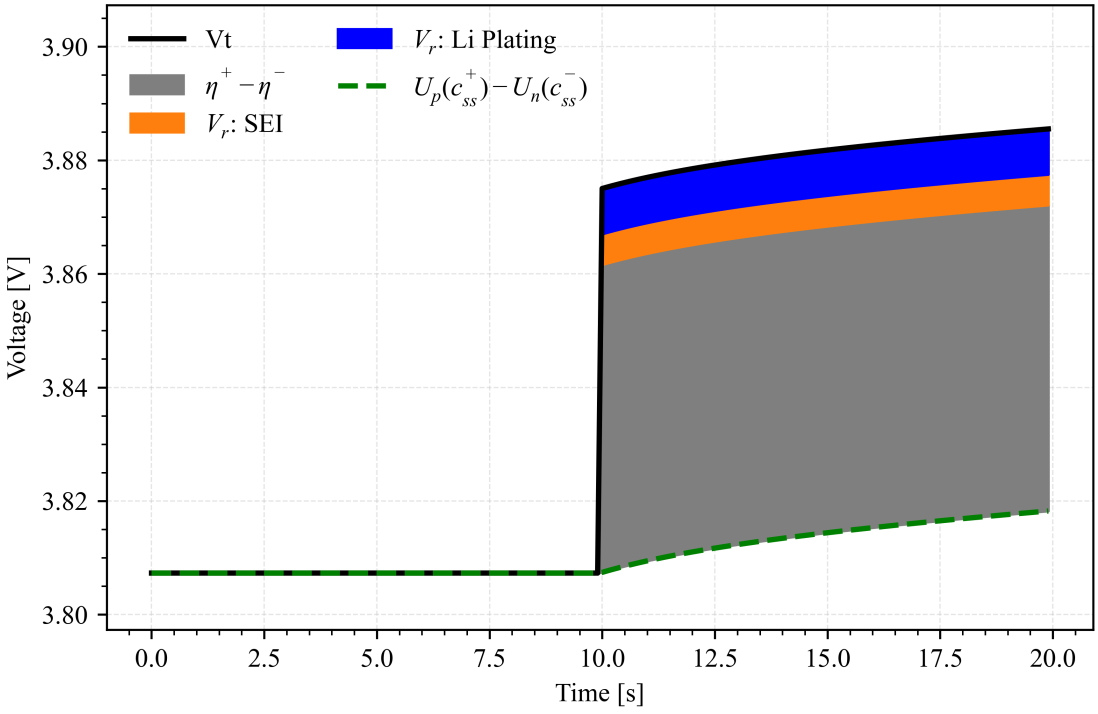


Figure 6.7: Components of voltage of an aged cell at 50% SOC during a pulse. These voltage components are used to calculate resistance growth due to each degradation mechanism

Fig. 6.7 shows the components of voltage during a 10 second pulse. The cell is at 65% capacity and the resting SOC is 50%. We can see the contribution of voltage change due to overpotential $\eta^+ - \eta^-$ (grey), SEI growth $V_{\text{r,SEI}}$ (yellow) and lithium plating $V_{\text{r,pl}}$ (blue). Similar to the method in Section 6.3.3.2 we can calculate resistance due to each component

using Eq. (6.1) just before and after the current change:

$$R_{\text{SEI}} = \frac{\Delta V_{\text{r,SEI}}}{\Delta I} \tag{6.13}$$

$$R_{\text{pl}} = \frac{\Delta V_{\text{r,pl}}}{\Delta I} \tag{6.14}$$

$$R^{-}_{\text{mech}} = \frac{\Delta \eta^{-}}{\Delta I} \tag{6.15}$$

$$R^{+}_{\text{mech}} = \frac{\Delta \eta^{+}}{\Delta I} \tag{6.16}$$

We can further process the data to estimate resistance growth:

$$\Delta R_{\text{SEI}} = R_{\text{SEI}} - R_{\text{SEI,0}} \tag{6.17}$$

$$\Delta R_{\text{pl}} = R_{\text{pl}} - R_{\text{pl,0}} \tag{6.18}$$

$$\Delta R^{-}_{\text{mech}} = R^{-}_{\text{mech}} - R^{-}_{\text{mech,0}} \tag{6.19}$$

$$\Delta R^{+}_{\text{mech}} = R^{+}_{\text{mech}} - R^{+}_{\text{mech,0}} \tag{6.20}$$

where $R_{\text{SEI,0}}, R_{\text{pl,0}}, \Delta R^{+}_{\text{mech}}, \Delta R^{+}_{\text{mech}}$ are the resistance values of each component for a fresh cell.

6.3.3.3 Expansion

The contribution of each degradation mechanism to irreversible expansion can be calculated by splitting Eq. (4.47) into individual components. This results in:

$$\delta_{\text{irrev,SEI}} = b_{\text{SEI}} \delta_{\text{SEI}} \tag{6.21}$$

$$\delta_{\text{irrev,pl}} = b_{\text{pl}} \delta_{\text{pl}} \tag{6.22}$$

$$\delta^{-}_{\text{irrev,mech}} = b^{-}_{\text{in}} \Delta \varepsilon^{-}_{\text{s}} \tag{6.23}$$

$$\delta^{+}_{\text{irrev,mech}} = b^{+}_{\text{in}} \Delta \varepsilon^{+}_{\text{s}} \tag{6.24}$$

6.3.4 Analysis

The contribution of the individual degradation mechanisms (SEI growth, Li plating, Negative electrode damage, Positive electrode damage) to capacity loss, resistance growth, and irreversible expansion at the nominal pressure of 35 kPa is shown in Fig. 6.8. From the figure, we observe that the negative electrode mechanical damage is the largest contributor to both capacity loss and expansion growth. For the resistance growth, both SEI growth and negative

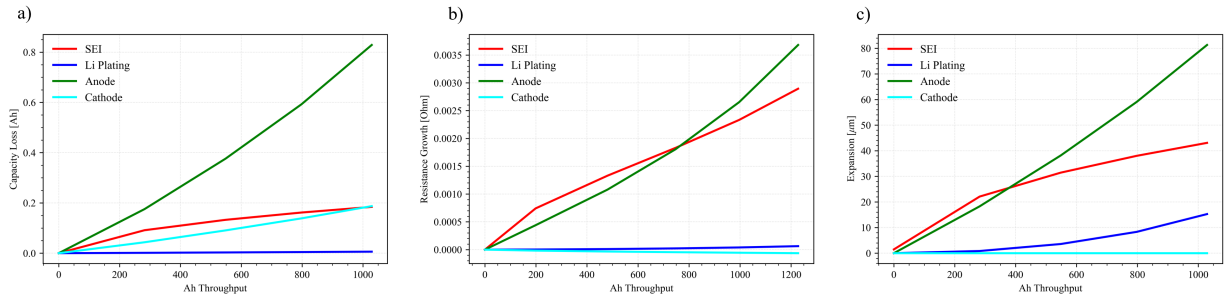


Figure 6.8: Contribution of degradation mechanisms (SEI growth, Li plating, Negative electrode damage, Positive electrode damage) to capacity loss, resistance growth and irreversible expansion at 35 kPa

electrode damage have similar contributions. The contribution of SEI growth to capacity loss is around one-fourth of the negative electrode damage and to expansion growth is around one-half. Hence, the negative electrode damage is the dominant degradation mechanism in the cells at 35 kPa.

6.4 Mechanical Damage Model: Impact of Pressure

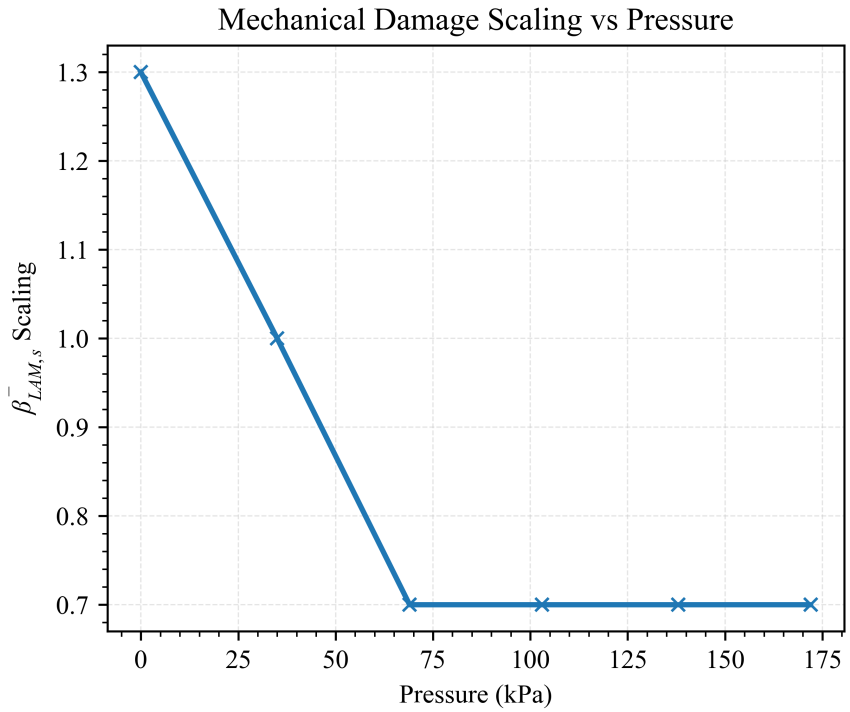


Figure 6.9: Negative Electrode Mechanical Damage Coefficient (Scaled) $\beta^-_{\mathrm{LAM},s}$ vs Pressure

In Section 6.2 we've seen that there is an impact of pressure on C_n and thus the LAM in the negative electrode. This impact can be modeled as different $\beta^-_{\text{LAM1,2}}$ parameters in the mechanical damage model for different pressures:

$$\frac{d\varepsilon_s^-}{dt} = \beta^-_{\text{LAM},s}(P)\left(-\beta^-_{\text{LAM},1}\left(\frac{|\sigma_{\max}|}{\sigma_{\text{critical}}}\right)^{m_{\text{LAM}}} - \beta^-_{\text{LAM},2}\left(\frac{|\sigma_{\min}|}{\sigma_{\text{critical}}}\right)^{m_{\text{LAM}}}\right) \tag{6.25}$$

equate this to LAM

Thus, we can tune the $\beta^-_{\text{LAM},s}(P)$ values in the model to match the LAM in the negative electrode. Fig. 6.9 shows the scaled value of β^-_{LAM} plotted versus applied pressure. The scaled value of $\beta^-_{\text{LAM},s}$ is the ratio of β^-_{LAM} divided by its value at the reference pressure of 35 kPa. As shown in the figure, the value of β^-_{LAM} is inversely proportional to the applied pressure. This means that higher the applied pressure, lower the mechanical damage in the negative electrode, thus lower capacity loss. This is valid until 69 kPa, after which the mechanical damage in the negative electrode doesn't change further with an increase in pressure. The dependence of $\beta^-_{\text{LAM},s}$ on pressure arises because the battery's mechanical properties depend on applied pressure. Applying more pressure changes the stiffness of the porous electrodes and, thus, the stresses in the electrodes [50]. Since we don't capture the change in mechanical properties in the stress model, the difference is pushed to the β^-_{LAM} parameter, which is now dependent on pressure.

We have seen how different values of β^-_{LAM} at different pressures affect C_n and thus capacity loss. But what about resistance to growth and expansion? In our model, C_n affects both resistance through the below equations:

$$R_s = R_{\text{film}} + R_{\text{LAM}} \tag{6.26}$$

$$R_{\text{LAM}} = \frac{r_p^-}{6l^- A i_0^- \varepsilon_s^-} + \frac{r_p^+}{6l^+ A i_0^+ \varepsilon_s^+} \tag{6.27}$$

where R_s is DC resistance of the cell, R_{film} is the film resistance from SEI and Li plating, R_{LAM} is resistance due to LAM, r_p is radius of particle, A is area of electrode, l^- is thickness of electrode, i_0 is exchange current density.

As shown in Eq. (A.2), ε_s^- is directly proportional to C_n. High C_n loss indicates a low ε_s^- resulting in a high R_{LAM} and thus a high R_s. Thus, different C_n loss rates results in different resistance growth rates. So, having different values of $\beta^-_{\text{LAM},s}(P)$ at different pressures results in different values of resistance growth.

Similarly for the irreversible expansion of the battery is given by Eq. (4.47). Different values of $\frac{d\varepsilon_s^-}{dt}$ for different pressures result in different values of $\Delta\varepsilon^-_{\text{in}}$ and thus different values

of δ_{irrev}, resulting in dependence of expansion on pressure.

Thus, having pressure-dependent parameters of $\beta^{-}_{\text{LAM},s}(P)$ results in pressure-dependent rates of capacity loss, resistance growth, and irreversible expansion.

6.5 Results

In this section, we simulate pressure-dependent cell aging by having $\beta^{-}_{\text{LAM},s}(P)$ as a function of pressure in the degradation model and then keeping the rest of the parameters the same. We then compare the simulations with the data to see if the pressure-dependent mechanical model captures the observed capacity loss, resistance growth, and irreversible expansion. The values of $\beta^{-}_{\text{LAM},s}(P)$ at different pressures are shown in Fig. 6.9.

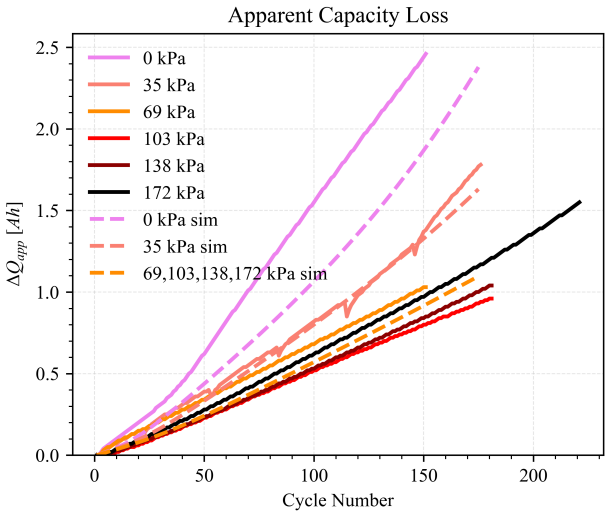


Figure 6.10: Capacity Simulation (Apparent Capacity Loss) for various pressures plotted against data

Table 6.3: Comparison of RMSE in Capacity, Resistance Growth, and Expansion for cells cycled at various pressures.

Pressure (kPa)	Capacity [Ah]	Resistance Growth [$m\Omega$]	Expansion [μm]
0	0.4	2.5	118
35	0.05	0.85	22
69	0.1	0.28	14
103	0.07	0.75	23
138	0.04	0.85	42
172	0.05	0.8	32

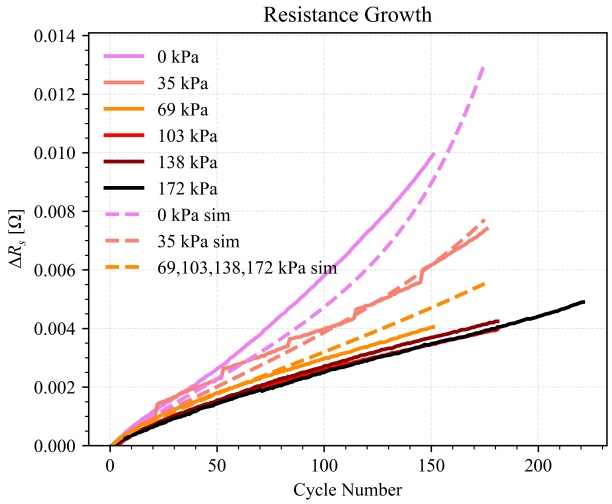


Figure 6.11: Resistance Simulation (Resistance growth) for various pressures plotted against data

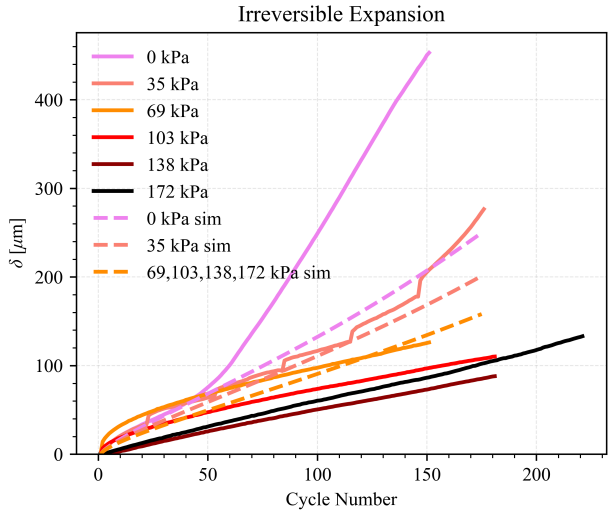


Figure 6.12: Expansion Simulation (Irreversible expansion) for various pressures plotted against data

6.5.1 Capacity

Fig. 6.10 shows the capacity loss in Ah for both the model and the data. We observe that the model matches the trends in the data well. As the pressure increases, we see a decrease in capacity loss. The RMSE between model and data is shown in Table 6.3. The model underpredicts the capacity loss at 0 kPa, leading to a high value of RMSE. At the pressures of 69-172 kPa, the model predicts the same value of the capacity loss since the $\beta^{-}_{\text{LAM},s}(P)$ values are the same at those pressures. The RMSE values of capacity loss at those pressures,

range between 0.04-0.1 Ah, showing that our model has good prediction at higher pressures.

Initially, an increase in applied pressure results in a decrease in capacity loss. This is probably because of better contact between particles and binder thus better transport of lithium ions. But, at higher pressures, the porosity of the electrodes is lower, which causes a decrease in transport and thus results in higher overpotentials. Higher overpotentials result in higher side reaction currents and, thus, higher capacity loss.

6.5.2 Resistance

Fig. 6.11 shows the resistance growth in Ohms for both the model and the data. We see a decrease in resistance growth as the pressure increases in both the data and model, showing that the model matches the trends in the data. The RMSE between the model and data is shown in Table 6.3. As with the capacity loss, the error is higher at 0 kPa pressure cell, with the model showing a sharp increase in resistance after MOL, which isn't observed in the data. The RMSE of resistance prediction is lowest at 69 kPa with a value of 0.28 $m\Omega$ and then increases at higher pressures. In the model, the resistance has the same values for at the pressures of 103-172 kPa, which matches the trends in the data and can also be seen in the RMSE values having similar values of 0.75-0.85 $m\Omega$.

6.5.3 Expansion

Fig. 6.12 shows the irreversible expansion in micrometers for both the model and the data. As with capacity loss and resistance growth, we see a decrease in irreversible expansion as the pressure increases which our model captures. The RMSE between model and data is shown in Table 6.3. The RMSE is very high for 0 kPa where the data shows a sharp increase in irreversible expansion before MOL which our model doesn't capture. This is possibly due to gassing in the battery which has a higher chance to occur at lower pressures. Gassing causes the battery to swell since in its a pouch cell, thus resulting a sharp increase in battery thickness beyond 300 μm. This phenomenon isn't observed at other pressures, including 35 kPa, showing that only the 0 kPa cell swelled. Gassing isn't modeled in this work and thus isn't captured by our model. The error is low at the pressures of 35-103 kPa and increases slightly at higher pressures of 138 and 172 kPa. This is because the battery thickness is lower as we increase the pressure since the porous components of the battery get compressed more. Since the battery thickness is lower, the irreversible expansion is proportionally lower. Capturing the decrease in battery thickness due to applied pressure (which we don't model in this thesis) can help us capture dependence of irreversible expansion at higher pressure.

6.5.4 Contribution of Degradation Mechanisms

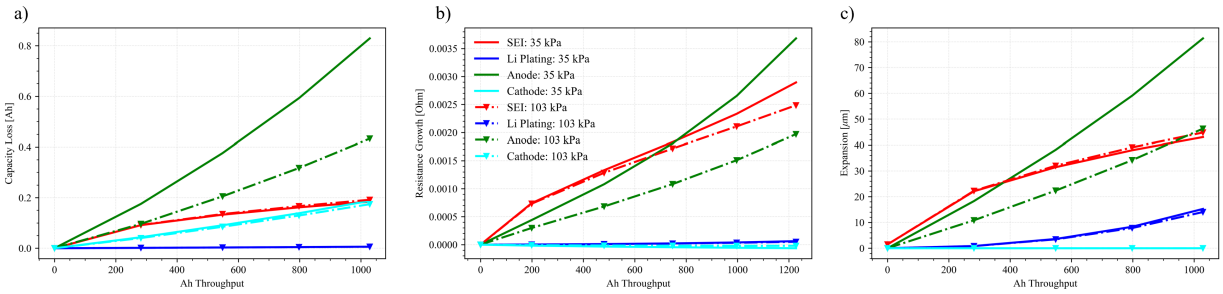


Figure 6.13: Impact of Pressure on contribution of degradation mechanisms to capacity loss, resistance growth and irreversible expansion

The impact of Pressure on the contribution of degradation mechanisms to capacity loss, resistance growth, and irreversible expansion is shown in Fig. 6.13. Negative electrode damage is the largest contributor to capacity loss and expansion at lower pressure (35 kPa). Both SEI growth and negative electrode damage have similar contributions to resistance growth. However, at higher pressure, the SEI growth contribution to resistance growth is higher compared to negative electrode damage, but the contribution to expansion growth is similar. The resistance growth due to SEI growth mechanism has a $\sqrt{t}$ shape. Higher contribution of SEI growth to resistance at higher pressures leads to the resistance growth curve also taking the $\sqrt{t}$ shape as shown in Fig. 6.2 b). Also, the contribution of SEI growth to capacity loss is one-half of the negative electrode damage as opposed to one-fourth at lower pressures.

6.6 Conclusion

In this chapter, we model the impact of externally applied pressure on battery aging. This is achieved by first analyzing the degradation data for cells cycled at higher pressures, including apparent capacity loss, resistance growth, irreversible expansion, and negative electrode capacity loss to determine which degradation mechanism is responsible for dependence of degradation on applied pressure. Then, we retune the model fitted previously to room temperature data to predict aging at higher temperature at which the cells at various pressures were cycled in. Negative electrode mechanical damage was found to be the aging mechanism which was dependent on pressure. We then tune the negative electrode mechanical damage mechanism to the negative electrode capacity loss. The tuned degradation model predicts the trends in capacity loss, resistance growth, and irreversible expansion found in the data. Also, the error between the model and data is low for various pressures.

CHAPTER 7

Conclusions and Future Work

This thesis presents a framework for modeling and tuning physics-based battery degradation models that can predict capacity loss, resistance growth, and expansion throughout its life. It was found that additional state of health (SOH) metrics, such as electrode state of health (eSOH) and battery expansion, can be leveraged to tune the parameters in a battery degradation model by understanding their connection to the underlying mechanisms. Extra information from battery expansion can help improve battery lithiation state estimation and also eSOH estimation under higher currents. The proposed model links battery degradation mechanisms such as SEI growth, Lithium plating, and Mechanical damage to capacity loss, resistance growth, and irreversible expansion. Accelerated aging simulations were utilized to enable the tuning of degradation mechanism parameters using degradation data from experimental aging studies. The tuning results in a single set of parameters that predicts all three SOH variables: capacity, resistance, and expansion throughout the battery lifetime for cells cycled under various current rates and SOC windows, even for cycling conditions not used for tuning. To design and operate battery storage systems safely, we must be able to predict and detect changes in all three SOH metrics over life accurately. Finally, we extend the model to predict the impact of externally applied pressure on battery degradation.

7.1 Summary of Contributions

The main contribution of this thesis is to model and predict battery irreversible expansion by linking it to battery degradation.

In Chapter 2, we developed a new sensor, called inductive displacement sensor (IDS), that uses the principle of mutual inductance to measure battery expansion. The sensor measurement is designed to be linearly proportional to displacement in the range of 10-500 μm at multiple temperatures. The sensor performs similarly to LVDT sensors, which are two orders of magnitude costlier. Thus, the sensor will enable scaling to multiple channels of

battery expansion at a low cost necessary for using expansion to model battery degradation.

In Chapter 3, we described the single particle model (SPM) that forms the framework of the degradation model. The electrode concentration (lithiation) states in the SPM were linked to the observed battery expansion. Particle stress and strain, which are functions of electrode concentration, were linked to particle expansion and, finally, cell expansion.

In Chapter 4, we modeled battery degradation in a Single Particle Model (SPM) framework with SEI growth and Lithium plating as side reactions, which resulted in loss of lithium inventory (LLI) and with mechanical damage as an additional mechanism, which resulted in loss of active material (LAM). We introduced an equivalent stress and concentration dependence of stress to the mechanical damage model. Commonly used fatigue models assume symmetric cycles (zero-mean stress). An equivalent stress that adjusts for non-zero mean stress was needed to account for cycling conditions with different currents on charge and discharge. The concentration dependency of strain and the resulting stress allowed us to capture different degradation rates for cells cycled at different depths of discharge (DOD). Lithium plating at the separator interface is often described as a spatially non-uniform process using the pseudo-2D (P2D) model. This phenomenon can be captured in the SPM framework using a current-dependent dynamic term to account for spatial-nonuniformity of electrolyte dynamics at higher currents. Finally, we related observed irreversible expansion to SEI growth, mechanical damage, and Li Plating variables using a linear relationship (quadratic in the case of Li plating).

In Chapter 5, we utilized experimental data from cells cycling with periodic reference performance tests to tune the degradation model. In addition to the standard I, V, and T measurements, continuous measurements of the thickness change of the battery pouch cells were recorded. We extracted the capacity, electrode state of health (eSOH), resistance, and reversible and irreversible expansion from this data. The test conditions were designed to excite different dominant degradation mechanisms (e.g., mechanical damage) by cycling the cells at different conditions (C-rate, temperature, preload pressure, and DOD). The tuning was performed in sequential steps. First, the parameters related to the electrochemical and mechanical degradation rates, which result in LLI and LAM, were tuned to match the extracted eSOH variables at each Reference Performance Test (RPT). This tuning gives us the amount of plated Li, SEI growth, and mechanical damage in the particles. Next, we tuned additional resistance and expansion model parameters to relate these quantities to observed resistance growth and irreversible expansion. The tuning, which uses accelerated aging simulations (to speed up the tuning process), results in a single set of parameters that predicts capacity loss, resistance growth, and irreversible thickness change as the battery ages, even for conditions that were not used for parameter tuning.

In Chapter 6, we extended the previously developed degradation model to include the impact of externally applied pressure. First, we developed ways to analyze aging metrics of cells cycled under various pressures from cycling data, including resistance growth and irreversible expansion, which are usually estimated using characterization tests. Cells cycled under various pressures were tested at a different temperature than those used previously to tune the degradation model. Hence, we re-tune the model to predict aging at this new temperature. Then, we introduce the dependency of pressure in the degradation mechanisms and finally predict the impact of pressure on capacity loss, resistance growth, and irreversible expansion.

In Appendix A, we discuss the methodology to estimate eSOH parameters, which were essential in the tuning process of the degradation model. First, we discuss eSOH estimation using voltage fitting method. Then, we explore the limitations of the eSOH estimation method and develop a scheme for updating eSOH parameters in a BMS using data screening. Finally, we introduce a new method of estimating eSOH parameters using expansion data, which works at higher currents, unlike the voltage-fitting method.

In Appendix B, we developed a state observer for a physics-based single-particle Li-ion battery model by augmenting the voltage and expansion measurements. Accurate estimation of negative solid-surface concentration from the state observer can enable more robust constraints on the state during charging and prevent degradation mechanisms like lithium plating during high C-rates.

7.2 Future Work

This work shows the ability of physics-based battery models to predict various state of health metrics that include irreversible expansion, resistance growth, and irreversible expansion. This work highlights the ability of battery expansion to improve battery state estimation and state of health estimation and tune degradation models. However, a few limitations of this work present opportunities for future research. The degradation model presented in this work can also be used as a digital twin for further studies into battery degradation.

7.2.1 Extension to Different Cell Chemistries

The cells used for degradation modeling in this work have an NMC111 chemistry, which exhibits less degradation than cathodes with higher Nickel content [68]. A possible extension of this work is adding cathode dissolution [69, 75, 76] as an additional degradation mechanism for NMC cathodes with higher Nickel content.

The framework presented in this work can also be extended to other Lithium-ion battery chemistries including different cathodes such as NCA, LFP, and also blended cathodes. These cathodes may need the inclusion of additional degradation mechanisms and the inclusion of the multiple-particle model (MPM) in the case of blended cathodes. Similarly, the model can also be extended to different anodes, such as silicon or silicon/graphite blends. The MPM is an extension to the SPM, which is necessary in the case of blended cathodes and/or anodes [33]. Modeling the link between expansion and degradation is vital for silicon-based anodes since their expansion is an order of magnitude higher than the graphite-based anodes.

The dominant degradation mechanisms are also pressure-dependent in next-generation lithium chemistries, which include Lithium Metal Solid-State batteries [77]. Thus, modeling the impact of pressure on degradation is essential to extend battery life.

7.2.2 Model Improvements

The phenomenological model for irreversible expansion in this thesis can be further improved with a more physics-based approach, which includes the effects of changes in battery mechanical properties with life and temperature. Having temperature dependent battery parameters can result in just tuning a single set of degradation model parameters to predict battery aging at multiple temperatures.

The mechanical damage model in this work was based on maximum and minimum stresses during a cycle. Calculating the impact of cycling on degradation from the experimental data is straightforward since the test protocol contained continuous constant current charge and discharge cycles. But if the charge and discharge cycles have varying currents and/or are discontinuous, cycle counting methods such as rainflow counting have to be employed. Thus, the model has to be extended using rainflow counting for predicting aging during drive cycles.

We observed two rates of resistance growth in Section 5.4.4, one at BOL and the other at MOL, which suggests a degradation mechanism that changes rates as the battery ages. Hybrid particle cracking and SEI growth mechanisms [19], could be used to capture the change in resistance growth rate from BOL to MOL. A gas generation model [78] can be added to predict cell expansion, capacity loss, and resistance growth when gassing has occurred, which was observed in the experimental testing with no externally applied pressure, as shown in Section 6.5.

Simulating DC fast charging for vehicle applications, corresponding to high currents, would require the use of higher order models such as SPMe or P2D to capture battery internal states accurately. The model tuning framework, which was based on the SPM, has to be implemented for the higher-order model to predict the spatially distributed degradation

at higher currents.

7.2.3 Model Validation

X-ray computed tomography can be used to validate the individual electrode thickness growth predicted by the model [70]. Unfortunately, the cells used in this work were too large for the current state-of-art X-ray microscopes (ZEISS Versa Advanced 3D XRM) to resolve individual electrode layers. As shown in work by [70], designing cells with lower geometric areas (facilitating rotation within the field of view) can be done in future experiments to validate the model.

7.2.4 Using Degradation Model for Charge Optimization

Charging time is an important barrier to making EVs more accessible and appealing. Fast charging, i.e., charging at higher currents, can enable the reduction of battery pack size and thus reduce EV cost [79]. In the survey conducted by Chen et al. [80], EV battery is considered a very important attribute preference by 72% of participants and EV Charging time by 51% of participants. The ability to fast charge at over 100 kW (¿1C charge rate) using direct current (DC) fast charging is becoming more prevalent [81]. Frequent fast charging accelerates degradation, and EV manufacturers limit the frequency and power level to reduce degradation. At higher currents, the increased side reaction overpotentials cause more lithium plating, and higher concentration gradients result in higher mechanical stress and capacity fade. The higher temperatures during fast charging also can lead to increased rates of SEI growth. Conventional charging uses the Constant Current (CC) - Constant Voltage (CV) protocol which is based on constraints on voltage and current measurements. CC-CV has been shown as the solution to the minimum-time optimization problem by [82]. However, CC-CV can violate internal constraints like plating overpotentials, which accelerates battery aging and intoduces safety concerns by creating Li metal dendrites. There have been several works that seek to improve battery charging [83, 84, 85, 86, 87, 88, 89, 90, 91]. Most optimal charging algorithms minimize the battery degradation for a single charge cycle. The effectiveness and impact of these charging algorithms throughout the battery's lifetime have not been previously studied. The accelerated degradation model can be used to evaluate fast charging algorithms and understand the impact of the internal battery constraints used in these algorithms on the battery's lifetime. The degradation models proposed in this thesis combined with the accelerated aging simulation framework would enable quick evaluation of the trade-offs between charge time and battery lifetime for the battery's internal constraints.

APPENDIX A

Electrode State of Health Estimation

Estimating the state of Health (SOH) is an integral part of the BMS. Accurate SOH estimation [92, 93, 94, 95, 96, 97] is necessary to operate the battery safely. The parameters associated with SOH include the cell capacity and resistance. Electrode state of health (eSOH) on the other hand includes additional parameters that give insight into the cell degradation modes which are loss of active material (LAM) and loss of lithium inventory (LLI) [98]. The additional parameters in eSOH include the capacities of negative and positive electrode C_{n}, C_{p}, the negative electrode stoichiometric limits x_0, x_{100}, and the positive electrode stoichiometric limits y_0, y_{100} as they shift and shrink with age. Due to these shits in material utilization, the aged batteries have different open circuit voltage (OCV) behavior that can greatly impede, if undiscovered, the classical capacity and state of charge (SOC) estimation. Thus estimation of the electrode capacity is critical for managing aged batteries and also for tuning the degradation model presented in this thesis.

The most common algorithm for joint state and parameter estimation to address the need to capture SOC and SOH simultaneously is the Kalman filter and its derivatives [99, 100]. Plett et al. [100] devised a method to estimate battery SOC, SOH, and also eSOH using a single particle model with electrolyte (SPMe) and sigma-point Kalman filters (SPKFs). They also acknowledged that estimating electrode capacities and stoichiometries requires low C-rates and full depth of discharge (DOD) and suggested that these parameters are updated under opportunistic events. Lee et al. [101, 55] have done extensive work on the estimation error of C_{n} for various cycling conditions and have developed methodology for calculating Cn estimation error bounds for specific DOD. Thus, we require updating strategies for eSOH estimation, which screen data based on error bounds to update the estimated values only when the data meets the required criterion of low C-rates and high DODs. Also, methods of estimating eSOH under high C-rates are necessary since low C-rate data is not always available. Expansion data has features that do not disappear under high C-rates [42], and that can be leveraged to improve eSOH estimation.

This appendix is organized as follows. Appendix A.1 shows how the model uses degradation mechanism states to estimate eSOH parameters in the aging simulations. Appendix A.2 presents the methodology to estimate eSOH parameters using voltage data. As described in Chapter 5, we tune the degradation model parameters to match eSOH from the data to the eSOH from the model. Appendix A.3 presents a way of updating eSOH parameters using screened voltage data. Finally, Appendix A.4 presents the methodology to estimate eSOH parameters using expansion data at high C-rates, where voltage estimation method fails.

A.1 Estimating eSOH from Degradation Model Variables

In addition to estimating eSOH from data, we need a method to estimate eSOH in the battery model. In our battery model, the eSOH parameters are estimated using the values of degradation variables and the methodology is discussed below. C_{n} and C_{p} are the scaled values of degradation variables $\varepsilon_{\mathrm{s}}^{-}, \varepsilon_{\mathrm{s}}^{+}$ and the relation is given in Eq. (4.22). The degradation variables are explained in detail in Section 5.2.2. Using the values of C_{n} and C_{p}, the value of degradation variable n_{Li} and the values of minimum voltage $V_{\min}$ and maximum voltage $V_{\max}$, we can estimate the stoichiometric windows by solving these equations simultaneously:

$$n_{\mathrm{Li}} = \frac{3600}{F}\left(x_{100}C_n + y_100C_p\right) \tag{A.1}$$

$$C = C_n\left(x_{100} - x_0\right) = C_p\left(y_0 - y_{100}\right) \tag{A.2}$$

$$V_{\max} = U^{+}(y_{100}) - U^{-}(x_{100}) \tag{A.3}$$

$$V_{\min} = U^{+}(y_0) - U^{-}(x_0) \tag{A.4}$$

The LLI can be quantified from the eSOH parameters by using the following equation:

$$LLI = \left(1 - \frac{n_{\mathrm{Li}}}{n_{Li,0}}\right) \times 100 \tag{A.5}$$

where $n_{Li,0}$ is n_{Li} at BOL.

Similarly, LAM can be quantified as:

$$LAM_{\mathrm{NE}} = \left(1 - \frac{C_n}{C_{n,0}}\right) \times 100 \tag{A.6}$$

$$LAM_{\mathrm{PE}} = \left(1 - \frac{C_p}{C_{p,0}}\right) \times 100 \tag{A.7}$$

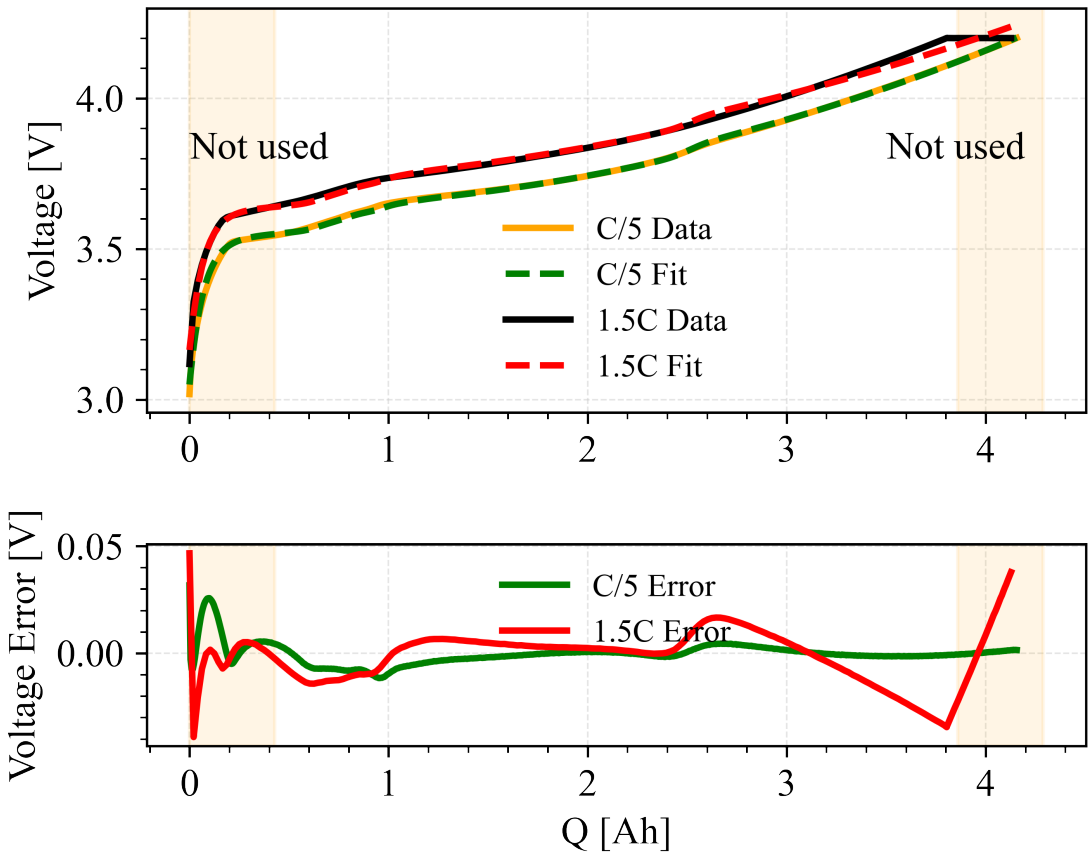


Figure A.1: Voltage fitting during a C/5 charge (yellow) and a 1.5C charge (black) to estimate C_{n} of a 16% aged cell. The data is shown in black, and the model fit is shown in red. The orange regions, which represent the first and last 10% during the charge, are not used in voltage fitting to improve the fitting accuracy.

where $C_{n,0}$ is C_n at BOL and $C_{p,0}$ is C_p at BOL

A.2 eSOH Based on Voltage Fitting of Electrode Open Circuit Potential

In this section, we introduce the method to calculate C_{n} from data using the voltage fitting method [101]. We take voltage data using the charging section of a cycle and estimate the value of C_{n} along with other eSOH parameters C_{p}, x_0, y_0 using a least-squares estimation framework:

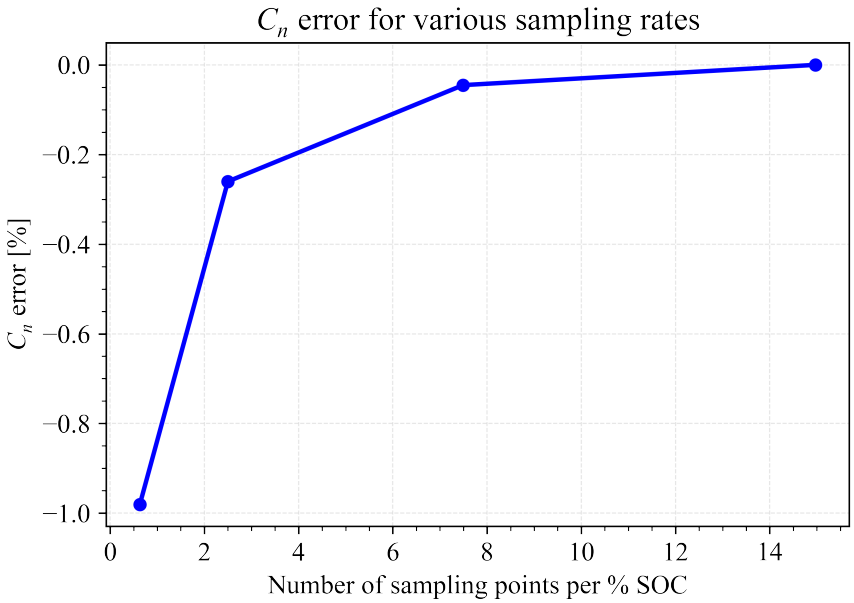


Figure A.2: C_{n} calculation error in % for various sampling rates. The error is less than 0.2% if we have more than 3 samples per % SOC.

$$\overline{X_v} = \min_{C_{\mathrm{n}}, C_{\mathrm{p}}, x_0, y_0} \sum_{i=1}^{n} \| V(Q_i) - V_{\mathrm{model}}(Q_i) \| \tag{A.8}$$

$$V_{\mathrm{model}} = \left(U_p(y_0 - \frac{Q_i}{C_p}) - U_n(x_0 + \frac{Q_i}{C_n}) \right) - IR_s \tag{A.9}$$

where C_{p} is positive electrode capacity, x_0 is negative electrode stoichiometry at 0% SOC, y_0 is positive electrode stoichiometry at 0% SOC, n is the number of time steps in the data vector for voltage, Q_i is charge capacity of the cell at i th time step, U_p is positive electrode open circuit potential, U_n is negative electrode open circuit potential, and I is current (discharge is positive).

A.3 A Strategy for Updating Estimated Electrode Capacity using Data Screening Based on Pre-computed Error Bounds

In this section, we design an observer for $\hat{C}_{\mathrm{n}}$ that fuses prior estimates from laboratory cycling data using an empirical degradation model coupled with high-confidence values of

$\overline{C_{\mathrm{n}}}$ that are calculated by voltage fitting of a dual tank model with open circuit potential ($\mathrm{OCP}_{n,p}$) during charging periods with constant current (or constant power) charging.

A.3.1 Methodology

In this section, we will introduce the strategy of updating C_{n} estimates $\hat{C}_{\mathrm{n}}$ by using $\overline{C_{\mathrm{n}}}$ values found by voltage fitting on data screened based on error bounds. We also describe the C_{n} empirical degradation model $DC_{\mathrm{n}}R$, which is used to predict C_{n} values as a function of cycle number, C-rate, and depth of discharge (DOD).

A.3.1.1 Electrode Capacity Degradation Update

Our strategy for estimating the electrode capacity degradation includes a model of C_{n} changes over life that captures sensitivity to the operating conditions, supplemented by a feedback mechanism in which we use only screened data to calculate and update C_{n}. The observer is shown in the below equations:

$$\begin{aligned}\hat{C}_{\mathrm{n},k+1} &= \hat{C}_{\mathrm{n},k} + DCnR(k, \text{C-rate}, \text{DOD}) \\ &\quad + L(\overline{C_{\mathrm{n},k}} - \hat{C}_{\mathrm{n},k})\end{aligned} \tag{A.10}$$

where $\hat{C}_{\mathrm{n},k}$ is the estimated capacity, $DCnR(k, \text{C-rate}, \text{DOD})$ is electrode degradation rate from the empirical model tuned on laboratory cycling data, $\overline{C_{\mathrm{n},k}}$ is the capacity calculated from voltage fitting in Eq. (A.8) during field opportunities and L is the observer gain which is determined by our update strategy. The work of [101, 55] shows that we need both high DOD and low C-rate to achieve an estimation error for C_{n} below 10% based on voltage fitting. At higher currents, the voltage output is different from the open circuit voltage due to diffusion in the electrode active material and the cell impedance. If the DOD is not large enough, the features in the voltage corresponding phase changes in the graphite (which result in voltage plateaus), are missing from the voltage data rendering C_{n} unobservable. The relatively flat open circuit voltage for the graphite leads to high errors in estimation for partial DOD cycles. For high DOD cycles, the data window size is large, and the error bound of C_{n} estimation decreases with the voltage data, once both phase transitions are crossed during charging. Hence, our strategy is to update C_{n} by choosing $L = 0.5$ only when the data meets the criterion of having high DOD and low C-rate:

$$L = \begin{cases} 0.5, \text{DOD} > 0.8, \text{ C-rate} < \text{C}/3 \\ 0, \text{otherwise.} \end{cases} \tag{A.11}$$

The gain value L must be $0 < L < 1$, so that a correction in $\hat{C}_{\mathrm{n}}$ is achieved when field calculated $\overline{C_{\mathrm{n}}}$ is accurate. Here we choose $L = 0.5$ to balance the $\overline{C_{\mathrm{n}}}$ measurement variability with a fast convergence rate.

A.3.1.2 Empirical Electrode Capacity Degradation Model

The eSOH model used in the observer is an empirical model first introduced in [102] and adopted for C_{n} in this work. The model predicts the negative electrode capacity loss during each cycle k, which the following basis function

$$C_{\mathrm{n}}(k) = a_1 + a_2 k^{0.4} + a_3 k^2 tanh(k) \tag{A.12}$$

where a_1, a_2, and a_3 are constants that depend on cycling C-rate and DOD. The empirical model's fit is depicted in Fig. A.3 for a set of graphite anode and NMC-111 cathode pouch cells with a nominal capacity of 5Ah and 3.0-4.2V operating voltage window. The cells were built at the University of Michigan Battery Lab and cycled under various conditions as part of an aging study conducted by Mohtat et al. [1]. The aging dataset can be found at [103]. The cycling procedure consists of a constant current (CC) charge until reaching 4.2 V, followed by a constant voltage (CV) phase at 4.2V until ($|I| < C/50$). Then a CC discharge until reaching 3.0 V for the full range conditions. For partial DOD, the discharge time was fixed throughout life with respect to the nominal capacity (i.e., to obtain 50% DOD, 2.5 Ah are discharged from a completely charged state). All the cells were cycled to at least 70% capacity retention, and reference performance tests (RPTs) were performed periodically to characterize degradation, consisting of a C/20 charge-discharge cycle. The extraction of C_n from the C/20 charging data was performed by the voltage fitting method in Eq. (A.8).

The optimal parameters a_i in the empirical model (Eq. 6) were computed using MATLAB's curve fitting toolbox via the least squares method. Data for tuning the model was obtained from six cells cycled continuously at $25°C$ at various C-rates and DODs (summarized in Table A.1):

For low currents ($< 1C$), the values of the fitted constants a_1, a_2 and a_3 are:

$$\begin{aligned} a_1 &= 6.3017 + 0.0172 \times \text{DOD} \\ &\quad + 0.0069 \times \text{C-rate} + 0.0011 \times \text{DOD} \times \text{C-rate} \end{aligned} \tag{A.13}$$

$$\begin{aligned} a_2 &= -0.0658 - 0.0143 \times \text{DOD} \times \text{C-rate} \\ &\quad 0.0095 \times \text{DOD} + 0.0083 \times \text{C-rate} \end{aligned} \tag{A.14}$$

$$\begin{aligned} a_3 &= 3.1396 \times 10^{-6} \\ &\quad - (1.4606 \times 10^{-5}) \times \text{DOD} + (6.9422 \times 10^{-8}) \times \text{C-rate} \\ &\quad + (3.6892 \times 10^{-6}) \times \text{DOD} \times \text{C-rate} \end{aligned} \tag{A.15}$$

For high currents ($\geq 1C$), the values of the fitted constants a_1, a_2 and a_3 are:

$$a_1 = 6.5147 - 0.1059 \times \text{C-rate} \tag{A.16}$$

$$a_2 = 0.0159 - 0.0668 \times \text{C-rate} \tag{A.17}$$

$$a_3 = 4.1951 \times 10^{-5} - (4.0255 \times 10^{-5}) \times \text{C-rate} \tag{A.18}$$

The degradation rate of C_n, $DC_\text{n}R(k, \text{C-rate}, \text{DOD})$ can be found by differentiating Eq. (A.12) with respect to k.

The electrode capacity degradation empirical model can be written as:

$$\hat{C}_{\text{n},k+1} = \hat{C}_{\text{n},k} + DC_\text{n}R(k, \text{C-rate}, \text{DOD}) \tag{A.19}$$

where k is cycle number, $\hat{C}_{\text{n},k}$ is the empirically predicted value of negative electrode capacity value at cycle k. We will use

$$D\hat{C}_\text{n}R = \epsilon_1 DC_\text{n}R + \epsilon_2 \tag{A.20}$$

Table A.1: Cycle Aging Test Conditions

Cell	Charge-Discharge C-rate	DoD
1	C/5—C/5	100%
2	1.5C—1.5C	100%
3	2C—2C	100%
4	C/5—1.5C	100%
5	C/5—C/5	50%
6	C/5—1.5C	50%

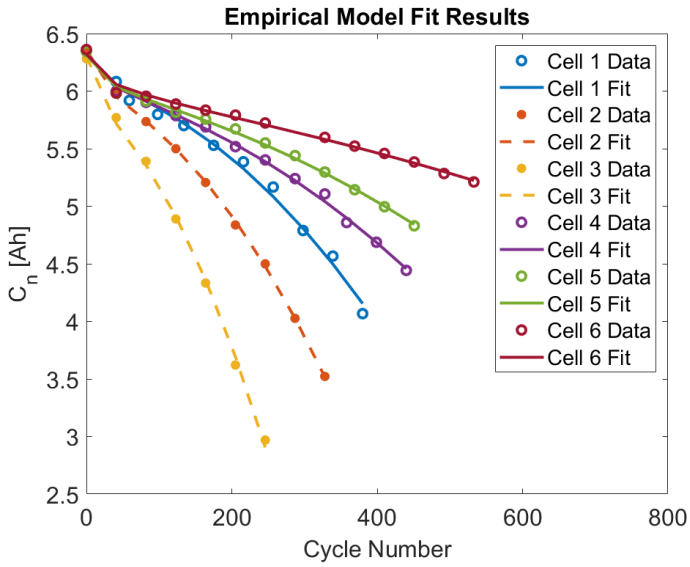


Figure A.3: Empirical Negative electrode Capacity degradation model. The dots represent the data used for fitting, the solid lines represent the model fit at low C-rates, and the dotted lines represent the model fit at high C-rates.

with $\epsilon_1 = 0.9$ and $\epsilon_2 = 0.001$ to introduce an error in the lab-determined degradation model for our online implementation that fuses the lab-derived and the field-derived $\hat{C}_\mathrm{n}$.

A.3.2 Results

The algorithm is applied on three continuous cycling cells at $25°C$. These three cells cover the following scenarios:

1. $L = 0.5$ during all cycles, i.e. we get frequent updates of C_n.
2. $L = 0.5$ during cycles at regular frequency, i.e., we get intermittent updates of C_n.
3. $L = 0.5$ during cycles at regular frequency but $L = 0$ after some cycles, i.e., we get intermittent updates of C_n for some cycles and no update after that. We also add an initialization error of 15% to the C_n observer and model mismatch to the empirical electrode capacity degradation model.

The results of running the observer on a cell cycled at C/5, 100% DOD, $25°C$ are shown in the Fig. A.4. The cell had reference performance tests (RPT) performed at regular intervals, in addition to regular cycling. The RPT consists of a very low C-rate (C/20) charge conducted to characterize cell aging. In the C/5 100% DOD, since both the cycles and RPTs meet the criterion of low C-rate and high DOD, the value of estimation gain L

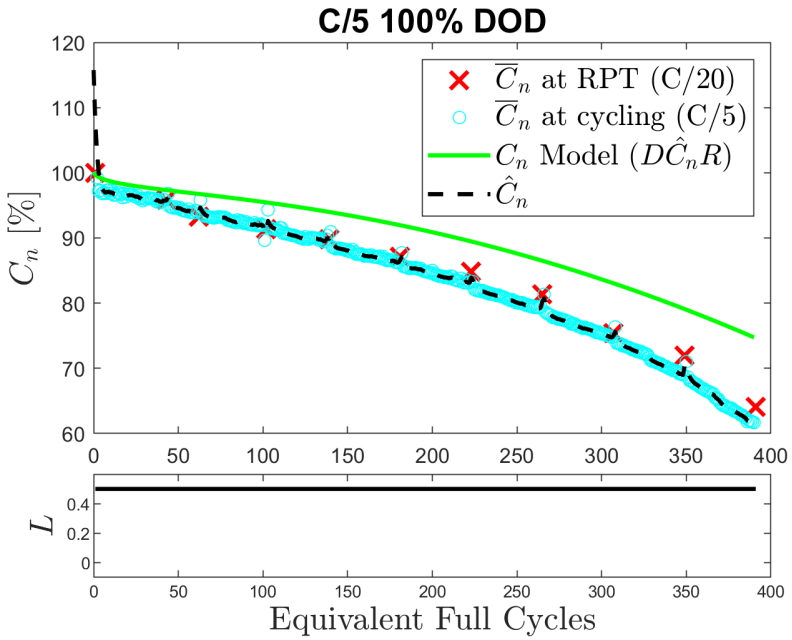


Figure A.4: C_n observer at C/5 100% DOD. The capacity in the plot is shown in the percentage of initial electrode capacity. The observed values $\hat{C}_\mathrm{n}$ [Eq. A.10] are shown as a black dashed line, the empirical degradation model C_n [Eq. A.19] (with model mismatch) as a green line, and voltage estimation values from voltage fitting $\overline{C}_\mathrm{n}$ [Eq. A.8] as cyan (during cycling) and as red (during RPT). The value of L for each cycle is also plotted. Since every cycle in this case has a low C-rate and high DOD, the value of $L = 0.5$ during all cycles.

is non-zero for all cycles. This leads to the observer tracking the values of C_n estimated from voltage fitting during both regular cycling (cyan dots in the figure) and the RPTs (red crosses in the figure). Since we have added a model mismatch to the C_n degradation model, the observer does not track the model but instead tracks the calculated C_n values from voltage fitting. Thus, regularly updating C_n from voltage fitting can help accurately track the electrode capacity even when a model mismatch exists.

The results of running the observer on a cell cycled at 1.5C, 100% DOD, 25°C are shown in the Fig. A.5. We observe a huge mismatch between C_n values estimated during cycling (cyan) and RPTs (red). This is because the cell was cycled at a high C-rate. Hence, the value of observer gain L is non-zero only during RPTs where the current is less than C/3. Hence the feedback from using voltage fitting C_n values is used only during RPT data, which occurs at regular intervals and not at every cycle. From the figure, we can see that the observed value of C_n tracks the values of RPT voltage fitted C_n values closely, even with a model mismatch (green). In this case, the rate of change of C_n between the voltage fitting updates is given by the empirical model, where the observer is open-loop and has no feedback. The

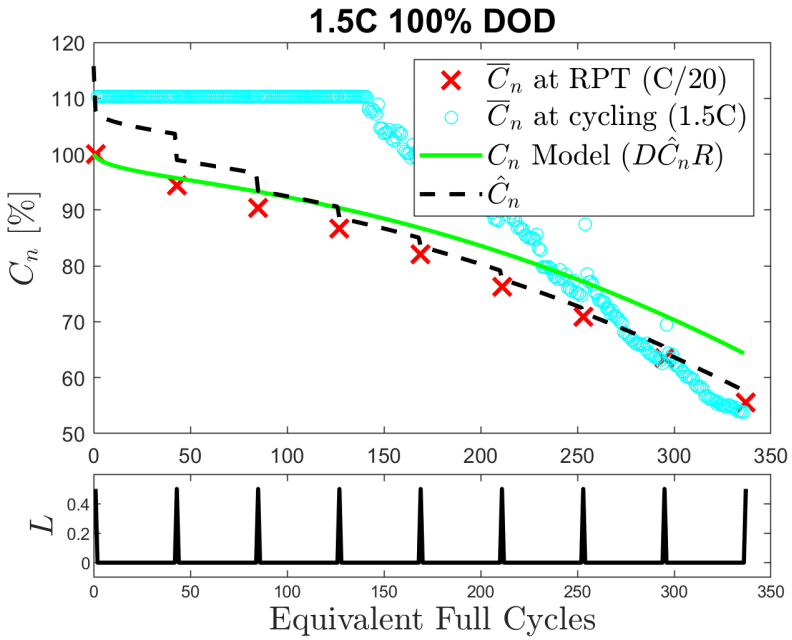


Figure A.5: C_{n} observer at 1.5C 100% DOD. The capacity in the plot is shown in the percentage of initial electrode capacity. The observed values $\hat{C}_{\mathrm{n}}$ [Eq. A.10] are shown as a black dashed line, the empirical degradation model C_{n} [Eq. A.19] as a green line, and voltage estimation values from voltage fitting $\overline{C_{\mathrm{n}}}$ [Eq. A.8] as cyan (during cycling) and as red (during RPT). The value of L for each cycle is also plotted. Since only the RPTs have low C-rate and high DOD, the value of $L = 0.5$ during only the RPTs. The rest of the cycles has $L = 0$.

feedback from the C_{n} updates helps reduce the error between observer and data, even with intermittent updates.

The results of running the observer on a cell cycled at C/5, 50% DOD, 25°C are shown in the Fig. A.6. Similar to the 1.5C, 100% DOD case, there is a mismatch between the values of C_{n} estimated during cycling (cyan) and RPTs (red). This is because the cell was not cycled at high DOD ($DOD > 80\%$). Therefore, the value of observer gain L is non-zero only during RPTs. However, in this case, we set $L = 0$ after 150 cycles, even during RPTs. We see that and the C_{n} observer tracks the C_{n} values estimated at RPTs closely till 150 cycles, after which the observer (black) deviates from the C_{n} data, because there is no update. After 150 cycles, the observer gets the rate of change of C_{n} with no update to correct the error from the model mismatch.

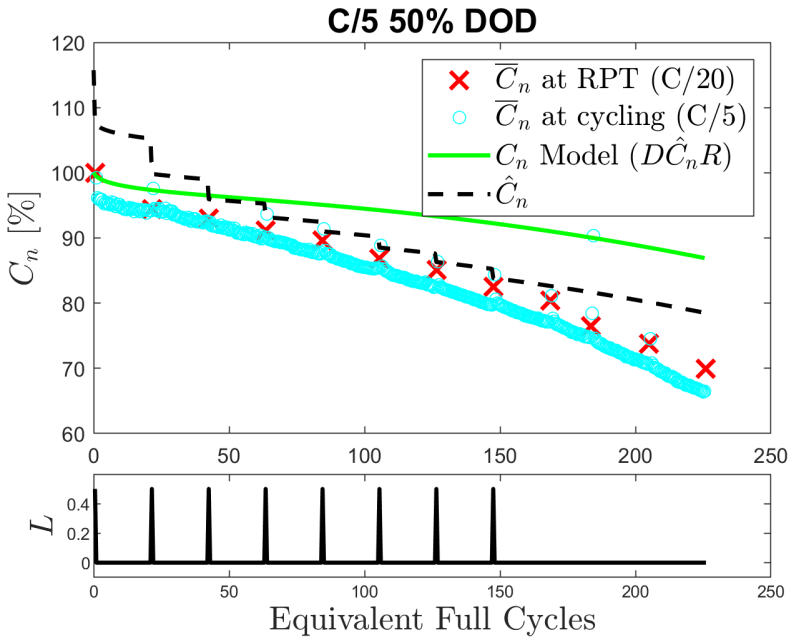


Figure A.6: C_{n} observer at C/5 50% DOD. The capacity in the plot is shown in the percentage of initial electrode capacity. The observed values $\hat{C}_{\mathrm{n}}$ [Eq. A.10] are shown as a black dashed line, the empirical degradation model C_{n} [Eq. A.19] as a green line, and voltage estimation values from voltage fitting $\overline{C_{\mathrm{n}}}$ [Eq. A.8] as cyan (during cycling) and as red (during RPT). The value of L for each cycle is also plotted. Since only the RPTs have low C-rate and high DOD, the value of $L = 0.5$ during only the RPTs. Here, we do not consider the data after 150 cycles for update which results in error between model and observer after 150 cycles.

A.4 Expansion Fitting to compute eSOH at high C-Rates

The estimation of degradation modes needs the process of electrode state of health (eSOH) estimation which is usually performed at very low C-rates of C/10 and below. At higher C-rates, this estimation cannot be performed, which presents a challenge in analyzing degradation modes. [42] has shown us that the peaks in the graphite electrode, that can be used to estimate the negative electrode capacity [104] vanish in the voltage signal but do not vanish in the expansion signal. These peaks, which exist in the 2nd derivative of the expansion signal can be seen in our data Fig. A.8. Thus, the expansion signal can be used to estimate the value of C_n in our data. In this section we start with the origin and location of peaks in the expansion signal, the methodology used to locate them and then finally the C_n estimation results.

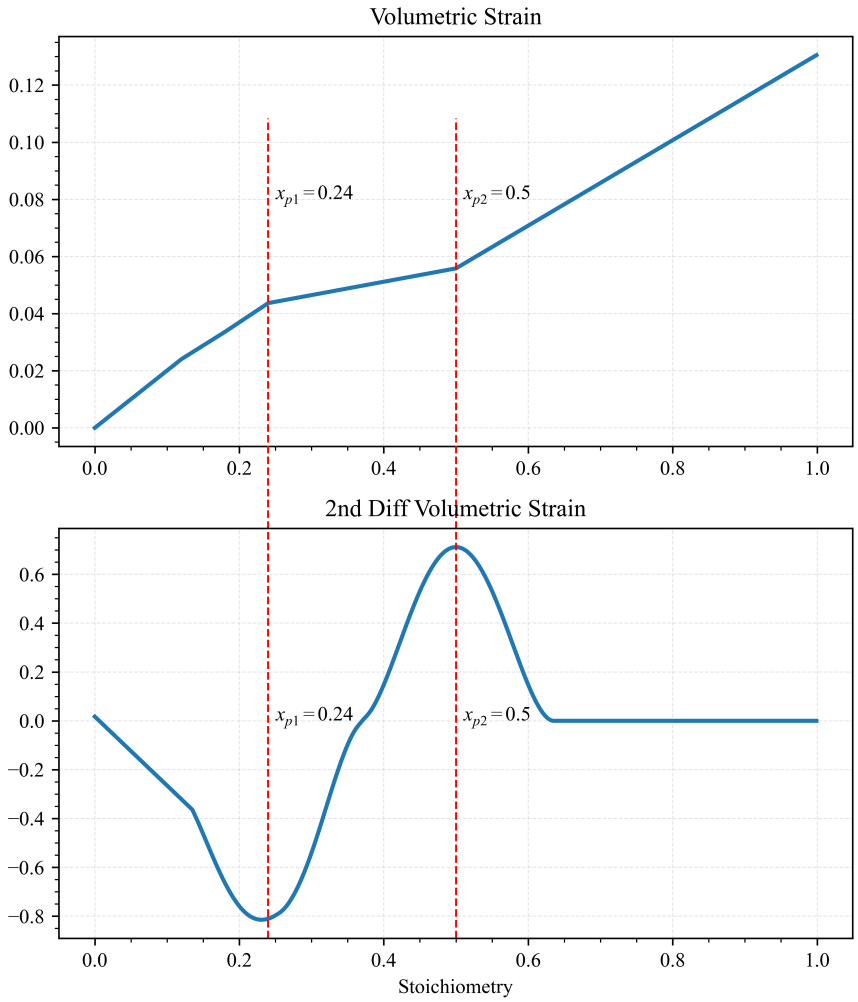


Figure A.7: Graphite Volumetric Strain and its 2nd derivative. The two peaks of 2nd derivative are located at stoichiometries 0.24 and 0.5

A.4.1 Origin of Peaks in Expansion Signals

When the graphite (negative electrode) in Li-ion batteries gains charge, it transitions between phases. Each of the phases have distinctive voltage plateaus. When the concentration of Li increases in graphite electrode, the electrode expands due to the change in lattice parameters and the structure of the electrode. The changes in the lattice structures occurs when there are phase transitions. Thus, each of the phases has a different strain rate due to the different lattice structures. So, each phase has different electrical and mechanical properties, and the transitions between them can be captured in the cell's electrical (terminal voltage) and mechanical (expansion) signals [55, 33, 42].

The volumetric strain curve of graphite is given in Fig. A.7 a). We can see that the strain rates i.e. the slopes of the volumetric strain curve are different at different graphite

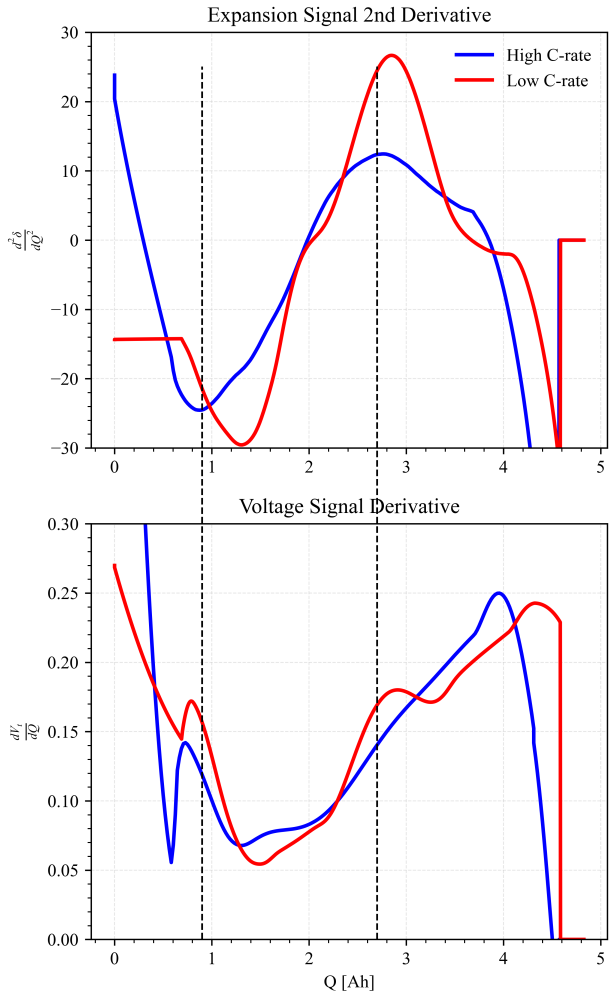


Figure A.8: Voltage vs Expansion Derivative Signals at high C-rate (2C) (blue) and low C-rate (red). The second peak (around 2.7 Ah) is present in the expansion signal but disappears in the voltage signal for high C-rate but is present at low C-rate.

stoichiometries i.e. each phase has its own strain rate. This leads to the two peaks in the 2nd derivative of the volumetric strain curve occurring at $x_{\mathrm{p1}} = 0.24$ and $x_{\mathrm{p2}} = 0.5$ as shown in Fig. A.7 b).

A.4.2 Estimation Methodology

The methodology used in this work to estimate the C_{n} is called peak finding method and is taken from [104], where the peaks in the differential voltage signal was used. In this work, we extend the method of peak finding to the 2nd derivative of the expansion signal and obtain peaks for estimating C_{n} from the 2nd derivative of the expansion signal instead of the derivative of the voltage signal. The expansion peaks are located at the negative electrode

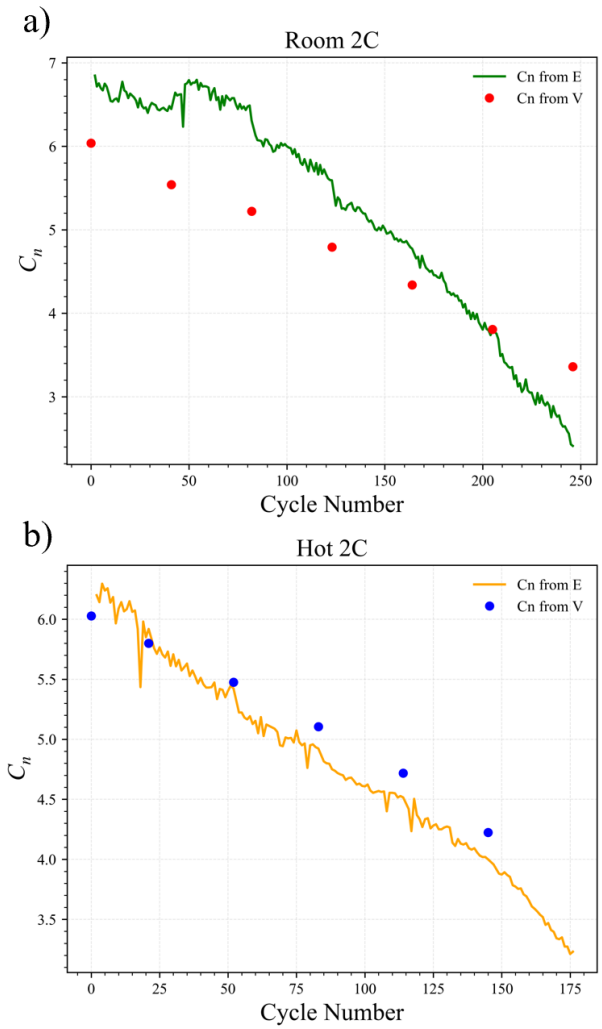


Figure A.9: Comparing Cn estimated using expansion method vs voltage method

(graphite) stoichiometries of $x_{\mathrm{p1}} = 0.24$ (1st peak) and $x_{\mathrm{p2}} = 0.5$ (2nd peak). Lets say that the peaks are located at the charge capacities of Q_{p1} (1st peak) and Q_{p2} (2nd peak). We know that the capacity of the battery at a particular negative electrode stoichiometry x is

$$Q = C_{\mathrm{n}}(x - x_0) \tag{A.21}$$

where Q is the capacity and x_0 is the negative electrode stoichometry at 0% SOC. Using the above equation we can find the relationship between x_{p1} and Q_{p1}, and between x_{p2} and Q_{p2}

$$Q_{\mathrm{p1}} = C_{\mathrm{n}}(x_{\mathrm{p1}} - x_0) \tag{A.22}$$

$$Q_{\mathrm{p2}} = C_{\mathrm{n}}(x_{\mathrm{p2}} - x_0) \tag{A.23}$$

Subtracting the above two equations, we have

$$Q_{\mathrm{p2}} - Q_{\mathrm{p1}} = C_{\mathrm{n}}(x_{\mathrm{p2}} - x_{\mathrm{p1}}) \tag{A.24}$$

$$C_{\mathrm{n}} = \frac{Q_{\mathrm{p2}} - Q_{\mathrm{p1}}}{x_{\mathrm{p2}} - x_{\mathrm{p1}}} \tag{A.25}$$

Thus, we have an equation which relates the values of Q_{p2} and Q_{p1} to C_{n}, giving us a method for estimating C_{n} if we know the location of peaks in the negative electrode i.e. the values of x_{p1} and x_{p2}.

A.4.3 Results

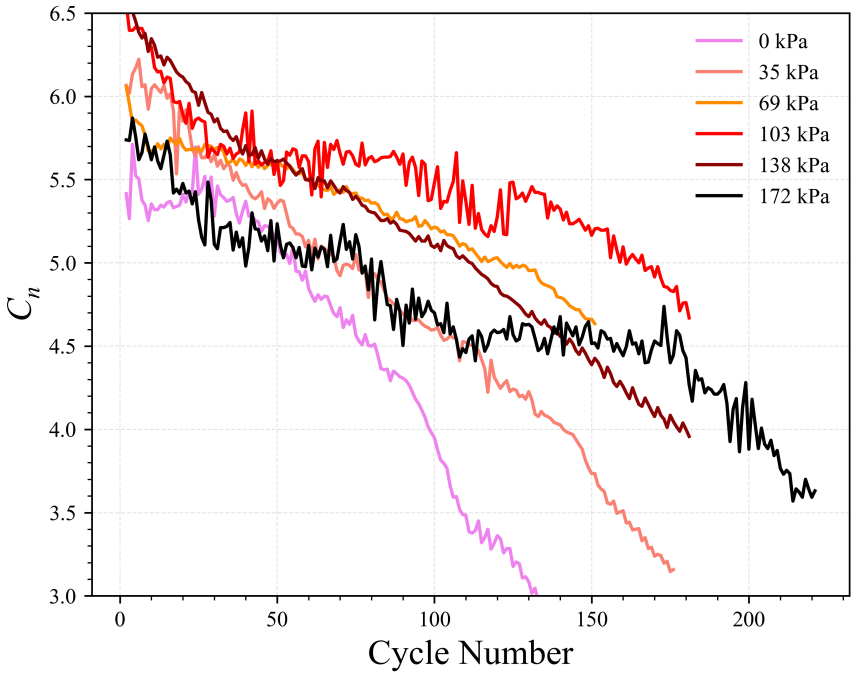


Figure A.10: Negative Electrode Capacity at various pressures

The values of C_n estimated using Eq. (A.25) at every cycle and voltage estimation method performed at cells which had RPTs available at regular intervals are shown in Fig. A.9. We see that the values of C_n are similar and show the same trends. This validates our novel approach in estimating C_n using continuous cycling data even at high C-rates. The estimated values of C_n for cells cycled at various pressures is shown in Fig. A.10. The C_n values estimated here will be later used in Chapter 6 to develop a model for impact of pressure on

degradation.

A.5 Conclusion

In this appendix, we describe the methodology of estimating eSOH parameters from voltage data. Afterwards, we design a strategy for determining the electrode capacity by fusing information from an empirical degradation model with the calculated capacity using voltage fitting from a charge cycle. Data screening based on analysis of error bounds is necessary to get low errors on electrode capacity estimates from voltage fitting during a charge cycle. The criterion for screening is using voltage data with high DOD and low C-rate. Finally, we introduce a novel way of estimating eSOH parameters at high C-rates using expansion data. Peaks from the second derivative of battery expansion can be used to estimate negative electrode capacity. The results of the expansion-based eSOH estimation method and a comparison with voltage-based methods are shown.

APPENDIX B

Application of Expansion: Improving Estimation of Electrode Level Lithiation

Various observers have been developed based on these reduced order models [105, 106]. In these observers voltage measurement is used to estimate the positive electrode states and the negative electrode states are indirectly calculated by using conservation of lithium in the battery [107], since the positive electrode states are more observable from the voltage measurement [108]. Thus, these observers are prone to large estimation errors when there is model parameter drift due to aging as the assumption of conservation of lithium leads to inaccurate results. Hence, a single measurement of voltage is insufficient to determine both electrode states [109]. Supplementing voltage measurement with battery expansion, which provides additional information about battery internal states, can help improve state estimation.

This appendix develops an observer for the state of lithiation using an electrochemical model. The observer uses voltage, expansion, and temperature measurements to estimate the individual electrode particle Lithium concentrations. We expand the state estimators based on voltage error injection to estimate the concentration in positive electrode particle proposed in [23], and augment the algorithm using the expansion error injection to estimate the negative electrode particle concentration. With the increase in the number of measurement signals, improvement of the estimator's performance under certain types of model parameter changes was achieved.

The observer was developed using an extension to SPM known as single particle model with electrolyte (SPMe), which we describe in Appendix B.1. The battery model in the observer also includes a thermal component, which is presented in Appendix B.2. We discuss the observer design in Appendix B.3. Then, we show the observer estimation results in Appendix B.4.

B.1 Single Particle Model with Electrolyte

In the observer, we use an extension to SPM called Single Particle Model with Electrolyte (SPMe) which which gives better prediction accuracy compared to SPM at high current rates. SPMe extends SPM by including electrolyte dynamics, which are described in this section. The electrolyte diffusion equations are derived based on the assumptions in [23] with boundary conditions: the continuity of c_e, and $\nabla c_e(0,t) = \nabla c_e(l^t,t) = 0$.

$$\epsilon_e \frac{\partial c_e}{\partial t}(x,t) = \nabla.(D_e^{eff} \nabla c_e(x,t)) + \frac{1-t_+^0}{F} \times \begin{cases} \frac{I(t)}{l^-} & 0 \le x < l^-, \\ 0 & l^- \le x \le l^- + l^s, \\ \frac{-I(t)}{l^+} & l^- + l^s < x \le l^t, \end{cases} \tag{B.1}$$

where $l^t = l^- + l^s + l^+$. The liquid-phase Ohm's law is shown in Eq. (B.2).

$$i_e(x,t) = -\kappa^{eff} \nabla \Phi_e(x,t) + \frac{2\kappa^{eff} RT}{F}(1-t_+^0)\left(1 + \frac{d\ ln\ f_\pm}{d\ ln\ c_e}(x,t)\right) \nabla(ln\ c_e)(x,t) \tag{B.2}$$

Integrating and applying the boundary condition results in

$$\begin{aligned} \Phi_e(l,t) = &-\left(\frac{l^-}{2(\epsilon^-)^{brugg}} + \frac{l^s}{(\epsilon^s)^{brugg}} + \frac{l^+}{2(\epsilon^+)^{brugg}}\right) \\ &\frac{I(t)}{\kappa} + \frac{2RT}{F} t_f (ln\ c_e(l^t,t) - ln\ c_e(0,t)) \end{aligned} \tag{B.3}$$

where the concentration dependence of the κ is neglected for simplicity, and the term $t_f = (1-t_+^0)\left(1 + \frac{d\ ln\ f_\pm}{d\ ln\ c_e}(x,t)\right)$ is assumed to be constant.

The terminal voltage in SPMe is different from SPM due to the addition of electrolyte dynamics and is given by Eq. (B.4) where U is the half-cell open circuit potential, and $V_R(x,t) = R_f F j(x,t)$ is the voltage drop due to the film resistance.

$$\begin{aligned} V_t(t) = h_v(c_{ss}^+, c_{ss}^-, c_e, I(t)) = \eta^+(t) + U^+(c_{ss}^+(t)) \\ + V_R^+(t) - \eta^+(t) U^-(c_{ss}^-(t)) - V_R^-(t) + \Phi_e(l^t,t) \end{aligned} \tag{B.4}$$

B.2 Thermal Model

The battery model in this observer also includes a thermal component, which predicts the battery temperature increase due to Joule heating. The thermal model used is a one-state

lumped model for battery temperature,

$$C_{th}\frac{dT_b}{dt}(t) = -h(T_b(t) - T_a(t)) + I(t)(U^+(c_{ss}^+(t)) - U^-(c_{ss}^-(t)) - V_t(t)) \tag{B.5}$$

where C_{th} is the lumped heat capacity, T_a is the ambient air temperature, h is the heat transfer coefficient, and the only source of heat generation inside the battery is Joule heating. The effect of Entropic heating can be ignored at the C-rates of interest.

The increase in temperature due to Joule heating, results in thermal expansion of the battery. Thus, in addition to intercalation-induced expansion, battery expansion now includes a thermal component. The lumped thermal model is used to predict the thermal expansion:

$$\delta_{th} = \alpha_{th}\left(T_b - T_0\right). \tag{B.6}$$

Here α_{th} is the thermal expansion coefficient and $T_0 = 298\,K$ is the reference temperature, and T_b is the battery temperature given by Eq. (B.5).

Now we calculate total battery expansion, which is the sum of intercalation-induced expansion and thermal expansion:

$$\delta_b = \delta_e + \delta_{th} \tag{B.7}$$

B.3 Battery State Observer Design

We discuss the observer design here. The battery state observer consists of observers for state of lithiation in the positive electrode, negative electrode and the electrolyte. Voltage inversion is used to get the estimate of positive electrode states. Open-loop observer is used to estimate the electrolyte states. Finally, expansion inversion which uses both expansion and temperature of battery as inputs, is used to estimate negative electrode states. The block diagram of the observer which describes how the different components are connected is shown in Fig. B.1. Appendices B.3.1 to B.3.3 are adopted from [23] and are briefly described below.

B.3.1 Positive Electrode Observer

The positive electrode observer uses a copy of model and injects boundary state error as shown in Eqs. (B.8) to (B.10)

$$\frac{\partial \hat{c}_s^+}{\partial t}(r,t) = D_s^+\left[\frac{2}{r}\frac{\partial \hat{c}_s^+}{\partial r}(r,t) + \frac{\partial^2 \hat{c}_s^+}{\partial r^2}(r,t)\right] + \overline{p}^+(r)\,[\check{c}_{ss}^+ - \hat{c}_{ss}^+] \tag{B.8}$$

$$\frac{\partial \hat{c}_s^+}{\partial r}(0,t) = 0 \tag{B.9}$$

$$\frac{\partial \hat{c}_s^+}{\partial r}\left(R_p^+, t\right) = \frac{I(t)}{D_s^- F a_s^- l^-} + \overline{p}_0^+ \left[\check{c}_{ss}^+ - \hat{c}_{ss}^+\right] \tag{B.10}$$

where $\check{c}_{ss}^+$ is inverted surface concentration calculated using Eq. (B.17). The observer gains are derived with the backstepping approach:

$$\overline{p}^+(r) = \frac{-\lambda D_s^+}{2R_p^+ \overline{z}} \left[I_1(\overline{z}) - \frac{2\lambda}{\overline{z}} I_2(\overline{z}) \right] \tag{B.11}$$

$$\overline{z} = \sqrt{\lambda \left(\frac{r^2}{(R_p^+)^2} - 1 \right)} \tag{B.12}$$

$$\overline{p}_0^+ = \frac{1}{2R_p^+}(3-\lambda), \quad \text{for } \lambda < \frac{1}{4} \tag{B.13}$$

where $I_1(z)$ and $I_2(z)$ are first and second order modified Bessel functions of the first kind, and λ controls the eigenvalue locations and determines the convergence rate.

B.3.2 Voltage Inversion

In this section we use a nonlinear gradient algorithm which estimates $\check{c}_{ss}^+$ by inverting the nonlinear V_t output function given in Eq. (B.4).

$$V_t(t) = h_v(c_{ss}^+, t) \tag{B.14}$$

The dependency of this nonlinear output function on c_{ss}^-, Φ_e and $I(t)$ is suppressed to a single dependence on t. We now define inversion error signal $e_V(t)$ in Eq. (B.15) and regressor signal $\phi_v(t)$ in Eq. (B.16).

$$e_v(t) = V_t(t) - h_v(\check{c}_{ss}^+, t) \tag{B.15}$$

$$\phi_v(t) = \frac{\partial h_v}{\partial c_{ss}^+}(\check{c}_{ss}^+, t) \tag{B.16}$$

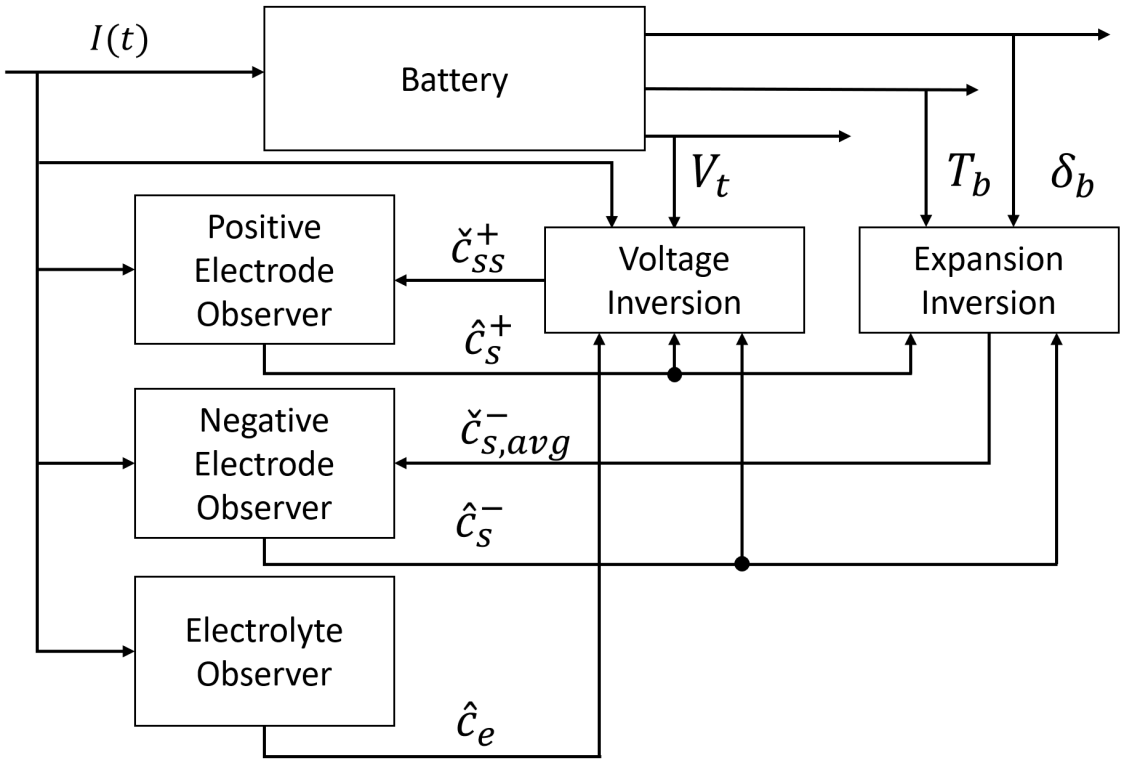


Figure B.1: Observer Schematic Diagram. The positive electrode observer depends on the inverted surface concentration $\check{c}_{ss}^{+}$ from the voltage inversion block which uses measured battery terminal voltage V_t. The voltage inversion depends on the open loop Electrolyte concentration estimate $\hat{c}_e$. The estimated positive electrode concentration $\hat{c}_s^{+}$ is then used in the expansion inversion block in combination with the measured battery temperature T_b and expansion δ_b to inform the negative electrode observer $\hat{c}_s^{-}$ using inverted negative electrode average concentration $\check{c}_{s,avg}^{-}$.

A Gradient update law for $\check{c}_{ss}^{+}$ is given by Eq. (B.17), where γ_v is a tuning parameter.

$$\frac{d}{dt}\check{c}_{ss}^{+} = \gamma_v \phi_v(t) e_v(t) \tag{B.17}$$

B.3.3 Electrolyte Observer

The electrolyte observer used is a open-loop observer which has the same form as the model. The equations of the observer are provided in Eq. (B.18) with boundary conditions: the

continuity of $\hat{c}_e$, and $\nabla \hat{c}_e(0,t) = \nabla \hat{c}_e(l,t) = 0$.

$$\epsilon_e \frac{\partial \hat{c}_e}{\partial t}(x,t) = \nabla.(D_e^{eff} \nabla \hat{c}_e(x,t)) + \frac{1-t_+^0}{F} \times \begin{cases} \frac{I(t)}{l^-} & 0 \leq x < l^-, \\ 0 & l^- \leq x \leq l^- + l^s, \\ \frac{-I(t)}{l^+} & l^- + l^s < x \leq l, \end{cases} \tag{B.18}$$

B.3.4 Negative Electrode Observer

The negative electrode observer uses a copy of model and injects $c^-_{s,avg}$ error as shown in Eqs. (B.19) to (B.21)

$$\frac{\partial \hat{c}_s^-}{\partial t}(r,t) = D_s^- \left[\frac{2}{r} \frac{\partial \hat{c}_s^-}{\partial r}(r,t) + \frac{\partial^2 \hat{c}_s^-}{\partial r^2}(r,t) \right] + k^- \left[\check{c}^-_{s,avg} - \hat{c}^-_{s,avg} \right] \tag{B.19}$$

$$\frac{\partial \hat{c}_s^-}{\partial r}(0,t) = 0 \tag{B.20}$$

$$\frac{\partial \hat{c}_s^-}{\partial r}\left(R_p^-, t\right) = \frac{-I(t)}{D_s^- F a_s^- l^-} \tag{B.21}$$

where k^- is the feedback gain which determines the system stability and convergence rate. Note by comparison of Eqs. (B.10) and (B.21), the anode observer does not adjust the estimate of the concentration gradient, only the average value, and relies on the open loop dynamics for prediction of the concentration gradient.

B.3.5 Expansion Inversion

We use the expansion measurement δ_b and the temperature measurement T_b to estimate the average negative electrode concentration $\check{c}^-_{s,avg}$. The steps followed are described below.

B.3.5.1 Estimating negative electrode particle displacement

We start by first estimating the thermal expansion by using the battery temperature measurement.

$$\hat{\delta}_{th} = \alpha_{th}\left(T_b - T_0\right) \tag{B.22}$$

Then we use the positive electrode observer states $\hat{c}_s^+(t)$ to estimate positive electrode expansion δ^+.

$$\hat{u}_R^+(t) = \frac{1}{(R_p^+)^2} \int_0^{R_p^+} \rho^2 \Delta\mathcal{V}\left(\hat{c}_s^+(\rho,t)\right) d\rho \tag{B.23}$$

$$\hat{\delta}^+ = a_s^+ l^+ \hat{u}_R^+(t) \tag{B.24}$$

Both of these estimates are used to estimate the negative electrode expansion as shown in Eq. (B.26).

$$\check{\delta}_e = \kappa_b \left(\check{\delta}_e^- + \hat{\delta}_e^+\right) = \delta_b - \hat{\delta}_{th} \tag{B.25}$$

$$\check{\delta}_e^- = \frac{\delta_b - \hat{\delta}_{th}}{\kappa_b} - \hat{\delta}_e^+ \tag{B.26}$$

Finally, the particle displacement at the surface is calculated as:

$$\check{u}_R^-(t) = \frac{\check{\delta}_e^-}{a_s^- l^-}. \tag{B.27}$$

B.3.5.2 Estimating negative electrode average concentration

Next, we develop a way to estimate average negative electrode concentration from negative electrode particle displacement. To start, we first define a new variable $\tilde{c}_s^-$ in Eq. (B.28).

$$\tilde{c}_s^-(r,t) = \hat{c}_s^-(r,t) - \hat{c}_{s,avg}^- \tag{B.28}$$

where $\hat{c}_{s,avg}^-$ is the average negative electrode concentration of the observer states calculated in Appendix B.3.4 . We now use the $\tilde{c}_s^-(r,t)$, $\check{u}_R^-(t)$ from Eq. (B.27) and Eq. (3.32) to estimate the inverted negative electrode average concentration $\check{c}_{s,avg}^-(t)$, by solving

$$\check{u}_R^-(t) = h_e(\tilde{c}_s^-(r,t) + c_{s,avg}^-(t)) = \frac{1}{(R_p^-)^2} \int_0^{R_p^-} \rho^2 \Delta\mathcal{V}\left(\tilde{c}_s^-(\rho,t) + c_{s,avg}^-(t)\right) d\rho. \tag{B.29}$$

To solve Eq. (B.29) we implement a gradient update law similar to voltage inversion in Appendix B.3.2. We now define inversion error signal $e_e(t)$ in Eq. (B.30) and regressor signal $\phi_e(t)$ in Eq. (B.31). Gradient update law for $\check{c}_{s,avg}^-$ is given by Eq. (B.32), where γ_e is a tuning

parameter.

$$e_e(t) = \breve{u}_R^-(t) - h_e(\tilde{c}_s^-(r,t) + \breve{c}_{s,avg}^-(t)) \tag{B.30}$$

$$\phi_e(t) = \frac{\partial h_e}{\partial c_{s,avg}^-}(\tilde{c}_s^-(r,t) + \breve{c}_{s,avg}^-(t)) \tag{B.31}$$

$$\frac{d}{dt}\breve{c}_{savg}^- = \gamma_e \phi_e(t) e_e(t) \tag{B.32}$$

This introduces a dynamic coupling between the concentration state observers for the positive and negative electrodes.

B.4 Results

Simulation results of the observer on the plant model are presented here. The diffusion equations in the model and observer are discretized using method of lines with second-order approximation of the boundary conditions [110]. Additional noise is added to voltage and expansion signals with a standard deviation of $1\,mV$ for voltage and $1\,\mu m$ for expansion.

B.4.1 Constant Current Charge

First we simulate a constant current charge of 1C. The simulated battery is initialized with $SOC_0 = 0.05$ and the observer with $\hat{SOC}_0 = 0.1$. The following observer parameters are used for the simulations; $\gamma_v = 10^8$, $\lambda = -20$ and $\gamma_e = 10^{22}$. Further discussion on how these gains are tuned can be found in [23]. Fig. B.2 shows simulation results for two gains $\kappa^- = 0.001$ and $\kappa^- = 0.01$. We can see that $\hat{V}_t$, $\Delta\hat{t}_b$, $\hat{c}_{ss}^-$, $\hat{c}_{s,avg}^-$, $\hat{c}_{ss}^+$ and $\hat{c}_{s,avg}^+$ converges for both gains, but faster for $\kappa^- = 0.01$. Hence, we use the value of $\kappa^- = 0.01$ for further simulations and analysis. The terminal voltage $\hat{V}_t$ converges faster than $\Delta\hat{t}_b$ as $\hat{V}_t$ depends on $\hat{c}_{ss}$ convergence but $\Delta\hat{t}_b$ depends on $\hat{c}_{s,avg}$ convergence which is slower. This is because $\hat{c}_{s,avg}$ is a linear combination of all $\hat{c}_s(r)$ states and convergence of $\hat{c}_{s,avg}$ depends on convergence of all the states including faster and slower states. We compare the performance of the Voltage and Expansion based observer (referred to as V+EXP-obs) which uses voltage, temperature and expansion measurements for with the one in [23], which uses only voltage measurement (referred to as V-obs). The root mean square percent error (RMSPE) of $\Delta\hat{t}_b$, $\hat{c}_{ss}^-$, $\hat{c}_{s,avg}^-$, $\hat{c}_{ss}^+$ and $\hat{c}_{s,avg}^+$ estimates after five minutes of simulation are given in Table B.1. While the RMSPE of positive electrode concentration estimates have similar values for both V+EXP-obs and V-obs, the RMSPE of negative electrode concentration estimates is slightly higher for V-obs.

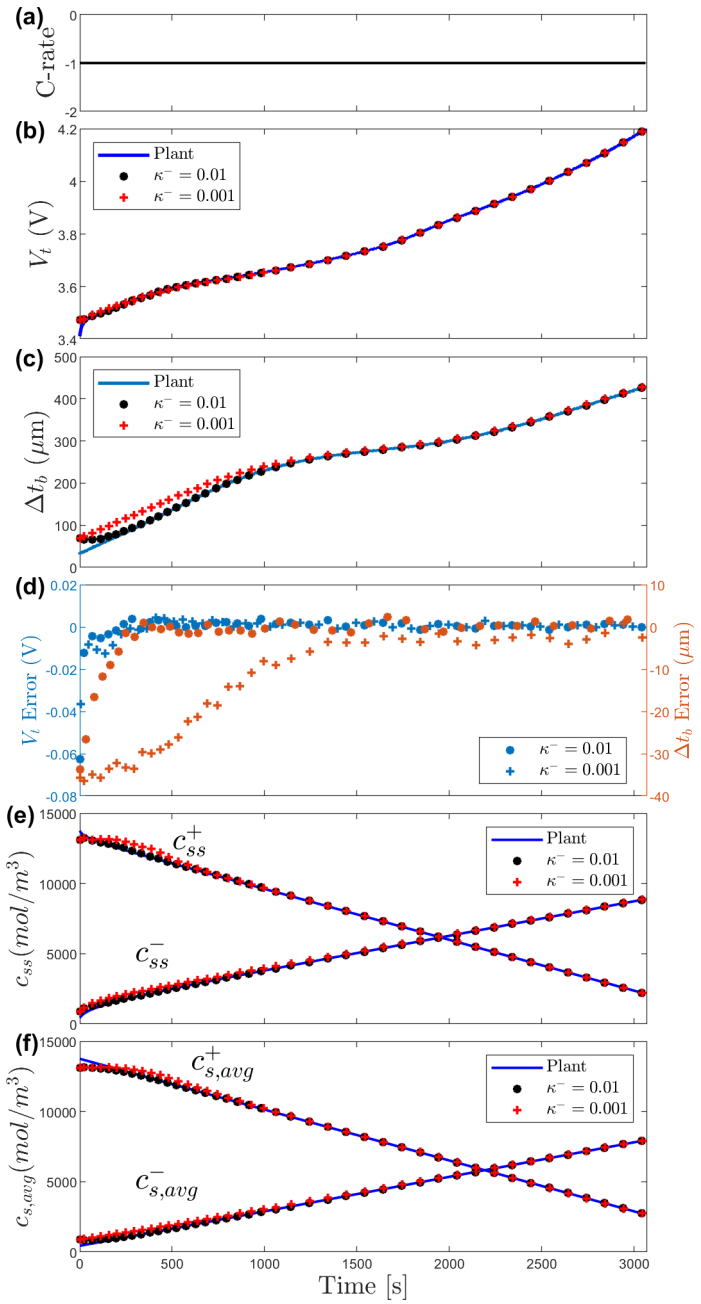


Figure B.2: Simulation results for 1C Constant Current input with $SOC_0 = 0.05$ and $\hat{SOC}_0 = 0.10$ shown for two gains $\kappa^- = 0.001$ and $\kappa^- = 0.01$. (a) Current (b) Voltage (c) Expansion (d) Voltage and Expansion Errors (e) Surface Concentration of both electrodes c_{ss}^-, c_{ss}^+ (f) Average Concentration of both electrodes $c_{s,avg}^-, c_{s,avg}^+$. Voltage and expansion converge to the measured values within 5 minutes.

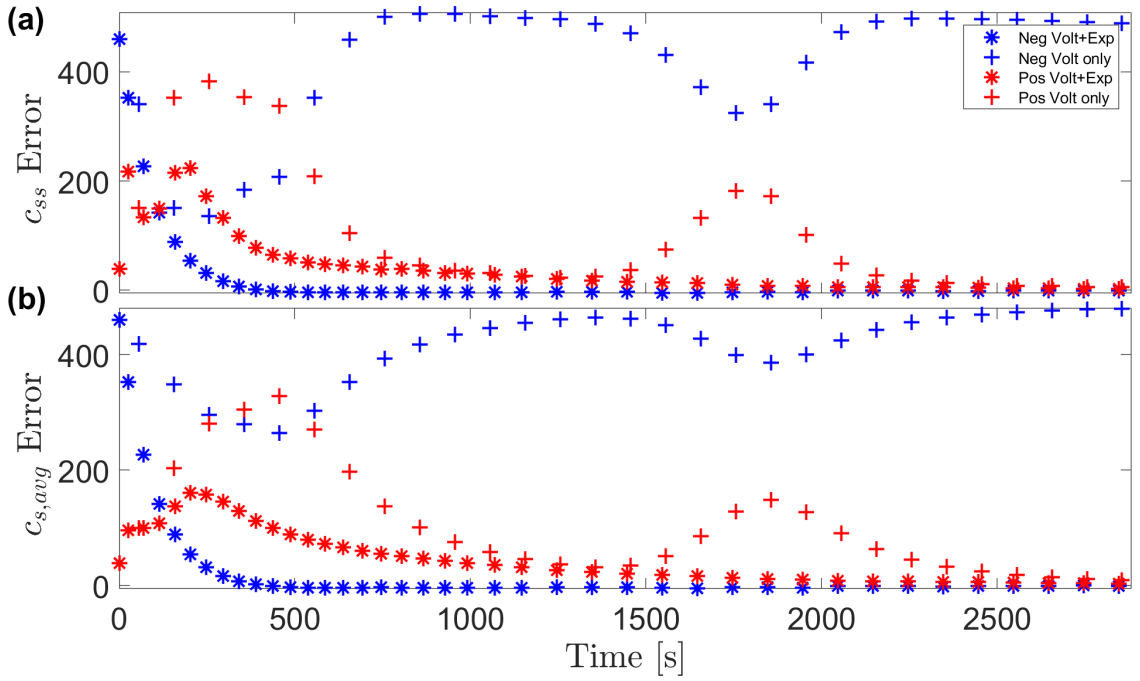


Figure B.3: Simulation results for Stoichiometric Window Drift for Voltage and Expansion observer and Voltage only observer during Constant Current charge at 1C rate with $SOC_0 = 0.05$ and $\hat{SOC}_0 = 0.10$. (a) Surface Concentration error of both electrodes $c^-_{s,s}, c^+_{s,s}$ (b) Average Concentration error of both electrodes $c^-_{s,avg}, c^+_{s,avg}$. $\hat{c}^+_s$ converges for both observers, but $\hat{c}^-_s$ converges only for V+EXP-obs.

B.4.2 Model Mismatch due to Aging

As the battery ages a number of parameters in the model drift from their initial values. Hence, it is important to evaluate the observer performance with uncertainty in parameters. There are number of aging mechanisms that contribute to parameter mismatch during aging, namely loss of lithium inventory (LLI) and loss of active material (LAM). It is known that these aging mechanisms affect the battery parameters like stoichiometric windows in negative electrode x_{100} and in positive electrode y_0, and active material ratio of negative electrode ϵ^-_s, which change as the battery ages [111].

B.4.2.1 Stoichiometric Window Change

First we simulate a case where both x_{100} and y_0 are reduced by 5% in the plant due to aging, and the parameters in observer are unchanged. The observer and plant are initialized as in Appendix B.4.1. The results of the simulations are shown in Fig. B.3. We can see that while the $\hat{c}^+_{ss}$ and $\hat{c}^+_{s,avg}$ converge for both observers, $\hat{c}^-_{ss}$ and $\hat{c}^-_{s,avg}$ converges for the V+EXP-obs but not for V-obs. This is because additional feedback in V+EXP-obs compensates for the

model mismatch in the negative electrode parameters resulting in better estimation of $\hat{c}_s^-$ states, while in V-obs the $\hat{c}_s^-$ states are calculated by using lithium conservation. Also, this higher $\hat{c}_s^-$ error in V-obs causes higher error in $\hat{c}_{ss}^+$ as shown in Table B.1.

B.4.2.2 Active Material Loss

Next we simulate a 5% parametric error in the negative electrode volume fraction, ϵ_s^- due to aging. The observer and simulated battery are initialized as in Appendix B.4.1. The results of the simulations are shown in Fig. B.4. We can see that while the $\hat{c}_{ss}^+$ and $\hat{c}_{s,avg}^+$ converge for both observers, both $\hat{c}_{ss}^-$ and $\hat{c}_{s,avg}^-$ do not converge neither for V+EXP-obs nor V-obs. Also the error of $\hat{c}_{s,avg}^-$ is higher in V+EXP-obs compared to V-obs as seen from the RMSPE values given in Table B.1. This is because ϵ_s^- is used in the output function inversion of expansion leading to inaccurate estimation of $\check{c}_{s,avg}^-$, thus resulting in inaccurate estimates of $\hat{c}_s^-$ states in V+EXP-obs.

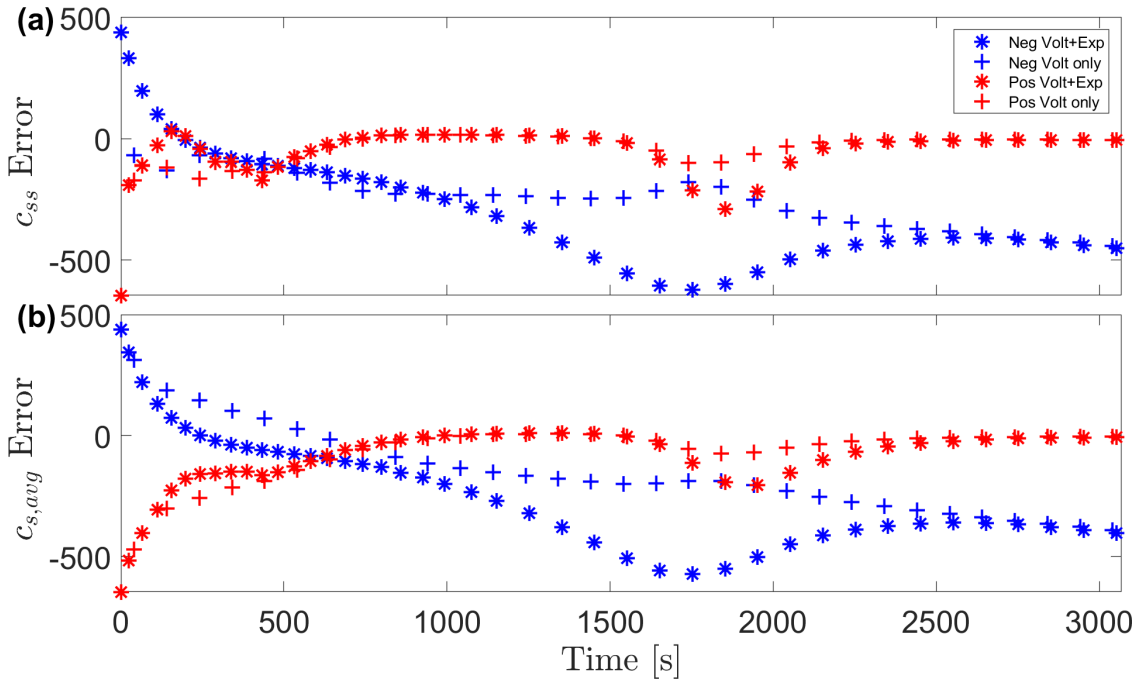


Figure B.4: Simulation results for Active Material Ratio Drift for V+EXP-obs and V-obs with $SOC_0 = 0.05$ and $\hat{SOC}_0 = 0.10$. (a) Surface Concentration error of both electrodes $c_{s,s}^-, c_{s,s}^+$ (b) Average Concentration error of both electrodes $c_{s,avg}^-, c_{s,avg}^+$. The estimates of negative electrode concentration states $\hat{c}_s^-$ does not converge for either observer.

Table B.1: Simulation Error in RMSPE (after 5 minutes) of Concentration Estimates for V+EXP-obs and V-obs

Estimates	Simulation Error (%)					
	Fresh Cell		Aged Cell			
			Stoich Change [1]		ϵ_s^- Loss [2]	
	V+E	V	V+E	V	V+E	V
$\hat{c}_{ss}^-$ †	0.2	1.2	0.1	9.3	6	4.6
$\hat{c}_{s,avg}^-$ §	0.4	2	0.2	11.6	6.3	4
$\hat{c}_{ss}^+$ †	0.3	0.2	0.3	1.4	1.1	4.6
$\hat{c}_{s,avg}^+$ §	0.2	0.4	0.4	1.3	1	4.6

[1] Stoichiometric window change
[2] Active material loss
† Negative/Positive electrode surface concentration
§ Negative/Positive electrode average concentration

B.4.3 Summary of Simulation Results

The outputs concentration state estimation errors for $\hat{c}_{ss}^-$, $\hat{c}_{s,avg}^-$, $\hat{c}_{ss}^+$ and $\hat{c}_{s,avg}^+$, after the initial convergence period, are given in Table B.1. These errors are calculated with the values after five minutes to simulations to normalize initialization errors across the simulations. The negative electrode concentrations $\hat{c}_{ss}^-$ and $\hat{c}_{s,avg}^-$ of V+EXP-obs have slightly lower errors for Constant Current simulation compared to V-obs. For the 1C charge simulation for the aged cell with change in stoichiometric window, the concentration errors for $\hat{c}_{ss}^-$ in V-obs is 9.3% which is much higher than 0.1% for V+EXP-obs. The error in $\hat{c}_{ss}^+$ is higher in V-obs. For the ϵ_s^- loss case all the concentration errors have high values for both the observers. While $\hat{c}_{ss}^-$ of V+EXP-obs has error of 6% and V-obs has a slightly lower error of 4.6%, $\hat{c}_{ss}^-$ of V+EXP-obs has a lower error of 1.1% against 4.6% of V-obs.

B.5 Conclusion

In this appendix we have developed a state observer for a physics based single particle Li-ion battery model by augmenting the voltage measurement with expansion measurement. The observer shows improved convergence of the concentration states. The observer performance is also evaluated against parametric modeling error representative of battery aging. This model parameter mismatch causes error in the negative electrode concentration states when using only voltage measurement for state estimation. Although the addition of expansion

measurement doesn't improve observer performance in the case of negative electrode active material ratio drift, the proposed observer was able to compensate for drift in stoichiometric windows. Accurate estimation of negative solid-surface concentration can enable more robust constraints on the state during charging and prevent degradation mechanisms like lithium plating during high C-rates.

APPENDIX C

Explaining the Outlier in Negative Electrode Capacity

In this appendix, we will discuss the cell aged at 138 kPa, which has an outlier negative electrode capacity loss trend.

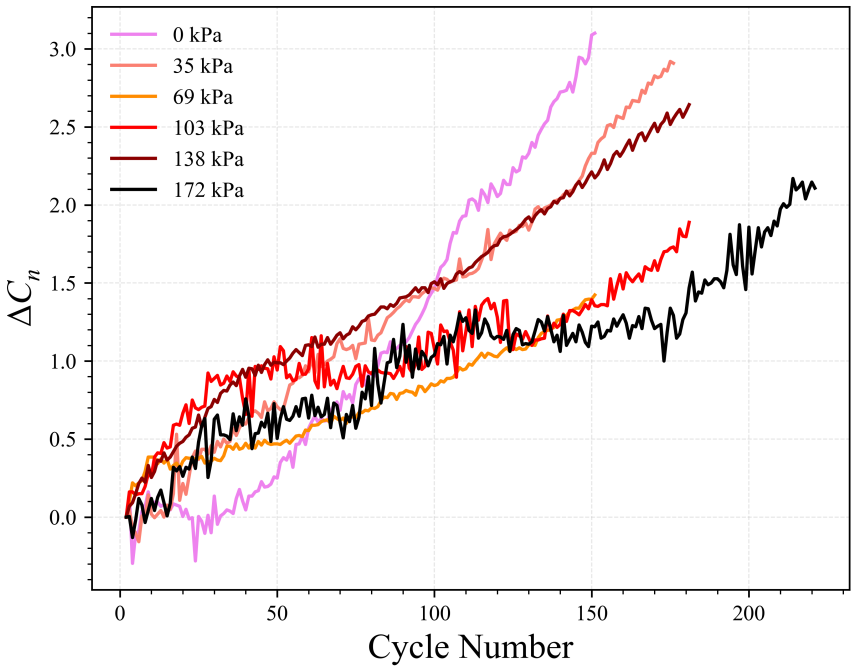


Figure C.1: Negative Electrode Capacity Loss at various pressures plotted

Fig. C.1 shows the estimated negative electrode capacity loss from expansion fitting, plotted at various pressures between 0-172 kPa. As the pressure increases, the ΔC_n decreases until 69 kPa, after which it doesn't decrease further. The cells cycled at 69, 103, and 172 kPa all have similar ΔC_n curves. But the cell cycled at 138 kPa has a much higher ΔC_n rate compared to other cells cycled at higher pressures. If we want to tune the pressure-

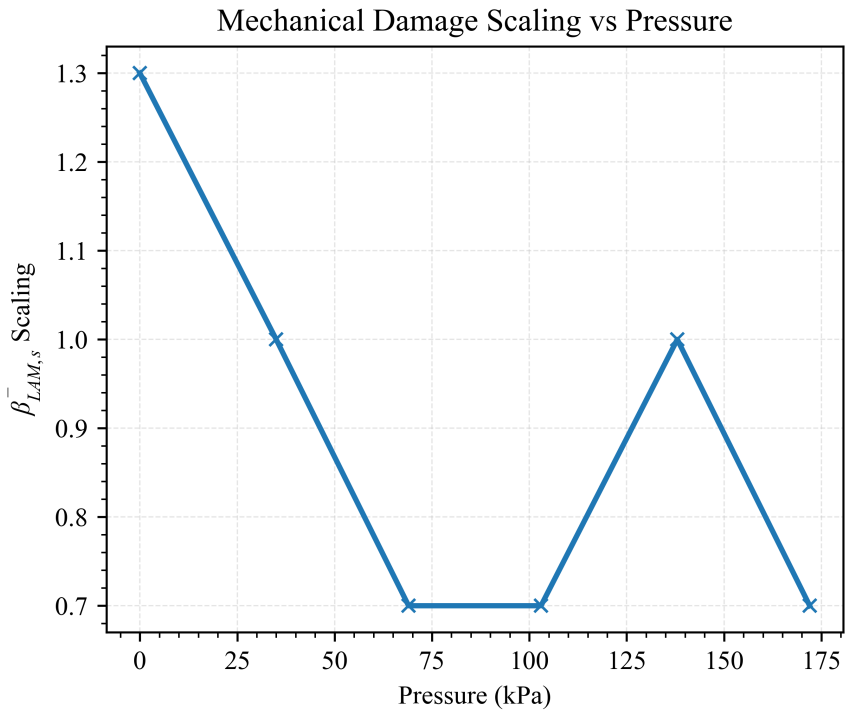


Figure C.2: Negative Electrode Mechanical Damage Coefficient (Scaled) $\beta^-_{\mathrm{LAM},s}$ vs Pressure

dependent degradation parameter $\beta^-_{\mathrm{LAM},s}(P)$ including the ΔC_n values at 138 kPa, we get the $\beta^-_{\mathrm{LAM},s}(P)$ vs P curve shown in Fig. C.2.

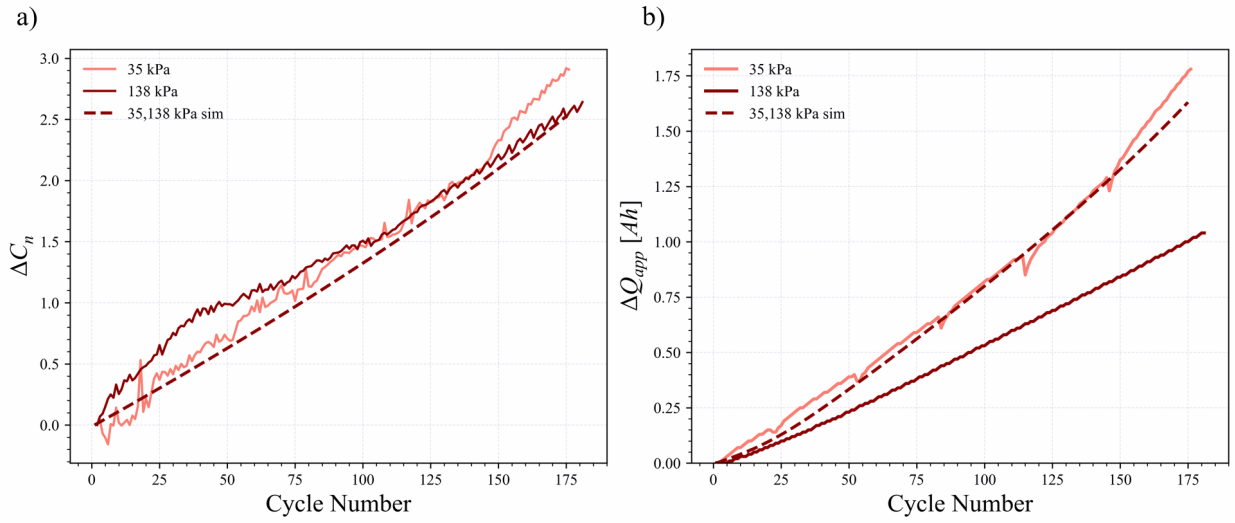


Figure C.3: a) Negative electrode capacity loss simulation at 35 and 138 kPa b) Apparent capacity loss simulation using outlier value of $\beta^-_{\mathrm{LAM},s}(P)$ at 138 kPa

Using the values of $\beta^-_{\mathrm{LAM},s}(P)$ in Fig. C.2 and simulating the battery aging at 35 and 138

kPa, we get the ΔC_n curves as shown in Fig. C.3 a) and apparent capacity loss ΔQ_{app} curves in Fig. C.3 b). Even though we match the ΔC_n at 138 kPa, we don't match ΔQ_{app}.

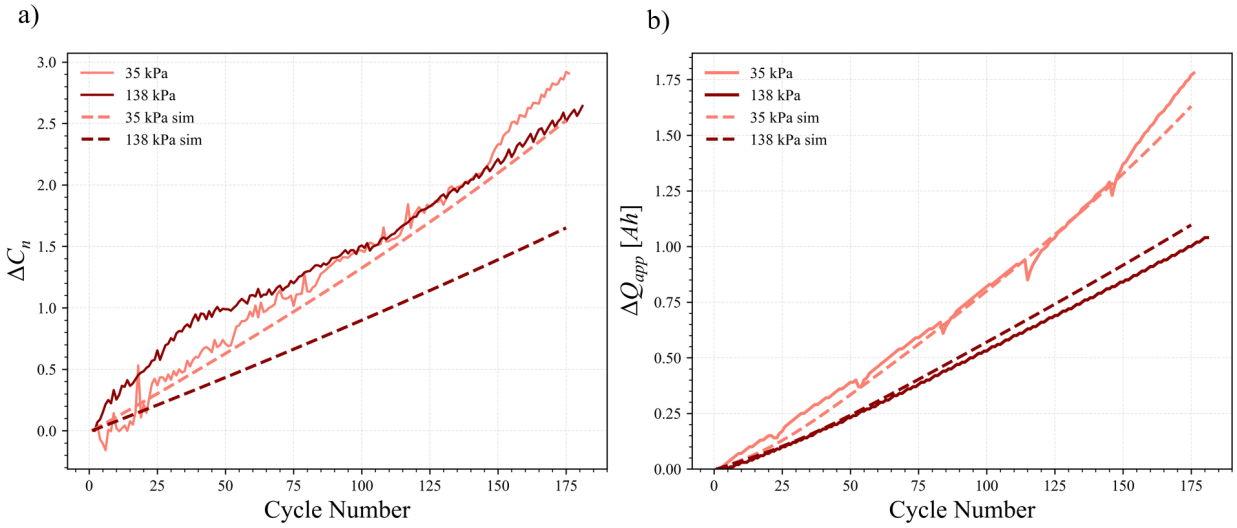


Figure C.4: a) Negative electrode capacity loss simulation at 35 and 138 kPa b) Apparent capacity loss simulation without using outlier value of $\beta^{-}_{\text{LAM},s}(P)$ at 138 kPa

Therefore, we use the values of $\beta^{-}_{\text{LAM},s}(P)$ in Fig. 6.9, which has the same value of $\beta^{-}_{\text{LAM},s}(P)$ for 69-172 kPa, instead of an outlier value at 138 in Fig. C.2, in our degradation model in Chapter 6. Using the values of $\beta^{-}_{\text{LAM},s}(P)$ in Fig. 6.9 and simulating the battery aging at 35 and 138 kPa, we get the ΔC_n curves as shown in Fig. C.4 a) and apparent capacity loss ΔQ_{app} curves in Fig. C.4 b). Now, we don't match the ΔC_n at 138 kPa, but we match the value of ΔQ_{app} which is more important for predicting the battery degradation.

BIBLIOGRAPHY

[1] Peyman Mohtat, Suhak Lee, Jason B. Siegel, and Anna G. Stefanopoulou. Reversible and Irreversible Expansion of Lithium-Ion Batteries Under a Wide Range of Stress Factors. *Journal of The Electrochemical Society*, 168(10):100520, October 2021.

[2] A.J. Louli, L.D. Ellis, and J.R. Dahn. Operando Pressure Measurements Reveal Solid Electrolyte Interphase Growth to Rank Li-Ion Cell Performance. *Joule*, 3(3):745–761, March 2019.

[3] Valentin Sulzer, Peyman Mohtat, Sravan Pannala, Jason B. Siegel, and Anna G. Stefanopoulou. Accelerated Battery Lifetime Simulations Using Adaptive Inter-Cycle Extrapolation Algorithm. *Journal of The Electrochemical Society*, 168(12):120531, December 2021.

[4] Valentin Sulzer, Peyman Mohtat, Antti Aitio, Suhak Lee, Yen T. Yeh, Frank Steinbacher, Muhammad Umer Khan, Jang Woo Lee, Jason B. Siegel, Anna G. Stefanopoulou, and David A. Howey. The challenge and opportunity of battery lifetime prediction from field data. *Joule*, 5(8):1934–1955, August 2021.

[5] Weihan Li, Neil Sengupta, Philipp Dechent, David Howey, Anuradha Annaswamy, and Dirk Uwe Sauer. One-shot battery degradation trajectory prediction with deep learning. *Journal of Power Sources*, 506:230024, September 2021.

[6] I Bloom, B.W Cole, J.J Sohn, S.A Jones, E.G Polzin, V.S Battaglia, G.L Henriksen, C Motloch, R Richardson, T Unkelhaeuser, D Ingersoll, and H.L Case. An accelerated calendar and cycle life study of Li-ion cells. *Journal of Power Sources*, 101(2):238–247, October 2001.

[7] Johannes Schmalstieg, Stefan Käbitz, Madeleine Ecker, and Dirk Uwe Sauer. A holistic aging model for Li(NiMnCo)O2 based 18650 lithium-ion batteries. *Journal of Power Sources*, 257:325–334, July 2014.

[8] Marcus Johnen, Simon Pitzen, Udo Kamps, Maria Kateri, Philipp Dechent, and Dirk Uwe Sauer. Modeling long-term capacity degradation of lithium-ion batteries. *Journal of Energy Storage*, 34:102011, 2021.

[9] Paul Gasper, Kevin Gering, Eric Dufek, and Kandler Smith. Challenging Practices of Algebraic Battery Life Models through Statistical Validation and Model Identification via Machine-Learning. *Journal of The Electrochemical Society*, 168(2):020502, February 2021.

[10] P Ramadass, Bala Haran, Ralph White, and Branko N Popov. Mathematical modeling of the capacity fade of li-ion cells. *Journal of power sources*, 123(2):230–240, 2003.

[11] Christoph R. Birkl, Matthew R. Roberts, Euan McTurk, Peter G. Bruce, and David A. Howey. Degradation diagnostics for lithium ion cells. *Journal of Power Sources*, 341:373–386, February 2017.

[12] Jorn M. Reniers, Grietus Mulder, and David A. Howey. Review and Performance Comparison of Mechanical-Chemical Degradation Models for Lithium-Ion Batteries. *Journal of The Electrochemical Society*, 166(14):A3189–A3200, 2019.

[13] P. Ramadass, Bala Haran, Parthasarathy M. Gomadam, Ralph White, and Branko N. Popov. Development of First Principles Capacity Fade Model for Li-Ion Cells. *Journal of The Electrochemical Society*, 151(2):A196, 2004.

[14] C. Delacourt and M. Safari. Life Simulation of a Graphite/LiFePO $_4$ Cell under Cycling and Storage. *Journal of The Electrochemical Society*, 159(8):A1283–A1291, 2012.

[15] Dongjiang Li, Dmitry Danilov, Zhongru Zhang, Huixin Chen, Yong Yang, and Peter H. L. Notten. Modeling the SEI-Formation on Graphite Electrodes in LiFePO $_4$ Batteries. *Journal of The Electrochemical Society*, 162(6):A858–A869, 2015.

[16] Xiao-Guang Yang, Yongjun Leng, Guangsheng Zhang, Shanhai Ge, and Chao-Yang Wang. Modeling of lithium plating induced aging of lithium-ion batteries: Transition from linear to nonlinear aging. *Journal of Power Sources*, 360:28–40, August 2017.

[17] Xiao-Guang Yang, Shanhai Ge, Teng Liu, Yongjun Leng, and Chao-Yang Wang. A look into the voltage plateau signal for detection and quantification of lithium plating in lithium-ion cells. *Journal of Power Sources*, 395:251–261, August 2018.

[18] Izaro Laresgoiti, Stefan Käbitz, Madeleine Ecker, and Dirk Uwe Sauer. Modeling mechanical degradation in lithium ion batteries during cycling: Solid electrolyte interphase fracture. *Journal of Power Sources*, 300:112–122, December 2015.

[19] Rutooj Deshpande, Mark Verbrugge, Yang-Tse Cheng, John Wang, and Ping Liu. Battery Cycle Life Prediction with Coupled Chemical Degradation and Fatigue Mechanics. *Journal of The Electrochemical Society*, 159(10):A1730–A1738, 2012.

[20] Matthew B. Pinson and Martin Z. Bazant. Theory of SEI Formation in Rechargeable Batteries: Capacity Fade, Accelerated Aging and Lifetime Prediction. *Journal of The Electrochemical Society*, 160(2):A243–A250, 2013.

[21] Tobias Deich, Mathias Storch, Kai Steiner, and Andreas Bund. Effects of module stiffness and initial compression on lithium-ion cell aging. *Journal of Power Sources*, 506:230163, September 2021.

[22] Hao Ge, Tetsuya Aoki, Nobuhisa Ikeda, Sohei Suga, Takuma Isobe, Zhe Li, Yuichiro Tabuchi, and Jianbo Zhang. Investigating Lithium Plating in Lithium-Ion Batteries at Low Temperatures Using Electrochemical Model with NMR Assisted Parameterization. *Journal of The Electrochemical Society*, 164(6):A1050–A1060, 2017.

[23] Scott J. Moura, Federico Bribiesca Argomedo, Reinhardt Klein, Anahita Mirtabatabaei, and Miroslav Krstic. Battery State Estimation for a Single Particle Model With Electrolyte Dynamics. *IEEE Transactions on Control Systems Technology*, 25(2):453–468, March 2017.

[24] Marc Doyle, Thomas F Fuller, and John Newman. Modeling of galvanostatic charge and discharge of the lithium/polymer/insertion cell. *Journal of the Electrochemical society*, 140(6):1526, 1993.

[25] Tianhan Gao, Andrew Kim, and Wei Lu. Modeling electrode-level crack and quantifying its effect on battery performance and impedance. *Electrochimica Acta*, 363:137197, 2020.

[26] Bin Wu and Wei Lu. A consistently coupled multiscale mechanical–electrochemical battery model with particle interaction and its validation. *Journal of the Mechanics and Physics of Solids*, 125:89–111, 2019.

[27] Pallab Barai and Partha P. Mukherjee. Stochastic Analysis of Diffusion Induced Damage in Lithium-Ion Battery Electrodes. *Journal of The Electrochemical Society*, 160(6):A955–A967, 2013.

[28] Alexander Bills, Shashank Sripad, William L. Fredericks, Matthew Guttenberg, Devin Charles, Evan Frank, and Venkatasubramanian Viswanathan. Universal Battery Performance and Degradation Model for Electric Aircraft. *arXiv:2008.01527 [physics]*, March 2021.

[29] Mingyu Gao, Yuanyuan Liu, and Zhiwei He. Battery state of charge online estimation based on particle filter. In *2011 4th International Congress on Image and Signal Processing*, pages 2233–2236, Shanghai, October 2011. IEEE.

[30] Yizhao Gao, Xi Zhang, Chong Zhu, and Bangjun Guo. Global Parameter Sensitivity Analysis of Electrochemical Model for Lithium-Ion Batteries Considering Aging. *IEEE/ASME Transactions on Mechatronics*, 26(3):1283–1294, June 2021.

[31] Coralia Cartis, Jan Fiala, Benjamin Marteau, and Lindon Roberts. Improving the Flexibility and Robustness of Model-based Derivative-free Optimization Solvers. *ACM Transactions on Mathematical Software*, 45(3):1–41, September 2019.

[32] Shankar Mohan, Youngki Kim, Jason B. Siegel, Nassim A. Samad, and Anna G. Stefanopoulou. A Phenomenological Model of Bulk Force in a Li-Ion Battery Pack and Its Application to State of Charge Estimation. *Journal of The Electrochemical Society*, 161(14):A2222–A2231, 2014.

[33] Peyman Mohtat, Suhak Lee, Valentin Sulzer, Jason B. Siegel, and Anna G. Stefanopoulou. Differential Expansion and Voltage Model for Li-ion Batteries at Practical Charging Rates. *Journal of The Electrochemical Society*, 167(11):110561, January 2020.

[34] Miriam A. Figueroa-Santos, Jason B. Siegel, and Anna G. Stefanopoulou. Leveraging Cell Expansion Sensing in State of Charge Estimation: Practical Considerations. *Energies*, 13(10):2653, May 2020.

[35] Nassim A. Samad, Youngki Kim, Jason B. Siegel, and Anna G. Stefanopoulou. Battery Capacity Fading Estimation Using a Force-Based Incremental Capacity Analysis. *Journal of The Electrochemical Society*, 163(8):A1584–A1594, 2016.

[36] Aaron Knobloch, Chris Kapusta, Jason Karp, Yuri Plotnikov, Jason B. Siegel, and Anna G. Stefanopoulou. Fabrication of Multimeasurand Sensor for Monitoring of a Li-Ion Battery. *Journal of Electronic Packaging*, 140(3), 05 2018. 031002.

[37] John Cannarella and Craig B. Arnold. State of health and charge measurements in lithium-ion batteries using mechanical stress. *Journal of Power Sources*, 269:7–14, December 2014.

[38] E. M. C. Jones, Ö. Ö. Çapraz, S. R. White, and N. R. Sottos. Reversible and Irreversible Deformation Mechanisms of Composite Graphite Electrodes in Lithium-Ion Batteries. *Journal of The Electrochemical Society*, 163(9):A1965–A1974, 2016.

[39] Lisa K. Willenberg, Philipp Dechent, Georg Fuchs, Dirk Uwe Sauer, and Egbert Figgemeier. High-Precision Monitoring of Volume Change of Commercial Lithium-Ion Batteries by Using Strain Gauges. *Sustainability*, 12(2):557, January 2020.

[40] Otto von Kessel, Tobias Deich, Severin Hahn, Felix Brauchle, Dragoljub Vrankovic, Thomas Soczka-Guth, and Kai Peter Birke. Mechanical impedance as a tool for electromechanical investigation and equivalent modeling of lithium-ion batteries. *Journal of Power Sources*, 508:230337, October 2021.

[41] Severin Hahn, Sebastian Theil, Jan Kroggel, and Kai Peter Birke. Pressure Prediction Modeling and Validation for Lithium-Ion Pouch Cells in Buffered Module Assemblies. *Journal of Energy Storage*, 40:102517, August 2021.

[42] Peyman Mohtat, Suhak Lee, Jason B. Siegel, and Anna G. Stefanopoulou. Comparison of expansion and voltage differential indicators for battery capacity fade. *Journal of Power Sources*, 518:230714, January 2022.

[43] Taylor R. Garrick, Kenneth Higa, Shao-Ling Wu, Yiling Dai, Xinyu Huang, Venkat Srinivasan, and John W. Weidner. Modeling Battery Performance Due to Intercalation Driven Volume Change in Porous Electrodes. *Journal of The Electrochemical Society*, 164(11):E3592–E3597, 2017.

[44] Drew J. Pereira, Miguel A. Fernandez, Kathryn C. Streng, Xu Xian Hou, Xiujie Gao, John W. Weidner, and Taylor R. Garrick. Accounting for Non-Ideal, Lithiation-Based Active Material Volume Change in Mechano-Electrochemical Pouch Cell Simulation. *Journal of The Electrochemical Society*, 167(8):080515, January 2020.

[45] Chao Zhang, Jun Xu, Lei Cao, Zenan Wu, and Shriram Santhanagopalan. Constitutive behavior and progressive mechanical failure of electrodes in lithium-ion batteries. *Journal of Power Sources*, 357:126–137, July 2017.

[46] Anup Barai, Ravichandra Tangirala, Kotub Uddin, Julie Chevalier, Yue Guo, Andrew McGordon, and Paul Jennings. The effect of external compressive loads on the cycle lifetime of lithium-ion pouch cells. *Journal of Energy Storage*, 13:211–219, 2017.

[47] Abdilbari Shifa Mussa, Matilda Klett, Göran Lindbergh, and Rakel Wreland Lindström. Effects of external pressure on the performance and ageing of single-layer lithium-ion pouch cells. *Journal of Power Sources*, 385:18–26, 2018.

[48] Verena Müller, Rares-George Scurtu, Michaela Memm, Michael A Danzer, and Margret Wohlfahrt-Mehrens. Study of the influence of mechanical pressure on the performance and aging of lithium-ion battery cells. *Journal of Power Sources*, 440:227148, 2019.

[49] Hanqing Yu, Li Wang, Zhiguo Zhang, Yiding Li, Shichun Yang, and Xiangming He. Insight understanding of external pressure on lithium plating in commercial lithium-ion batteries. *Advanced Functional Materials*, page 2406966, 2024.

[50] Arber Avdyli, Alexander Fill, and Kai Peter Birke. Modeling and experimental investigation of the interaction between pressure-dependent aging and pressure development due to the aging of lithium-ion cells. *Batteries*, 9(10), 2023.

[51] Kandler Smith, Paul Gasper, Andrew M. Colclasure, Yuta Shimonishi, and Shuhei Yoshida. Lithium-Ion Battery Life Model with Electrode Cracking and Early-Life Break-in Processes. *Journal of The Electrochemical Society*, 168(10):100530, October 2021.

[52] Aaron Knobloch, Chris Kapusta, Jason Karp, Yuri Plotnikov, Jason B. Siegel, and Anna G. Stefanopoulou. Fabrication of Multimeasurand Sensor for Monitoring of a Li-Ion Battery. *Journal of Electronic Packaging*, 140(3):031002, September 2018.

[53] Domenico Di Domenico, Anna Stefanopoulou, and Giovanni Fiengo. Lithium-Ion Battery State of Charge and Critical Surface Charge Estimation Using an Electrochemical Model-Based Extended Kalman Filter. *Journal of Dynamic Systems, Measurement, and Control*, 132(6):061302, November 2010.

[54] Joel C Forman, Saeid Bashash, Jeffrey L Stein, and Hosam K Fathy. Reduction of an electrochemistry-based li-ion battery model via quasi-linearization and pade approximation. *Journal of the Electrochemical Society*, 158(2):A93, 2010.

[55] Peyman Mohtat, Suhak Lee, Jason B. Siegel, and Anna G. Stefanopoulou. Towards better estimability of electrode-specific state of health: Decoding the cell expansion. *Journal of Power Sources*, 427:101–111, July 2019.

[56] Xiangchun Zhang, Wei Shyy, and Ann Marie Sastry. Numerical Simulation of Intercalation-Induced Stress in Li-Ion Battery Electrode Particles. *Journal of The Electrochemical Society*, 154(10):A910, 2007.

[57] Taylor R Garrick, Kumud Kanneganti, Xinyu Huang, and John W Weidner. Modeling volume change due to intercalation into porous electrodes. *Journal of The Electrochemical Society*, 161(8):E3297, 2014.

[58] Taylor R. Garrick, Miguel A. Fernandez, Mark W. Verbrugge, Christine Labaza, Rafid Mollah, Brian J. Koch, Matthew D. Jones, Jing Gao, Xiujie Gao, and Nicholas Irish. Quantifying volume change in porous electrodes via the multi-species, multi-reaction model. *Journal of The Electrochemical Society*, 170(6):060548, jun 2023.

[59] G.L. Plett. *Battery Management Systems, Volume I: Battery Modeling*. Artech House power engineering series. Artech House, 2015.

[60] Bernhard Rieger, Steffen Schlueter, Simon V Erhard, and Andreas Jossen. Strain propagation in lithium-ion batteries from the crystal structure to the electrode level. *Journal of The Electrochemical Society*, 163(8):A1595, 2016.

[61] Valentin Sulzer, Scott G. Marquis, Robert Timms, Martin Robinson, and S. Jon Chapman. Python Battery Mathematical Modelling (PyBaMM). *Journal of Open Research Software*, 9:14, June 2021.

[62] Simon EJ O'Kane, Ian D Campbell, Mohamed WJ Marzook, Gregory J Offer, and Monica Marinescu. Physical origin of the differential voltage minimum associated with lithium plating in li-ion batteries. *Journal of The Electrochemical Society*, 167(9):090540, 2020.

[63] Pallab Barai, Kandler Smith, Chien-Fan Chen, Gi-Heon Kim, and Partha P. Mukherjee. Reduced Order Modeling of Mechanical Degradation Induced Performance Decay in Lithium-Ion Battery Porous Electrodes. *Journal of The Electrochemical Society*, 162(9):A1751–A1771, 2015.

[64] Simon EJ O'Kane, Weilong Ai, Ganesh Madabattula, Diego Alonso-Alvarez, Robert Timms, Valentin Sulzer, Jacqueline Sophie Edge, Billy Wu, Gregory J Offer, and Monica Marinescu. Lithium-ion battery degradation: how to model it. *Physical Chemistry Chemical Physics*, 24(13):7909–7922, 2022.

[65] Sravan Pannala, Valentin Sulzer, Jason B Siegel, and Anna G Stefanopoulou. Methodology for accelerated inter-cycle simulations of li-ion battery degradation with intra-cycle resolved degradation mechanisms. In *2022 American Control Conference (ACC)*, pages 1788–1793. IEEE, 2022.

[66] Nicholas M Meyer. *Effects of mean stress and stress concentration on fatigue behavior of ductile iron*. The University of Toledo, 2014.

[67] Robert Burger and Yung-Li Lee. Assessment of the mean-stress sensitivity factor method in stress-life fatigue predictions. *Journal of Testing and Evaluation*, 41(2):200–206, 2013.

[68] Hyung-Joo Noh, Sungjune Youn, Chong Seung Yoon, and Yang-Kook Sun. Comparison of the structural and electrochemical properties of layered li [nixcoymnz] o2 (x= 1/3, 0.5, 0.6, 0.7, 0.8 and 0.85) cathode material for lithium-ion batteries. *Journal of power sources*, 233:121–130, 2013.

[69] Frank M. Kindermann, Jonas Keil, Alexander Frank, and Andreas Jossen. A sei modeling approach distinguishing between capacity and power fade. *Journal of The Electrochemical Society*, 164:E287–E294, 2017.

[70] Roby Gauthier, Aidan Luscombe, Toby Bond, Michael Bauer, Michel Johnson, Jessie Harlow, Alex Louli, and Jeff R Dahn. How do Depth of Discharge, C-rate and Calendar Age Affect Capacity Retention, Impedance Growth, the Electrodes, and the Electrolyte in Li-Ion Cells? *Journal of The Electrochemical Society*, January 2022.

[71] Christian Kupper, Björn Weißhar, Sascha Rißmann, and Wolfgang G. Bessler. End-of-Life Prediction of a Lithium-Ion Battery Cell Based on Mechanistic Aging Models of the Graphite Electrode. *Journal of The Electrochemical Society*, 165(14):A3468–A3480, 2018.

[72] Ashish P Vora, Xing Jin, Vaidehi Hoshing, Gregory Shaver, Subbarao Varigonda, and Wallace E Tyner. Integrating battery degradation in a cost of ownership framework for hybrid electric vehicle design optimization. *Proceedings of the Institution of Mechanical Engineers, Part D: Journal of Automobile Engineering*, 233(6):1507–1523, May 2019.

[73] Hyobin Lee, Seungwon Yang, Suhwan Kim, Jihun Song, Joonam Park, Chil Hoon Doh, Yoon Cheol Ha, Tae Soon Kwon, and Yong Min Lee. Understanding the effects of diffusion coefficient and exchange current density on the electrochemical model of lithium-ion batteries. *Current Opinion in Electrochemistry*, 34:100986, 2022.

[74] Andrew Weng, Everardo Olide, Iaroslav Kovalchuk, Jason Siegel, and Anna Stefanopoulou. Modeling battery formation: Boosted sei growth, multi-species reactions, and irreversible expansion. *Journal of The Electrochemical Society*, 2023.

[75] Yoon Koo Lee, Jonghyun Park, and Wei Lu. A comprehensive experimental and modeling study on dissolution in li-ion batteries. *Journal of The Electrochemical Society*, 166(8):A1340, 2019.

[76] Hamidreza Movahedi, Sravan Pannala, Jason Siegel, Stephen J Harris, David Howey, and Anna Stefanopoulou. Extra throughput versus days lost in v2g services: Influence of dominant degradation mechanism. *Journal of Energy Storage*, 104:114242, 2024.

[77] Paul Albertus, Venkataramani Anandan, Chunmei Ban, Nitash Balsara, Ilias Belharouak, Josh Buettner-Garrett, Zonghai Chen, Claus Daniel, Marca Doeff, Nancy J Dudney, et al. Challenges for and pathways toward li-metal-based all-solid-state batteries, 2021.

[78] Vivian Tran, Jason Siegel, and Anna Stefanopoulou. Extending a multi-physics li-ion battery model from normal operation to short circuit and venting. *Journal of The Electrochemical Society*, 2024.

[79] Dale Hall and Nic Lutsey. Emerging best practices for electric vehicle charging infrastructure. *White Paper. The International Council on Clean Transportation (ICCT)*, page 54, 2017.

[80] Chien-fei Chen, Gerardo Zarazua de Rubens, Lance Noel, Johannes Kester, and Benjamin K. Sovacool. Assessing the socio-demographic, technical, economic and behavioral factors of Nordic electric vehicle adoption and the influence of vehicle-to-grid preferences. *Renewable and Sustainable Energy Reviews*, 121:109692, April 2020.

[81] Gordon Bauer, Chih-Wei Hsu, Mike Nicholas, and Nic Lutsey. Charging up America: Assessing the growing need for U.S. charging infrastructure through 2030. *White Paper. International Council on Clean Transportation (ICCT)*, page 45, July 2021.

[82] Saehong Park, Donggun Lee, Hyoung Jun Ahn, Claire Tomlin, and Scott Moura. Optimal Control of Battery Fast Charging Based-on Pontryagin's Minimum Principle. In *2020 59th IEEE Conference on Decision and Control (CDC)*, pages 3506–3513, Jeju, Korea (South), December 2020. IEEE.

[83] Kandler A. Smith, Christopher D. Rahn, and Chao-Yang Wang. Model-Based Electrochemical Estimation and Constraint Management for Pulse Operation of Lithium Ion Batteries. *IEEE Transactions on Control Systems Technology*, 18(3):654–663, May 2010.

[84] D. Anseán, M. González, J.C. Viera, V.M. García, C. Blanco, and M. Valledor. Fast charging technique for high power lithium iron phosphate batteries: A cycle life analysis. *Journal of Power Sources*, 239:9–15, October 2013.

[85] Lalit Patnaik, A. V. J. S. Praneeth, and Sheldon S. Williamson. A Closed-Loop Constant-Temperature Constant-Voltage Charging Technique to Reduce Charge Time of Lithium-Ion Batteries. *IEEE Transactions on Industrial Electronics*, 66(2):1059–1067, February 2019.

[86] Manan Pathak, Suryanarayana Kolluri, and Venkat R. Subramanian. Generic Model Control for Lithium-Ion Batteries. *Journal of The Electrochemical Society*, 164(6):A973–A986, 2017.

[87] Reinhardt Klein, Nalin A. Chaturvedi, Jake Christensen, Jasim Ahmed, Rolf Findeisen, and Aleksandar Kojic. Optimal charging strategies in lithium-ion battery. In *Proceedings of the 2011 American Control Conference*, pages 382–387, San Francisco, CA, June 2011. IEEE.

[88] Shankar Mohan, Youngki Kim, and Anna G. Stefanopoulou. Energy-Conscious Warm-Up of Li-Ion Cells From Subzero Temperatures. *IEEE Transactions on Industrial Electronics*, 63(5):2954–2964, May 2016.

[89] Youngki Kim, Shankar Mohan, Nassim A. Samad, Jason B. Siegel, and Anna G. Stefanopoulou. Optimal power management for a series hybrid electric vehicle cognizant of battery mechanical effects. In *2014 American Control Conference*, pages 3832–3837, Portland, OR, USA, June 2014. IEEE.

[90] Bharatkumar Suthar, Venkatasailanathan Ramadesigan, Sumitava De, Richard D. Braatz, and Venkat R. Subramanian. Optimal charging profiles for mechanically constrained lithium-ion batteries. *Phys. Chem. Chem. Phys.*, 16(1):277–287, 2014.

[91] H. E. Perez, S. Dey, X. Hu, and S. J. Moura. Optimal Charging of Li-Ion Batteries via a Single Particle Model with Electrolyte and Thermal Dynamics. *Journal of The Electrochemical Society*, 164(7):A1679–A1687, 2017.

[92] Alexander Bartlett, James Marcicki, Kevin Rhodes, and Giorgio Rizzoni. State of health estimation in composite electrode lithium-ion cells. *Journal of Power Sources*, 284:642–649, 2015.

[93] Chen Zhu, Liqing Sun, Cheng Chen, Jinpeng Tian, Weixiang Shen, and Rui Xiong. Lithium-ion battery degradation diagnosis and state-of-health estimation with half cell electrode potential. *Electrochimica Acta*, 459:142588, 2023.

[94] Satadru Dey, Ying Shi, Kandler Smith, Andrew M Colclasure, and Xuemin Li. From battery cell to electrodes: Real-time estimation of charge and health of individual battery electrodes. *IEEE Transactions on Industrial Electronics*, 67(3):2167–2175, 2019.

[95] Matteo Acquarone, Federico Miretti, Daniela Misul, and Simona Onori. Sleek dual extended kalman filter for battery state of charge and state of health estimation in electric vehicle applications. Technical report, SAE Technical Paper, 2024.

[96] Robert R Richardson, Michael A Osborne, and David A Howey. Battery health prediction under generalized conditions using a gaussian process transition model. *Journal of Energy Storage*, 23:320–328, 2019.

[97] Haijun Ruan, Niall Kirkaldy, Gregory J Offer, and Billy Wu. Diagnosing health in composite battery electrodes with explainable deep learning and partial charging data. *Energy and AI*, 16:100352, 2024.

[98] Suhak Lee, Jason B. Siegel, Anna G. Stefanopoulou, Jang-Woo Lee, and Tae-Kyung Lee. Electrode State of Health Estimation for Lithium Ion Batteries Considering Half-cell Potential Change Due to Aging. *Journal of The Electrochemical Society*, 167(9):090531, 2020.

[99] Shida Jiang, Junzhe Shi, Manashita Borah, and Scott Moura. Weaknesses and improvements of the extended kalman filter for battery state-of-charge and state-of-health estimation. In *2024 American Control Conference (ACC)*, pages 1441–1448. IEEE, 2024.

[100] Iker Lopetegi, Gregory L Plett, M Scott Trimboli, Laura Oca, Eduardo Miguel, and Unai Iraola. A new battery soc/soh/esoh estimation method using a pbm and interconnected spkfs: Part ii. soh and esoh estimation. *Journal of The Electrochemical Society*, 171(3):030518, 2024.

[101] Suhak Lee, Peyman Mohtat, Jason B. Siegel, Anna G. Stefanopoulou, Jang-Woo Lee, and Tae-Kyung Lee. Estimation error bound of battery electrode parameters with limited data window. *IEEE Transactions on Industrial Informatics*, 16(5):3376–3386, 2020.

[102] Apoorva Roy, Hamidreza Movahedi, Jason B. Siegel, and Anna G. Stefanopoulou. Empirical modeling of degradation in lithium-ion batteries and validation in complex scenarios. *IFAC-PapersOnLine*, 56(3):457–462, 2023. 3rd Modeling, Estimation and Control Conference MECC 2023.

[103] Peyman Mohtat, Jason Siegel, Anna Stefanopoulou, and Suhak Lee. Uofm pouch cell voltage and expansion cyclic aging dataset [data set]. *University of Michigan - Deep Blue Data*, 2021.

[104] Suhak Lee, Jason B. Siegel, Anna G. Stefanopoulou, Jang-Woo Lee, and Tae-Kyung Lee. Comparison of Individual-Electrode State of Health Estimation Methods for Lithium Ion Battery. In *Volume 2: Control and Optimization of Connected and Automated Ground Vehicles; Dynamic Systems and Control Education; Dynamics and Control of Renewable Energy Systems; Energy Harvesting; Energy Systems; Estimation and Identification; Intelligent Transportation and Vehicles; Manufacturing; Mechatronics; Modeling and Control of IC Engines and Aftertreatment Systems; Modeling and Control of IC Engines and Powertrain Systems; Modeling and Management of Power Systems*, page V002T19A002, Atlanta, Georgia, USA, September 2018. American Society of Mechanical Engineers.

[105] Kirk D Stetzel, Lukas L Aldrich, M Scott Trimboli, and Gregory L Plett. Electrochemical state and internal variables estimation using a reduced-order physics-based model of a lithium-ion cell and an extended kalman filter. *J. Power Sources*, 278:490–505, 2015.

[106] Shu-Xia Tang, Leobardo Camacho-Solorio, Yebin Wang, and Miroslav Krstic. State-of-charge estimation from a thermal–electrochemical model of lithium-ion batteries. *Automatica*, 83:206–219, 2017.

[107] Scott J Moura, Federico Bribiesca Argomedo, Reinhardt Klein, Anahita Mirtabatabaei, and Miroslav Krstic. Battery state estimation for a single particle model with electrolyte dynamics. *IEEE Trans Control Syst Technol*, 25(2):453–468, 2017.

[108] Kandler A Smith, Christopher D Rahn, and Chao-Yang Wang. Model-based electrochemical estimation and constraint management for pulse operation of lithium ion batteries. *IEEE Trans Control Syst Technol*, 18(3):654–663, 2009.

[109] Domenico Di Domenico, Anna Stefanopoulou, and Giovanni Fiengo. Lithium-ion battery state of charge and critical surface charge estimation using an electrochemical model-based extended kalman filter. *Journal of dynamic systems, measurement, and control*, 132(6), 2010.

[110] Ashlee N Ford Versypt and Richard D Braatz. Analysis of finite difference discretization schemes for diffusion in spheres with variable diffusivity. *Computers & chemical engineering*, 71:241–252, 2014.

[111] Peyman Mohtat, Farinaz Nezampasandarbabi, Shankar Mohan, Jason B. Siegel, and Anna G. Stefanopoulou. On identifying the aging mechanisms in li-ion batteries using two points measurements. In *2017 American Control Conference (ACC)*, pages 98–103, Seattle, WA, USA, May 2017. IEEE.